ATOMISTIC STUDIES OF DEFECTS IN BCC IRON: DISLOCATIONS AND GAS BUBBLES

A Dissertation
Presented to
The Academic Faculty

by

Erin G. Hayward

In Partial Fulfillment
of the Requirements for the Degree
Doctor of Philosophy in the
George W. Woodruff School of Mechanical Engineering
Nuclear and Radiological Engineering Program

Georgia Institute of Technology
August 2012

ATOMISTIC STUDIES OF DEFECTS IN BCC IRON: DISLOCATIONS AND GAS BUBBLES

Approved by:

Chaitanya S. Deo, Advisor
George W. Woodruff School of
Mechanical Engineering
Nuclear and Radiological Engineering
Program
Georgia Institute of Technology

Dr. Weston M. Stacey
George W. Woodruff School of
Mechanical Engineering
Nuclear and Radiological Engineering
Program
Georgia Institute of Technology

Dr. Ting Zhu
George W. Woodruff School of
Mechanical Engineering
Georgia Institute of Technology

Dr. Mo Li
School of Materials Science and
Engineering
Georgia Institute of Technology

Dr. Preet Singh
School of Materials Science and
Engineering
Georgia Institute of Technology

Dr. Blas P. Uberuaga
Materials Science and Technology
Division
Los Alamos National Laboratory

Date Approved: 25 April 2012

To my loves, Rob and Proton

ACKNOWLEDGEMENTS

TABLE OF CONTENTS

LIST OF TABLES

LIST OF FIGURES

SUMMARY

The structure and interactions of the defects in material on an atomistic scale ultimately determine the macroscopic behavior of that material. A fundamental understanding of how defects behave is essential for predicting materials failure; this is especially true in an irradiated environment, where defects are created at higher than average rates. In this work, we present two different atomistic scale computational studies of defects in body centered cubic (bcc) iron. First, the interaction energies between screw dislocations (line defects) and various kinds of point defects will be calculated, using anisotropic linear elastic theory and atomistic simulation, and compared. Second, the energetics and behavior of hydrogen and hydrogen-helium gas bubbles will be investigated.

CHAPTER I

INTRODUCTION

The interactions between defects within a material's microstructure determine the ultimate behavior of the material on a macroscopic scale. Dramatic macroscopic behavioral changes include creep, plasticity, radiation-induced segregation, embrittlement, changes in brittle to ductile transition temperature, hardening, and cracking. Atomistic studies provide a valuable tool for investigating these interactions in a detailed and fundamental way.

Ferritic steels are a popular choice for current and future reactor designs. These steels are mainly composed of body centered cubic, or α-phase iron. Thus, this material is a relevant and important choice for the matrix in which we perform defect studies.

The goal of this work is to examine the interactions and energetics of defects on the microscale, in order to gain a more fundamental understanding of their behavior. We use atomistics as a tool for this purpose.

1.1 Radiation Damage

A material undergoing irradiation experiences a high rate of defect creation due to a high volume of incident particles, so the study of defect behavior is particularly important to the study of irradiated materials. The process of radiation damage proceeds in several stages, as is shown in Figure 1. First, and incident particle transfers some or all of its energy to an atom in the crystal, resulting in the atom being removed from its lattice site. This atom, known as the primary knock-on atom, or PKA, goes on to interact with other atoms in the system, creating a cascade of damage. Ultimately, some of the affected atoms will come to rest in off lattice sites as interstitials, leaving behind an empty lattice site known as a vacancy. A vacancy and an interstitial are together known as as Frenkel pair. The majority of Frenkel pairs created during a damage cascade will recombine within several picoseconds. However, a small number of the created defects some will remain, usually creating a structure consisting of a core of vacancies surrounded by a shell of interstitials. Over time, these

(a) 0.1 ps

(b) 0.9 ps - near peak damage

(c) 4.0 ps - partially relaxed

(d) 20.0 ps - fully relaxed
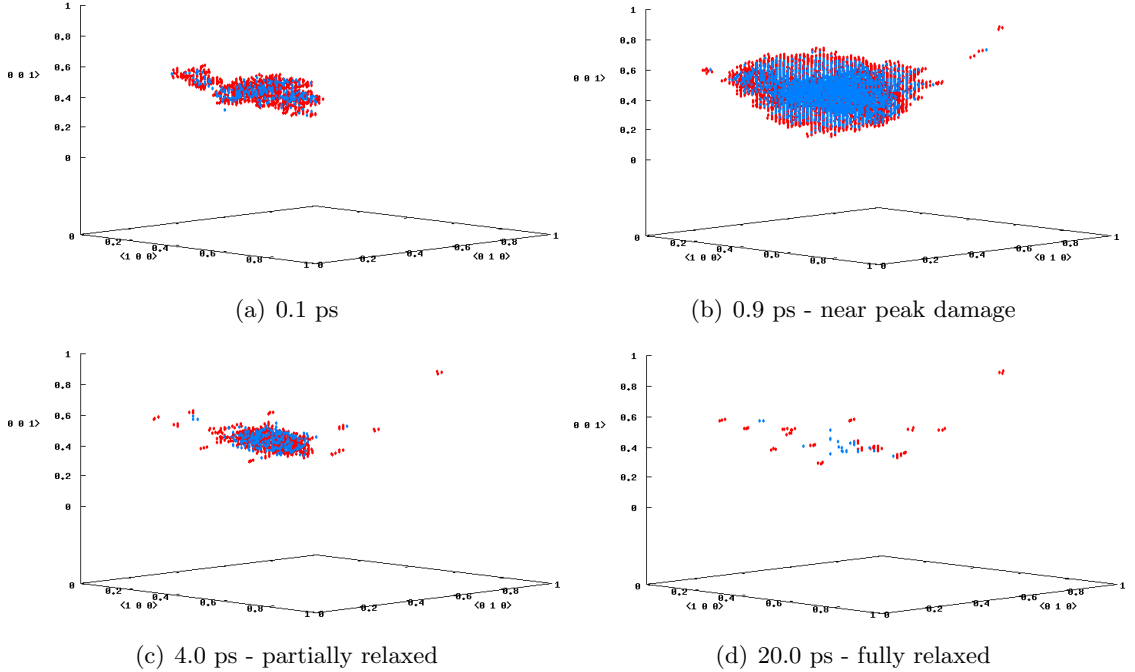
Figure 1: Four snapshots from a 10 keV cascade in pure Fe. Red dots show interstitials, blue dots show vacancies. Note the vacancy rich core surrounded by interstitials.

point defects migrate through the lattice, cluster together, and form extended defects, such as dislocation lines and loops.

1.1.1 The Crystal Lattice

The Miller indices [86] are the most commonly used notation system for describing planes and directions in crystal lattices. A unit cell coordinate system is defined by three lattice vectors (for a cubic lattice, these will be orthogonal). The inverse intercepts along these lattice vectors expressed in integer form define a plane (hkl), a family of planes $\{hkl\}$, a direction $[hkl]$, or a family of directions $<hkl>$, of the unit cell. Thus, if an index is zero, the plane does not intersect the corresponding axis. By convention, a negative integer is written with a bar over its value (e.g. $\bar{1}$).

This notation is particularly useful for for describing orientations of point defects in materials. Generally, an interstitial will share a lattice site with another matrix atom; this is known as an interstitial dumbbell. The orientation of the dumbbell can be described using the Miller indices; several low-index orientations are shown in Figure 2.
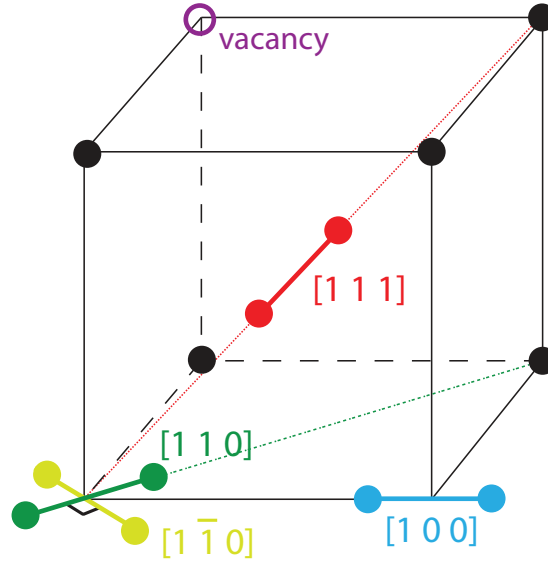
Figure 2: A body-centered cubic (bcc) cell with various orientations and types of point defects.

In the body-centered cubic (bcc) cell, there a matrix atom on every corner of a cube, plus one atom in the center of the cell. In iron, this structure is referred to as α-iron or ferritic iron. This is the structure that is stable below 1670 °F. In α-iron, the $< 1\ 1\ 0 >$ dumbbell is the most stable (lowest energy) interstitial orientation; this is in contrast to other bcc transition metals, in which the $< 1\ 1\ 1 >$ orientation is preferred.

1.1.2 Dislocations

Dislocations are topological irregularities in the crystal structure. There are two main types, edge and screw; additionally, a dislocation can be of mixed character. An edge dislocation can be pictured as a block into which an extra half-plane of atoms has been inserted. A screw dislocation can be generated by making a cut into a block of material, and slipping the atoms on either side relative to each other. The result is a helical structure about the dislocation line (the terminus of the cut in the bulk material). These two structures are illustrated schematically in Figure 3. Dislocations may be of line form, with the ends terminating at grain boundaries or surfaces, or they may be loops, in which they are entirely enclosed within the crystal.

If in a perfect crystal, a closed rectangle in a plane can be drawn about the site of
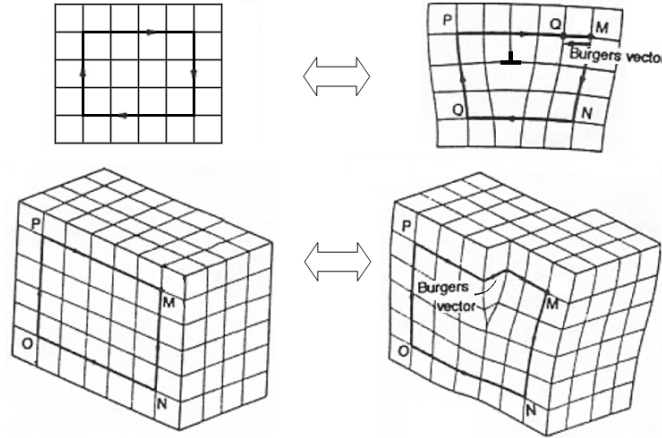
Figure 3: Schematics of the two types of dislocations; edge is on top, screw is on the bottom. Image from Wikimedia Commons via the Creative Commons Attribution–Share Alike 3.0 Unported license.

the dislocation, when the dislocation is present, an attempt to draw the same rectangle will result in a gap in the circuit. The vector required to close this gap is known as the Burgers vector **b**. The relationship between the Burgers vector **b** and the dislocation line ξ characterize the type of dislocation – in an edge dislocation, **b** is perpendicular to ξ, while in a screw dislocation, the two are parallel.

Dislocations strongly affect macroscopic properties. The presence of dislocations lowers the shear stress needed to deform a material, since dislocations may move incrementally through climb and glide. The interactions with other defects affect these processes; for example, some defects may act as pinning sites, while others may be absorbed to aid movement.

1.2 Simulation Methods

The modeling of materials is an inherently multi-scale problem, both in time and length scales (see Figure 4). Smaller scale methods are more accurate because they can capture more of the relevant interactions between atoms. However, they are limited in applicability because of this same feature – the number of atoms goes up, the calculation requires significantly more computational resources to detail all of the interactions. Generally, highly accurate small scale calculations can be used to generate input parameters for larger scale simulations. These larger scale simulations are able to more directly connect with observed

4
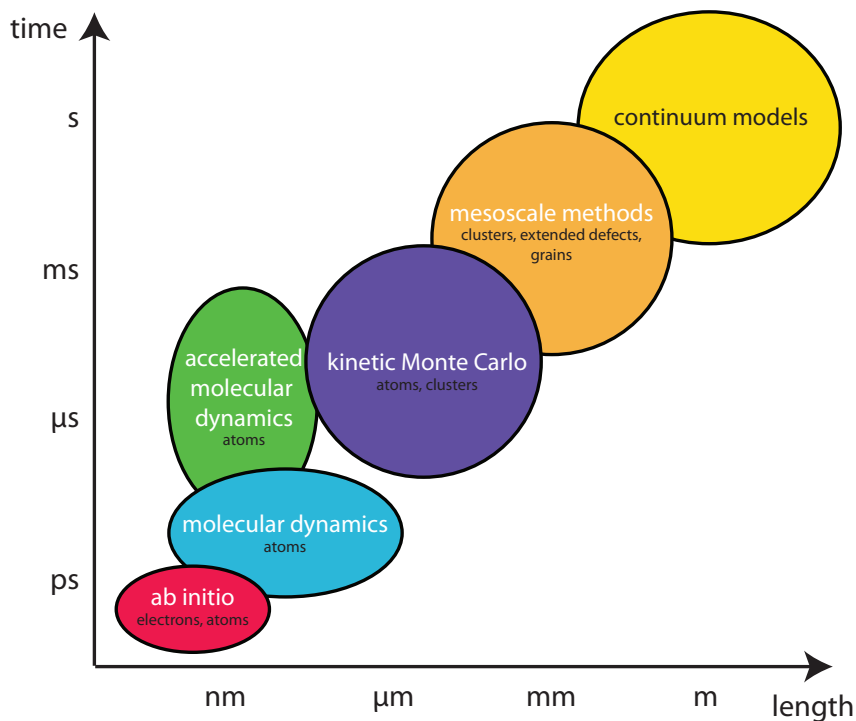
Figure 4: Modeling of materials is an inherently multiscale task. This graph shows the approximate time and length scales over which a particular method is applicable.

phenomena and can (hopefully) be used in predictive capacity. Simulation methods can be categorized by what type of entity is taken as the basic unit for interactions. That is, electronic structure calculations consider individual electrons and atoms, while large scale models may consider entire grains as their basic unit.

First principles, or *ab initio*, methods seek to find a solution to the Schrödinger equation for a group of atoms and to determine the electronic structure. There are a wide variety of methods available to quantum chemists, they vast majority of which rely on the Born-Oppenheimer approximation. This approximation assumes that the motions of the electrons and the nuclei are essentially separable, since the atomic nuclei are much heavier than the electrons. Thus, the ground state of the electrons can be solved based on fixed nuclear positions. Then, the energy of the system for displaced nuclei can be determined.

Density functional theory (DFT) is one very popular *ab initio* method, in which the ground state energy of a group of atoms is a unique functional of the electron density. Minimizing this functional theoretically results in the ground state energy that would be found

by solving the Schrödinger equation. However, finding the appropriate density functional is the challenge of DFT. In practice, this problem is solved for iteratively.

Although *ab initio* methods are extremely valuable, since they consider the most fundamental details of a problem, the most advanced methods in this category are currently limited to several hundred atoms. Molecular dynamics methods are the next step up in time and length scale and can solve for millions of atoms for times of up to microseconds, however they do not solve for electrons directly.

Classical molecular dynamics codes operate on a fairly simple principle. For all the atoms in a system, Newton's equations of motion are solved for known atomic masses and velocities to determine trajectories. The interactions between atoms are described via interatomic potentials, which will be described in more detail in Section 1.2.1. Molecular dynamics is the chosen method for the majority of this work.

Most molecular dynamics calculations have the capacity to model millions of atoms, generally for nanosecond timescales. However, an additional class of methods, known as accelerated molecular dynamics are able to look at even longer timescales. This is particularly useful when the processes one wishes to model are uncommon or infrequent events (e.g. vacancy diffusion). An example of this class of codes is temperature accelerated dynamics [132].

Kinetic Monte Carlo methods may use individual atoms or clusters of atoms as their basic units. These methods rely on probabilities of events occurring to determine the long-time behavior of a system. These probabilities are often based on binding and diffusion energies discovered by the smaller scale methods. At even longer time and length scales, mesoscopic and continuum models follow the behavior of extended defects and grains to develop constitutive models, based on data found in smaller scale simulations.

1.2.1 Interatomic Potentials

Interactions between particles in atomistic simulations are described by functions and parameters known as interatomic potentials. Choosing an appropriate potential is essential for obtaining quality results in any atomistic calculation.

The simplest types of interatomic potentials are pair potentials. Pair potentials are computationally very inexpensive and are often relatively easy to compute. This class of potentials assumes that by summing up all the individual pair bonds the total energy of the solid E_{coh} can be recovered. However, this assumption turns out to be impossible to prove theoretically.

An often used form is the Lennard-Jones (L-J) potential [74], where the potential energy V between particles i and j at a distance r is given by

$$V(r_{ij}) = 4\varepsilon \left[\left(\frac{\sigma}{r}\right)^{12} - \left(\frac{\sigma}{r}\right)^{6} \right]. \tag{1}$$

Here, ε is the depth of the potential well and σ is the distance at which the potential becomes zero. The second term is responsible for the attractive part of the potential, representing the weak van der Waals bond. The first term models strong repulsion at short distances due to electronic overlap; the exponent is given a value of 12 purely for ease of computation, but has no theoretical justification. Similar to other pair potential forms, the L-J potential is inadequate for modeling strongly bonded systems or metals.

At close distances, the repulsion between two nuclei is essentially Coulombic, while at larger distances, the electron clouds of the atoms screen the nuclei. This may be written as

$$V(r_{ij}) = \frac{Z_1 Z_2 e^2}{r} \varphi\left(\frac{r}{a}\right), \tag{2}$$

where Z_1 and Z_2 are the atomic numbers of the two interacting nuclei, e is the charge on an electron, and φ is the screening potential. A commonly used version of this form is the Ziegler-Biersack-Littmark (ZBL) repulsive potential, in which the universal screening function is given by

$$\varphi(x) = 0.1818e^{-3.2x} + 0.5099e^{-0.9423x} + 0.2802e^{-0.4029x} + 0.02817e^{-0.2016x}, \tag{3}$$

and

$$a = \frac{0.8854 a_B}{Z_1^{0.23} + Z_2^{0.23}} \tag{4}$$

where $a_B = 0.529$Å is the Bohr radius. This potential is purely repulsive, but theoretically correct at small distances.

Thus, it is a common practice to create an overall interatomic pair potential for interacting atoms by connecting different types of pair potentials at different distances with polynomial splines. In this way, a potential can be generated which has both long and short range attraction and repulsion that is theoretically correct.

In reality, a many-body potential is needed to account for the influence that bonds between atoms have on each other. To deal with this, the embedded-atom method (EAM) was developed by Daw and Baskes in 1983 [25, 26, 27] for metallic solids. Essentially, each atom is treated as if it were a defect embedded in an electron gas created by the presence of all the other atoms. The cohesive energy of the system can be described in two parts - by an embedding energy and by an electrostatic interaction with a sum over all atoms in the system:

$$E_{coh} = \sum_i G_i \left(\sum_{j \neq i} \rho_j^a(R_{ij}) \right) + \frac{1}{2} \sum_{i,j(j \neq i)} \phi_{ij}(R_{ij})$$

where G is the embedding energy, ρ^a is the spherically averaged atomic electron density, R_{ij} is the distance between atoms i and j, and ϕ is an electrostatic, two-atom interaction. With this formulation, atoms that are near defects or surfaces, for example, will feel a different density profile than atoms in the bulk, allowing the potential to treat significantly more complex systems than pair potentials alone.

While more complex systems can be treated, implementing the method is no more difficult than implementing a pair potential. The functions $G(\rho)$ and $\phi(R)$ can be found either from first principles or using semi-empirical methods. Normally, they are fit to data from a particular (pure) metal, such as lattice constants, elastic constants, or defect formation energies.

A similar method was developed simultaneously by Finnis and Sinclair (FS) [36]. For pure metals, the two methods are exactly equivalent. For alloys, the FS ansatz requires different functionals ρ for interactions between different elements, while EAM uses an averaged one.

To simulate all of the interactions between the three different elements considered in this work, at least six potentials are required. In practice, even more interatomic potentials

were used. The relative merits and properties of all potentials used or considered in this work are discussed in this section.

1.2.1.1   Fe-Fe

The iron-iron interactions in our simulations are described by Ackland's potential [3]. This EAM style potential is a slightly improved form of a potential originally published by Mendelev [83]; we refer to potential #2 of that paper. The original potential is intended to provide an accurate description of both crystalline and liquid iron; thus, it is sensitive to a wide-range of separation distances between atoms. The potential is fit to perfect crystal properties, as well as to forces found from first principles calculations. The new parametrization takes advantage of further *ab initio* calculations performed at small inter-atomic distances with the goal of accurately describing point defect properties. This makes the potential ideal for describing radiation damage events and interactions between defects.

The Ackland potential for Fe-Fe is widely used in radiation damage studies, as it is provides an excellent description of defect behavior. Of course, it is not the only available potential for iron available [95, 93, 2, 31]; even Mendelev et al. provides alternate parameterizations of the above potential which may perform slightly better in particular situations [83]. The potential we choose does not take into account magnetic effects of iron, which may be important in some situations; there are potentials available with the capability [31], however they are currently less suitable for describing defect interactions appropriately than is the potential of Ackland et al.

1.2.1.2   Fe-H and H-H

We take both the iron-hydrogen and hydrogen-hydrogen interactions from Ramasubramaniam et al. [119, 121]. Ramasubramaniam provides two parameterizations of the potential, called A and B. The first takes it's iron-iron interactions from Mendelev's potential #4 [83], while the latter describes Fe-Fe via the improved Ackland potential [3] based on Mendelev's potential #2 [83], the potential we use for Fe-Fe interactions. Thus, potential B is a natural choice for our calculations. Additionally, the authors provide a slightly different version

of potential B, called B′, which is available for download from their website[1], but is not described in detail in the literature. We test both potential B and potential B′, as described in Chapter 3. Potential B is fit to bulk, surface, and vacancy DFT data, while B′ is fit only to bulk and vacancy data, but has better performance regarding strain fields in the bulk.

1.2.1.3   Fe-He

There are many interatomic potentials for the iron-helium system, many of which have come out just in the past several years. These include the "classic" potential of Wilson [155], a three-body potential from Seletskaia et al. [125, 135], and a pair potential from Gao et al. [41].

For this work, we choose to use the purely repulsive pair potential of Juslin and Nordlund [69]. This potential is ideally parameterized to be used along with Ackland's potential for Fe-Fe [3]. For small interatomic distances, calculations of an Fe-He dimer from the DMol97 program package are used. Farther out, the potential is fit to DFT data. The authors caution that potential is not appropriate for molecules, but only for helium within the iron matrix.

1.2.1.4   He-He

Helium is an extremely stable, almost completely inert element. Beck [6] developed a potential for helium-helium interactions given by

$$V(r_{ij}) = A \exp(-\alpha r - \beta r^6) - \frac{0.869}{(r_{ij}^2 + b^2)^3} \left(1 + \frac{2.709 + 3b^2}{r_{ij}^2 + b^2} \right), \tag{5}$$

where $b = 0.675$ Å, $\alpha = 4.390$ Å^{-1}, $\beta = 3.746 \times 10^{-4}$ Å^{-6}, and $A = 398.7$ eV.

Beck fit this potential so that the long-range attraction is theoretically correct, and the short-range repulsion agrees with both experimental and calculated results. Additionally, the depth and shape of the well were determined by a fit to the second virial coefficient, which provides a correction to the ideal gas law for the pressure of a multi-particle system. The potential has its minimum of $V(r) = 8.936 \times 10^{-4}$ eV at $r = 2.969$ Å.

---

[1]http://www.princeton.edu/mae/people/faculty/carter/homepage/research/potentials/

This potential has been used extensively by researchers within the field of nuclear materials; thus, comparison of our results with those of other researchers is straightforward.

1.2.1.5 H-He

We present a new interatomic potential which is suitable for simulating the interactions between hydrogen and helium.

Hydrogen and helium have an extremely weak van der Waals attraction, making this system a good candidate for a L-J potential. Exact quantum mechanical calculations on the system were performed by Bhattacharya and Anderson [9] using a Green's-function Monte Carlo method. They found the H-He potential energy for completely separated atoms as well as for eleven internuclear distances. They compared their results to multiple experimental and *ab initio* studies, with good agreement.

We have fit a Lennard-Jones potential to these data points, finding values of $\varepsilon = 0.0006$ eV and $\sigma = 3.0862$ Å. This gives a maximum well depth of 0.0006 eV (6.96 K) at an interatomic distance of 3.464 Å (6.55 bohr).

In order to simulate the correct short distance repulsion between hydrogen and helium, we connect the Lennard-Jones form to a ZBL form at short distances. An inverse polynomial form is chosen for the spline, and parameters are chosen to guarantee continuity of the potential and its first derivative. The potential energy between a hydrogen atom and a helium atom at distance r is given by

$$
V(r_{ij}) = \begin{cases}
\dfrac{Z_1 Z_2 e^2}{r} \varphi\left(\dfrac{r}{a}\right), & \text{for } r < r_1 \\[2mm]
D_0 + \dfrac{D_1}{r} + \dfrac{D_2}{r^2} + \dfrac{D_3}{r^3}, & \text{for } r_1 \leq r \leq r_2 \\[2mm]
4\varepsilon\left[\left(\dfrac{\sigma}{r}\right)^{12} - \left(\dfrac{\sigma}{r}\right)^{6}\right], & \text{for } r > r_2
\end{cases} \tag{6}
$$

with the fitting parameters found in Table 1, and the screening function φ described in Equations 3 and 4.

$$V(r_{ij}) = 4\varepsilon \left[\left(\frac{\sigma}{r} \right)^{12} - \left(\frac{\sigma}{r} \right)^6 \right]$$
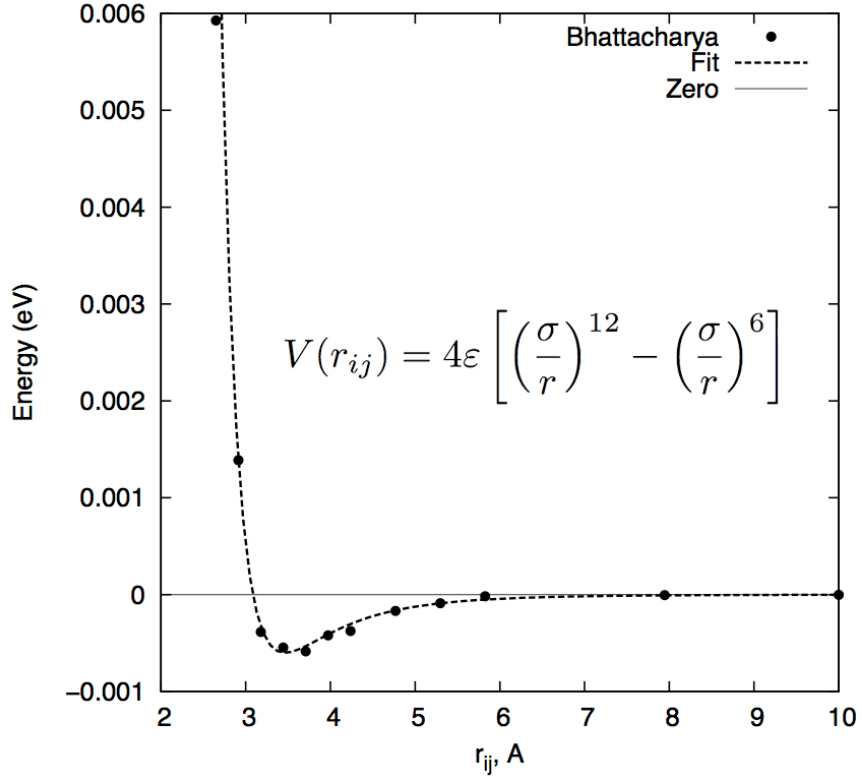
Figure 5: The data points are from Bhattacharya (1994), while the dashed line is our Lennard-Jones fit. The zero energy line is also shown for reference. Values of $\varepsilon = 0.0006$ eV and $\sigma = 3.0862$ Å are used.

Table 1: The parameters for the interatomic potential for hydrogen and helium referenced in Equation 6. Units are eV and Å where appropriate.

D_0	D_1	D_2	D_3	σ	ε	r_1	r_2
-0.318151	1.142826	-0.530526	0.116766	3.0862	0.0006	0.5	2.5

CHAPTER II

SCREW DISLOCATION-DEFECT INTERACTIONS

2.1 Motivation and Literature Review

The interactions of dislocations with intrinsic point defects are of importance in understanding the processes of plasticity, hardening [4], and irradiation creep. Plasticity is enabled through the presence of dislocations, which lower the stress needed to deform a material. Additionally, dislocations act as sinks for point defects, affecting dislocation growth and the subsequent swelling of irradiated materials.

The problem of modeling the effects of dislocations is inherently multiscale, and the motion of dislocations through climb, glide, slip, and cross-slip must be well understood on a microscopic scale in order for larger scale simulations to be properly parameterized [112, 60, 100, 89, 46]. There is a multi-decade history of computer simulation of dislocations; an excellent review of methods is found in Bulatov and Cai [13]. From *ab initio* and molecular dynamics simulations of single dislocation cores and individual point defects, parameters may be found which enable simulations of the interactions between dislocations themselves. Finally, properties found through discrete dislocation simulations, such as hardening parameters, may be used in large scale crystal plasticity models. There are several issues that must be considered when linking simulations of different scales, such as size effects [158, 94]. McDowell [80] and Groh and Zbib [52] provide excellent reviews of the way in which multiscale simulations of dislocations and crystal plasticity may be structured, with the larger scale simulations relying on results from atomistics. Elasticity theory is one of a variety of inputs that are commonly used with the dislocation dynamics methodology. Groh and Zbib point out that a large number of discrete dislocation codes may only be properly applied to isotropic materials [76, 153]. Isotropic elasticity is quite general and easy to implement, thus it is commonly used, if not entirely accurate. Exceptions to this include the anisotropic discrete dislocation code of Rhee et al. [122], which uses anisotropic

expressions at least for short-range interactions, and that of Capolungo et al. for hcp metals [16]. The equations of anisotropic elasticity are much more complex than their isotropic counterparts and, aside from special cases [34], are often applicable to a particular orientation of dislocation and must be solved numerically. These factors necessitate an understanding of where and when theory and approximation may be used successfully, and where detailed effects of atomic structure must be known.

In both isotropic and anistropic continuum dislocation formulations, the strain field of the dislocation becomes singular at the core and must be treated carefully. There are clever solutions in the literature to get around this shortcoming, for example, Cai et al.'s non-singular formulation [15], but they are not in widespread use. Clearly there is a need to characterize the deficiencies of isotropic theory as applied to highly anisotropic materials such as bcc iron, as well as to determine the limitations of the more powerful anisotropic formulation of continuum dislocation elasticity theory.

2.1.1 Core Structure

The determination of the proper structure of the core of a screw dislocation in bcc transition metals is a long standing problem [151]. In recent years, many multibody interatomic potentials have been developed for atomistic simulation of iron, but not all predict the same core structure for a $\frac{1}{2}[1\ 1\ 1]$ screw dislocation. Some predict a degenerate structure, where the relaxed core spreads along three {1 1 0} planes of the <1 1 1> zone. Two possible configurations exist, related by the symmetry operation of the [1 0 $\bar{1}$] diad, and are equivalent in energy. Other potentials predict a compact structure, referred to as the non-degenerate core.

Until recently, the degenerate structure was accepted as accurate [150, 33]. However, recent *ab initio* calculations [37] clearly show the non-degenerate structure to be preferred, and this structure is now believed to be the lowest energy configuration and a general feature of many transition metals [157]. One of the very few available embedded-atom method (EAM) potentials to predict this latter structure, that of Ackland et al. [3], is employed in this work. In fact, non-central forces are the physical cause for this configuration
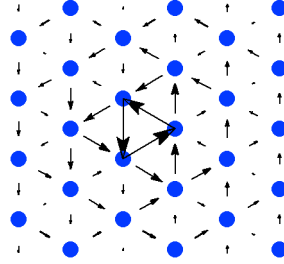
Figure 6: Differential displacement map of the screw core in iron; the non-degenerate structure is recovered.

[148, 149, 93, 51]; the Ackland potential does not explicitly account for this, while other types, including bond-order potentials, do [51]. However, this potential is widely used in the literature and does provide the appropriate core structure; the criteria under which a potential of this type may be guaranteed to generate this core type are described in [22]. Thus, it is useful for comparing the effects of atomic structure vs. those of elastic theory on dislocation-defect interactions. The differential displacement diagram [33] is used to verify that our computational setup results in the non-degenerate structure, as shown in Figure 6. The point of this work is not to definitively determine the energetics of defect-dislocation interactions, but to understand at what point continuum elasticity theory reproduces atomistic results.

2.1.2 Dislocation-Defect Interaction

In this work we seek to intimately examine the differences in interactions between screw dislocations and point defects from linear elastic theory and atomistic simulation, in particular close to the core of a dislocation. The interactions between dislocations and point defects have been elucidated in a number of studies for both screw and edge dislocations using a variety of methods [39, 5, 127, 57], including tight-binding approximations [78, 79] and hybrid methods [129, 128], as well as studies of interactions with impurities [23] and clusters of self-interstitials [75, 111, 110, 154]. Additionally, there have been a number of studies on dislocation glide via the double kink mechanism; different aspects of the nucleation and energy barriers have been simulated in a number of works [150, 30, 20, 48, 19]. We note that core spreading and kink nucleation will be assisted by the absorption of defects within

15

the core. We endeavour to build upon this knowledge by conducting a detailed investigation of the direct interaction of a variety of orientations and types of point defects with a screw dislocation, including calculating interaction energies and performing stability analysis.

We calculate the interaction energy E of intrinsic point defects (vacancies and interstitial dumbbells) with screw dislocations in alpha-iron. First, using the dipole force tensor and the dislocation strain field, we calculate the interaction energy using continuum methods as discussed below. Second we perform atomistic calculations of the defect-dislocation interaction which incorporates the dislocation core explicitly. A defect is introduced near a dislocation, the energy of this ensemble of atoms minimized and the interaction energy is directly determined by comparing this energy to that of a defect far away from a dislocation. Of these two methods, the first does not contain any description of the dislocation core, while the other explicitly accounts for the atomic structure of the core. Thus, in order to determine the effects of the dislocation core structure, we compare these two methods of calculating the interaction energy.

2.2 Linear Elasticity Theory

Meissner et al. [82] derived the dislocation defect interaction energy from the dipole tensor and the dislocation strain field in a general anisotropic medium. This model was the basis of the work by Tomé et al. [144] in which the interaction energy in hexagonal close packed materials was studied near edge and screw dislocations. Both of these papers used lattice Green's functions to calculate the dipole tensors. Additional works invoking this theoretical framework and the model of point defects diffusion of Dederichs and Schroeder [28] include those of Tomé et al. [143], Monti et al. [88], and Smetniansky-de Grande et al. [130].

In this formulation, the interaction energy between the point defect and a dislocation separated by a distance $\mathbf{r}$ is given by

$$E(\mathbf{r}) = -\varepsilon_{ij}(\mathbf{r})P_{ij} \tag{7}$$

where $\boldsymbol{\varepsilon}$ is the strain field of the dislocation and P_{ij} are components of the dipole force tensor $\mathbf{P}$, which will be discussed in the following section.[1]The strain field of the dislocation

can be calculated from the displacement field as:

$$\varepsilon_{ij} = \frac{1}{2}\left(\frac{\partial u_i}{\partial x_j} + \frac{\partial u_j}{\partial x_i}\right). \tag{8}$$

At large separation distances, where the defect is far enough away from the dislocation to feel no influence, the interaction energy $E = 0$.

When we wish to compare to atomistics, it is convenient to add another term to Equation 7, so that

$$E(\mathbf{r}) = -\varepsilon_{ij}(\mathbf{r})P_{ij} + E_{defect}. \tag{9}$$

E_{defect} is an additional energy accounting for different types of configurations of the same type of defect. This term is especially relevant for interstitial dumbbells. In bcc iron, the <1 1 0> dumbbell configuration is the lowest energy interstitial defect. Other orientations are higher energy structures, so the addition of E_{defect} for the higher energy structures, relative to the lowest energy structure, allows all interaction energies for a given type of defect to be compared on equal footing. This term is equal to the additional formation energy required to form the defect of interest, above what is required for a <1 1 0> dumbbell. With the interatomic potential we are using, the formation energy for a <1 1 0> dumbbell is 3.53 eV, 4.34 eV for a <1 0 0> dumbbell, and 4.02 eV for a <1 1 1> dumbbell [83]. Thus, $E_{defect}^{<1\,1\,0>} = 0.0$ eV, $E_{defect}^{<1\,1\,1>} = 0.49$ eV and $E_{defect}^{<1\,0\,0>} = 0.81$ eV. In this way, all interaction energies for interstitials can be compared directly.

2.2.1 Dipole Tensor

The dipole force tensor describes the influence that a point defect, either a vacancy or interstitial, has on its neighbors in otherwise perfect bulk material. It may be calculated using different methods [47]; in this case it is calculated by

$$P_{ij} = \sum_{k=1}^{N}[S_i^{(k)} + d_i^{(k)}]F_j^{(k)}, \tag{10}$$

---

[1]It is important to make sure all calculations and comparisons are done in the same coordinate system. For example, dipole tensors are given in the crystal coordinate system, while strain fields are given, and atomistics are performed, in the dislocation coordinate system. First and second order tensors can be transformed between the crystal and dislocation systems by $\mathbf{v}^C = \mathbf{T}\mathbf{v}^D$, and $\mathbf{P}^C = \mathbf{T}\mathbf{P}^D\mathbf{T}^\mathsf{T}$ where $\mathbf{T}$ is the transformation matrix, which contains the normalized vectors of the dislocation coordinate system as its columns.

Table 2: The components of the dipole tensor **P** for a variety of point defects, expressed in crystal axes.

defect type	P_{11}	P_{22}	P_{33}	P_{12}	P_{13}	P_{23}
vacancy	-2.7119	-2.7119	-2.7119	0.00	0.00	0.00
[1 1 0] dumbbell	10.2056	10.2056	10.9080	4.7428	0.00	0.00
[1 0 0] dumbbell	8.7977	8.1689	8.1689	-1.0332	-1.0332	2.9766
[1 1 1] dumbbell	8.5493	8.5493	8.5493	4.6977	4.6977	4.6977

where the summation is over N neighbors of the defect, **S** denotes the perfect lattice position of a neighbor with respect to the defect, **d** is the displacement from the perfect lattice position caused by the defect's presence, and the Kanzaki force, **F**, is defined as the force that must be applied to maintain the displaced structure when the defect is removed. The Kanzaki force is equivalently the component of the total force that the defect exerts on a neighbor when in the relaxed configuration. For a specific potential these quantities can be calculated with Green function methods or directly with molecular statics.

In this work, the latter method is used. Atomistic simulations are performed in which a defect is introduced into a perfect lattice. Conjugate gradient minimization is used to relax the lattice. Care must be taken that the lattice is fully relaxed; this is ensured by requiring that no component of force on any atom is larger than 1×10^{-9} eV/Å. An interstitial dumbbell with the neighboring atoms after relaxation is depicted in Figure 7(a). Then, the defect is removed and the lattice restored to its original state, but with the neighbors maintaining their displacements, as shown in Figure 7(b). The force produced by the defect site on the neighbors can then be calculated; it is equal in magnitude but opposite in sign to the force produced by the defect itself. In the calculations which follow, we use the LAMMPS molecular dynamics code [113] and the clsman atomistic code developed at Los Alamos National Laboratory. The six independent components of the symmetric tensors **P** are given in Table 2 for four types of defects: the vacancy and three configurations of the interstitial ([1 1 0], [1 0 0], and [1 1 1] dumbbells). Convergence testings were performed to ensure that a sufficient number of neighbor shells were included in the calculations; at least nine neighbor shells (approx. 2.5 Å) beyond the defect were included.

(a) A defect displaces its neighbors by a distance **d** when the system is relaxed.

(b) When the defect is removed, a force **F** is required to hold the neighbors in their displaced positions.
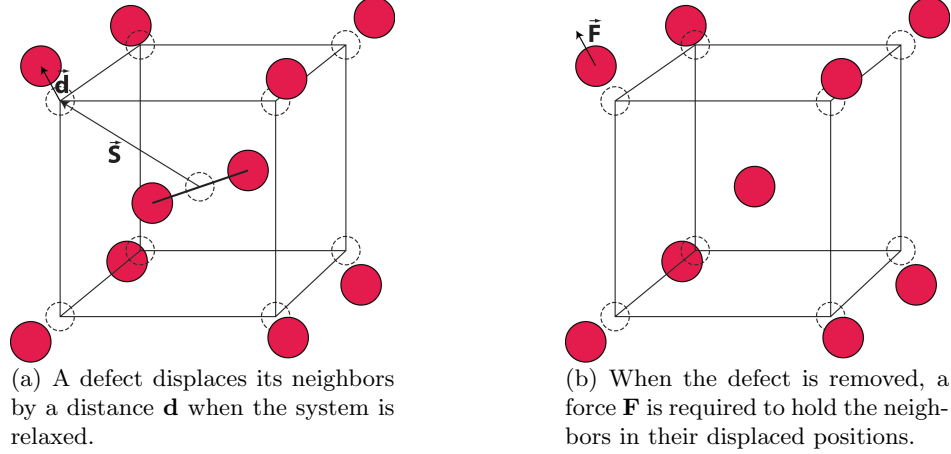
Figure 7: Schematic of the quantities used when calculating the dipole tensor for a generic defect in a bcc lattice. Dotted circles denote perfect lattice positions. Red circles denote displaced atom positions caused by the presence of the defect.

2.2.2 Strain Fields

The strain field may be formulated isotropically or anisotropically. The isotropic formulation is well-known and generally may be applied to any generic screw dislocation. On the other hand, the anisotropic formulation must be derived for a particular orientation of the dislocation.

For any isotropic medium, a screw dislocation results in displacement along the x_3 direction only, given by:

$$u_3 = \frac{b_{x_3}}{2\pi} \tan^{-1} \frac{x_2}{x_1}, \tag{11}$$

where b_{x_3} is the magnitude of the Burgers vector and ξ lies along the x_3 axis [60]. There are no displacements in the directions perpendicular to the dislocation line. Thus, $\varepsilon_{11} = \varepsilon_{22} = \varepsilon_{33} = \varepsilon_{12} = 0$, and the non-zero symmetric strain field components are

$$\varepsilon_{13} = -\frac{b_{x_3}}{4\pi r^2} x_2$$

$$\varepsilon_{23} = \frac{b_{x_3}}{4\pi r^2} x_1.$$

For the anisotropic formulation, the equations needed to generate a <1 1 1> screw dislocation are given by Hirth [59], based on the solutions of Eshelby, Read, and Shockley [34], Stroh [136], and Head [56].

Note that the equations in this section apply to the coordinate system where $x_1 = [\bar{1}\,2\,\bar{1}]$, $x_2 = [\bar{1}\,0\,1]$, and $x_3 = [1\,1\,1]$. Hirth [59] assumes that the dislocation line ξ lies in the negative x_3 direction, that is, the $[\bar{1}\,\bar{1}\,\bar{1}]$ direction. The equations can be used to describe right or left handed dislocations, with a negative or positive Burgers vector, respectively.

The elastic constants in the dislocation coordinate system C_{ij} are defined in terms of the standard elastic constants C_{ij}^0 from the crystal coordinate system, and in terms of the anisotropy factor $H = 2C_{44}^0 - C_{12}^0 - C_{11}^0$. Their values are given by

$$C_{11} = C_{11}^0 + H/2 \qquad\qquad C_{44} = C_{44}^0 - H/3$$

$$C_{12} = C_{12}^0 - H/6 \qquad\qquad C_{66} = C_{44}^0 - H/6$$

$$C_{13} = C_{12}^0 - H/3 \qquad\qquad C_{15} = -\sqrt{2}H/6$$

$$C_{33} = C_{11}^0 + 2H/3 \qquad\qquad 2C_{66} = C_{11} - C_{12}.$$

For a right handed dislocation in the x_3 direction Hirth gives the displacements as

$$
u_1 = -\frac{b_{x_3}}{6\pi}\left\{\tan^{-1}\left(\frac{Fx_2}{x_1}\right) - \frac{1}{2}\tan^{-1}\left(\frac{4Fx_2}{J_1x_1 - \sqrt{3}J_3x_2}\right) - \frac{1}{2}\tan^{-1}\left(\frac{4Fx_2}{J_1x_1 + \sqrt{3}J_3x_2}\right)\right\}
$$
$$
\times (A+B) - \frac{\sqrt{3}b_{x_3}}{12\pi}\left\{\ln\left(\frac{J_1x_1^2 + J_2x_2^2 - 2\sqrt{3}J_3x_1x_2}{J_1}\right)^{1/2}\right.
$$
$$
\left. - \ln\left(\frac{J_1x_1^2 + J_2x_2^2 + 2\sqrt{3}J_3x_1x_2}{J_1}\right)^{1/2}\right\} \times BF, \tag{12}
$$

$$
u_2 = -\frac{\sqrt{3}b_{x_3}}{12\pi}\left\{\tan^{-1}\left(\frac{4Fx_2}{J_1x_1 - \sqrt{3}J_3x_2}\right) - \tan^{-1}\left(\frac{4Fx_2}{J_1x_1 + \sqrt{3}J_3x_2}\right)\right\} \times (A+B)
$$
$$
- \frac{b_{x_3}}{6\pi}\left\{\ln(x_1^2 + F^2x_2^2)^{1/2} - \frac{1}{2}\ln\left(\frac{J_1x_1^2 + J_2x_2^2 - 2\sqrt{3}J_3x_1x_2}{J_1}\right)^{1/2}\right.
$$
$$
\left. - \frac{1}{2}\ln\left(\frac{J_1x_1^2 + J_2x_2^2 + 2\sqrt{3}J_3x_1x_2}{J_1}\right)^{1/2}\right\} \times BF, \tag{13}
$$

$$
u_3 = -\frac{b_{x_3}}{6\pi}\left\{\tan^{-1}\left(\frac{Fx_2}{x_1}\right) + \tan^{-1}\left(\frac{4Fx_2}{J_1x_1 - \sqrt{3}J_3x_2}\right) + \tan^{-1}\left(\frac{4Fx_2}{J_1x_1 + \sqrt{3}J_3x_2}\right)\right\}. \tag{14}
$$

where

$$F = \frac{(R+1)^{1/3} + (R-1)^{1/3}}{(R+1)^{1/3} - (R-1)^{1/3}} \qquad\qquad R^2 = \frac{C_{66}(C_{11}C_{44} - C_{15}^2)}{C_{11}(C_{44}C_{66} - C_{15}^2)}$$

$$J_1 = 1 + 3F^2 \qquad\qquad J_6 = C_{44}/C_{15}$$

$$J_2 = 3 + F^2 \qquad\qquad J_7 = (C_{15}S_{44})^{-1}$$

$$J_3 = 1 - F^2 \qquad\qquad J_8 = (F^2 C_{11} + C_{12})^{-1}$$

$$J_4 = (C_{12} + C_{66})/(C_{15}S_{44}) \qquad\qquad A = J_6 - (J_2 J_7 / J_1)$$

$$J_5 = [C_{44}(C_{12} + C_{66}) - 2C_{15}^2]/C_{15} \qquad\qquad B = J_8[(J_2 J_4 / J_1) - J_5]$$

$$S_{44} = C_{66}/(C_{44}C_{66} - C_{15}^2).$$

Using Equation 8, we can calculate the components of the strain field:

$$\frac{\partial u_1}{\partial x_1} = -\frac{b_{x_3}}{6\pi}\left\{\frac{2FJ_1 x_2}{D_+} + \frac{2FJ_1 x_2}{D_-} - \frac{Fx_2}{G}\right\} \times (A+B) - \frac{\sqrt{3}b_{x_3}}{12\pi}\left\{\frac{K_-}{M_-} - \frac{K_+}{M_+}\right\} \times BF$$

$$\frac{\partial u_1}{\partial x_2} = -\frac{b_{x_3}}{6\pi}\left\{-\frac{2FJ_1 x_1}{D_+} - \frac{2FJ_1 x_1}{D_-} + \frac{Fx_1}{G}\right\} \times (A+B) - \frac{\sqrt{3}b_{x_3}}{12\pi}\left\{\frac{L_-}{M_-} - \frac{L_+}{M_+}\right\} \times BF$$

$$\frac{\partial u_2}{\partial x_1} = -\frac{b_{x_3}}{6\pi}\left\{\frac{K_+}{2M_+} + \frac{K_-}{2M_-} - \frac{x_1}{G}\right\} \times (BF) - \frac{\sqrt{3}b_{x_1}}{12\pi}\left\{\frac{4FJ_1 x_2}{D_+} - \frac{4FJ_1 x_2}{D_-}\right\} \times (A+B)$$

$$\frac{\partial u_2}{\partial x_2} = -\frac{b_{x_3}}{6\pi}\left\{\frac{L_+}{2M_+} + \frac{L_-}{2M_-} - \frac{F^2 x_2}{G}\right\} \times (BF) - \frac{\sqrt{3}b_{x_3}}{12\pi}\left\{\frac{4FJ_1 x_1}{D_-} - \frac{4FJ_1 x_1}{D_+}\right\} \times (A+B)$$

$$\frac{\partial u_3}{\partial x_1} = -\frac{b_{x_3}}{6\pi}\left\{-\frac{4FJ_1 x_2}{D_+} - \frac{4FJ_1 x_2}{D_-} - \frac{Fx_2}{G}\right\}$$

$$\frac{\partial u_3}{\partial x_2} = -\frac{b_{x_3}}{6\pi}\left\{\frac{4FJ_1 x_1}{D_-} + \frac{4FJ_1 x_1}{D_+} + \frac{Fx_1}{G}\right\} \qquad (15)$$

where

$$L_\pm = J_2 x_2 \pm \sqrt{3}J_3 x_1$$

$$K_\pm = J_1 x_1 \pm \sqrt{3}J_3 x_2$$

$$M_\pm = J_1 x_1^2 + J_2 x_2^2 \pm 2\sqrt{3}J_3 x_1 x_2$$

$$D_\pm = 16F^2 x_2^2 + K_\pm$$

$$G = (x_1^2 + F^2 x_2^2)^{-1}$$

and $\partial u_1/\partial x_3 = \partial u_2/\partial x_3 = \partial u_3/\partial x_3 = 0$.

The elastic constants we use in our calculations have the values $C_{11}^0 = 243.4$ GPa, $C_{12}^0 = 145.0$ GPa, and $C_{44}^0 = 116.0$ GPa. These numbers come from the interatomic

21
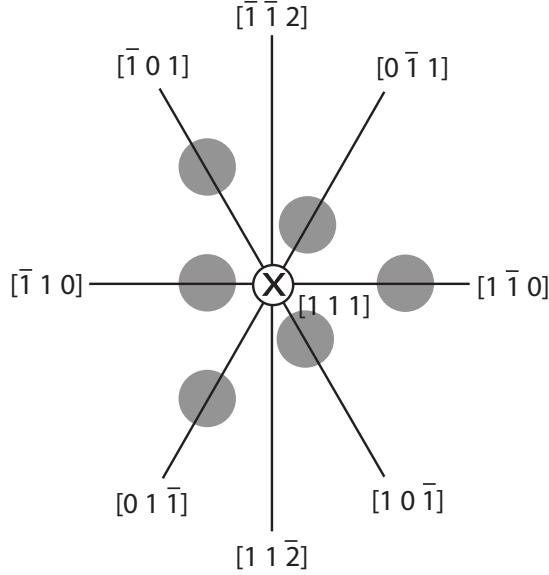
Figure 8: The coordinate system for the screw dislocation, with the [1 1 1] direction pointing into the page. The orientation of all figures in this paper correspond to this system. The dislocation line ξ and the Burgers vector **b** point along the [1 1 1] direction, resulting in a right-handed dislocation. The atoms that comprise the core are shown as grey circles.

potential we use in this work, where they were parameters used in the fitting procedure [83].

2.3 Atomistic Simulation

The coordinate system used in describing our results is shown in Fig. 8. The [1 1 1] direction is into the page. Both the dislocation line vector ξ and the Burgers vector **b** point in the same direction along the x_3 axis, resulting in a right-handed dislocation.

Our system is cylindrical, with periodic boundary conditions in the direction of the dislocation line. The box size is approximately 37.1 Å in the periodic direction, and the cylinder has a radius of approximately 100 Å. Initial displacement of all atoms is performed according to linear elastic theory. An outer shell of atoms (approximately 20 Å) is then frozen, while the core is allowed to relax. The resulting core structure was identical when either isotropic or anisotropic displacement expressions were used for the initial displacements.

We introduce defects into the simulation box in a systematic way. First, an individual iron atom is replaced by a defect, either by removing it for a vacancy, or shifting it and

introducing an additional atom for an interstitial dumbbell. The energy of the system is minimized, while keeping the outer shell frozen, to obtain the relaxed structure containing the defect. The energy of the system is then measured. This process is repeated, starting from the initial dislocation structure without defects, for each unique atomic site within the simulation box. In this way, the interaction energy can be calculated between a defect and the dislocation as a function of their relative positions.

2.4   Results

Interaction energy from atomistics is calculated by the following formula:

$$E_{int} = [E_D^d + E_0] - [E_D + E_0^d]. \tag{16}$$

All energies are total energies of the ensemble system, where the D subscript indicates a system containing a dislocation, the 0 subscript indicates a single crystal system, and a d superscript indicates that the defect of interest is contained in the system. The energy of the system containing both the dislocation and the defect given by atomistic calculation (E_D^d) includes the energy of formation for both the dislocation and the defect. Thus, in order to extract out just the interaction energy, the last two terms must be subtracted. Additionally, E_0 is added back to the equation for balance of atoms. With this definition, a negative interaction indicates that the defect is attracted to the dislocation.

Our system contains 100095 atoms, of which 36090 are frozen, before defects are introduced. Thus, $E_0 = -399082.256$ eV and $E_D = -399043.396$ eV. E_0^d is dependent on the type of defect. For a vacancy, $E_0^d(V) = -399076.522$ eV. For all types of interstitials considered, the interaction energies are relative to the lowest energy interstitial in the bulk crystal, the <1 1 0> dumbbell, which gives $E_0^d(I) = -399082.740$ eV. This also allows for direct comparison of the energies between all atomistic results. E_D^d is determined by the atomistic results for each position and defect.

Note that in all figures showing basic interaction energies for atomistic data, the interaction energy scale bar runs from -0.5 eV to 0.5 eV, even when most of the data for a particular figure does not approach these limits. This was done so that interaction energies from atomistics could be easily intuitively compared across all defect configurations. In the

remainder of this section, we will describe the results from atomistic and continuum theory for <1 1 0>, <1 1 1>, and <1 0 0> dumbbell configurations, and for vacancies.

2.4.1   <1 1 0> Dumbbell

The <1 1 0> type dumbbell is known to be the most stable interstitial configuration in the bulk in bcc iron, in contrast to many other bcc metals in which crowdions are the most stable configuration. In our dislocation coordinate system, not all members of the <1 1 0> family are created equal with respect to their orientation to the dislocation. A $[1\ \bar{1}\ 0]$ dumbbell lies perpendicular to the dislocation line, along the x-axis of figure 8, while a $[1\ 1\ 0]$ dumbbell makes an angle of $\sim 35°$ with the core. We define

$$< 1\ \bar{1}\ 0 > \equiv \{[1\ \bar{1}\ 0], [1\ 0\ \bar{1}], [0\ 1\ \bar{1}], [\bar{1}\ 1\ 0], [\bar{1}\ 0\ 1], [0\ \bar{1}\ 1]\} \tag{17}$$

to differentiate those specific dumbbells which are perpendicular to the dislocation line from those of the general <1 1 0> family, and use

$$< 1\ 1\ 0 >^{+} \equiv \{[1\ 1\ 0], [1\ 0\ 1], [0\ 1\ 1]\} \tag{18}$$

to indicate only those members which have all positive components, and thus have some extent along the core.

We begin by calculating energetics for $[1\ \bar{1}\ 0]$ dumbbells; the results are shown in Figure 9. The dumbbell lies on the horizontal axis, with no extent into the page. A clear pattern of positive and negative interaction energies emerges from the atomistic simulations. The most negative interaction energies are seen to the left of the core, while to the right, the most positive energies are seen. Bands of slightly negative interaction energy are seen in the $[0\ \bar{1}\ 1]$ and $[1\ 0\ \bar{1}]$ directions, and slightly positive bands are seen in the $[\bar{1}\ 0\ 1]$ and $[0\ 1\ \bar{1}]$ directions. This pattern reflects the non-degenerate core structure of the screw dislocation in bcc iron. Even at the angles at which the long-range interaction energy is positive (repulsive), within about 5-8 Å of the core, all interaction energies are negative. This indicates that if a defect travels close enough to the core from any direction, it will ultimately be attracted instead of repelled. As can be seen in Figure 9, there are five lattice sites in the core (white area) at which the dumbbell is unstable and is spontaneously

absorbed into the core under minimization. This results in a much lower energy structure, off the scale in Figure 9, which will be discussed later.

When we compare these atomistic results to those from elasticity theory, we find several discrepancies. The anisotropic strain field is able to replicate the pattern of negative and positive interaction energies (given by Eq. 9) around the core, although the magnitude of the interactions is underestimated. Also, anisotropic elasticity theory does not predict the negative energies very near the core in all directions that we see from atomistics. The absolute error and absolute percentage error (referenced to the atomistic solution) between atomistics and anisotropic elasticity theory can be seen in Figure 10. To the right and left of the core, where the interaction energies have the largest magnitude, the absolute error is greatest. However, these areas have some of the lowest relative errors. In areas of very small magnitude interaction energy, the percentage error is very significant, but errors in these regions would be of little practical significance. In the core, as we would expect, the error approaches 1 eV, but outside of the core the error rarely exceeds 0.1 eV. Even so, the percentage errors are quite large (between about 10 and 50% in significant regions of strong interaction energy). Overall, anisotropic theory agrees qualitatively with atomistics outside of the core region, but has large errors quantitatively.

The results from anisotropic theory are significantly better than those from isotropic theory (Figure 9). Isotropic theory simply predicts a clear divide between positive and negative interaction energies at the y-axis and does not account for the non-degenerate core structure at all.

These results can be generalized for any $<1\,\bar{1}\,0>$ dumbbell. The pattern of interaction energy seen in Figure 9 will appear rotated by 120° for other dumbbells of this type, with the strongest positive and negative interaction energies appearing when the dumbbell is pointed directly towards the core.

A [1 1 0] dumbbell was also examined; results are shown in Figure 11. This dumbbell displays three regions of negative interaction energy, and three regions of positive/repulsive interaction. In contrast to the [1 $\bar{1}$ 0], however, all three regions are the same size, displaying a symmetry when looking down the dislocation line. Additionally, the magnitudes of the
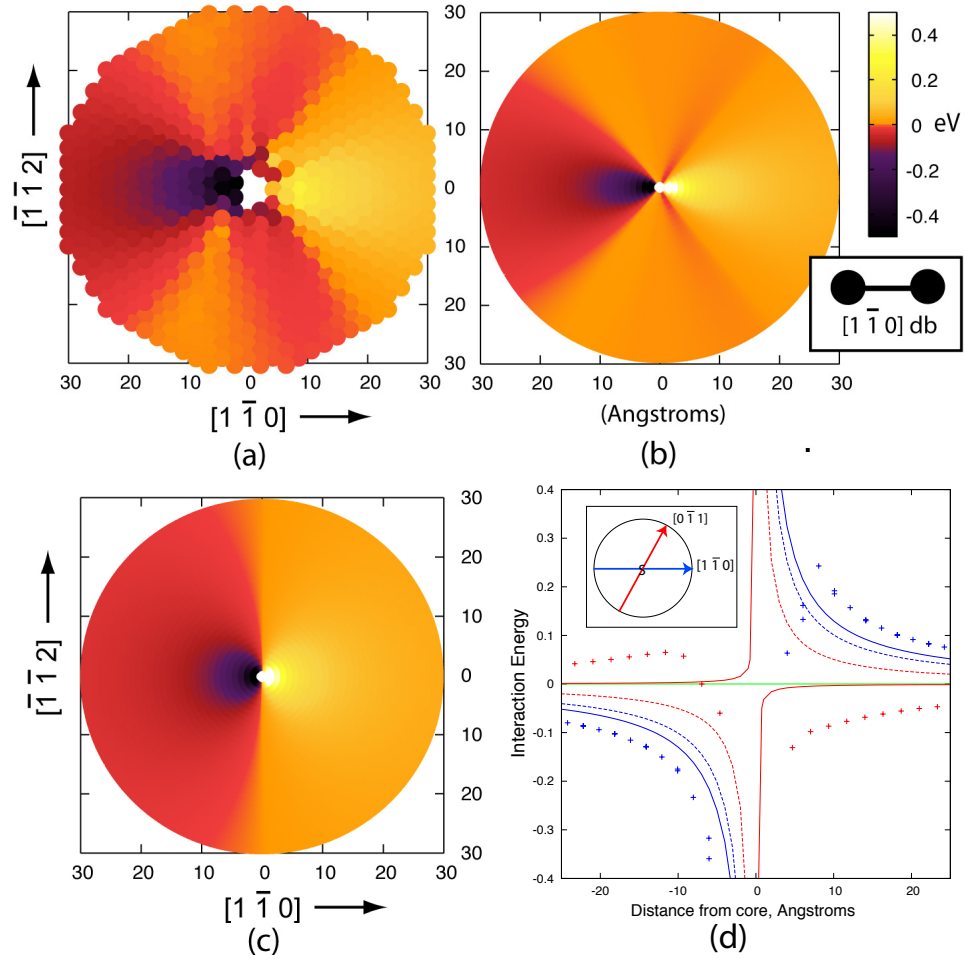
Figure 9: Plots of the interaction energy of a $[1\,\bar{1}\,0]$ dumbbell with the dislocation core as a function of distance and angle from the dislocation. In all figures, the core is centered at (0,0), and the numbers on the axes show distance from the core in Angstroms. Interaction energies are plotted by color, in eV. (a) shows the interaction energies calculated directly from atomistics. (b) shows E calculated with elasticity theory, using Equation 9 with the anisotropic strain field, with the dipole tensor **P** calculated using atomistic methods. (c) shows the interaction energy calculated with elasticity theory using the isotropic strain field. (d) shows profiles of the interaction energy along the directions indicated in the inset circle. As the interstitial position varies along the $[1\,\bar{1}\,0]$ direction (blue) and the $[0\,\bar{1}\,1]$ direction (red) the interaction energy is plotted. Dotted lines indicate isotropic results, solid lines indicate anisotropic results, and points show atomistic results. The anisotropic strain field results in interactions of the same sign as those shown by atomistics, even when the magnitude is in disagreement; however the results when using the isotropic strain field does not even have this property.

26
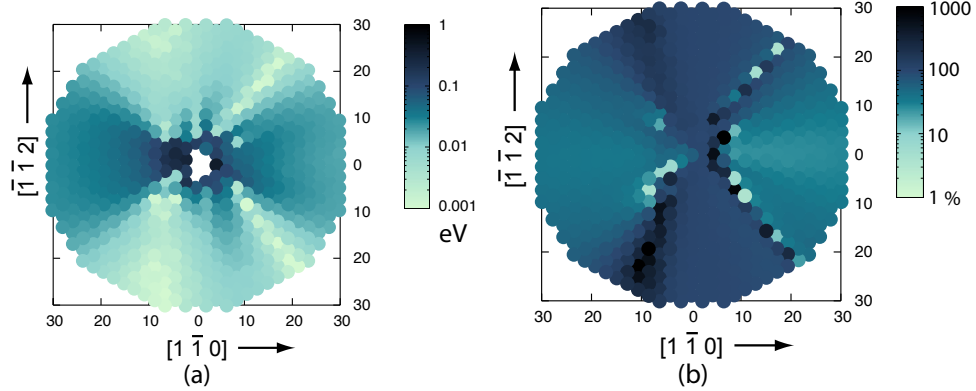
Figure 10: (a) shows the absolute error in eV between the atomistic and anisotropic elasticity theory results for the [1 $\bar{1}$ 0] dumbbell. (b) shows the absolute value of the percent error between the atomistic and anisotropic elasticity theory results with respect to the atomistic calculations for the same dumbbell. The same coordinate system that is used in Figure 9 is used here.

interactions are weaker than for the [1 $\bar{1}$ 0] dumbbell. Essentially, this indicates that a member of the <1 $\bar{1}$ 0> family is energetically preferred over a <1 1 0>$^+$ in the regions where negative interaction energy is seen (the [$\bar{1}$ 1 0], [1 0 $\bar{1}$], and [0 $\bar{1}$ 1] directions). However, in the other regions where a positive interaction is observed, a <1 1 0>$^+$ may be preferred since its interaction is less repulsive than that of a <1 $\bar{1}$ 0>.

2.4.2   <1 1 1> Dumbbell

The <1 1 1> family of dumbbells is not as energetically favorable in the bulk as the <1 1 0>, but more so than the <1 0 0> family. However, the pattern of energetic favorability may change near a strong strain field such as that of a dislocation. [1 1 1] dumbbells, which lie parallel to the dislocation line, are introduced at each lattice site about our screw dislocation core (one at a time) and subsequently minimized.

After an analysis of the minimized structures, it is clear that the [1 1 1] dumbbell is not a stable configuration everywhere, as illustrated in Figure 12. We map the final dumbbell type by color, using an algorithm that can distinguish between families of directions, but does not account for permutations within a family (for example, a [1 1 0] and a [1 $\bar{1}$ 0] will both appear green). We find that half of the dumbbells convert to <1 1 0>-type structures, while the other half lie somewhere between <1 1 1> and <2 1 1>; they have a <1 1 1>
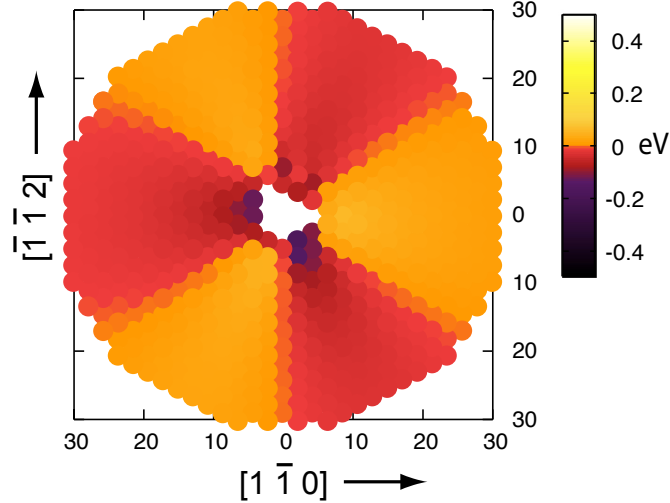
Figure 11: The interaction energies between a [1 1 0] dumbbell and a screw dislocation core are shown as a function of of distance and angle from the dislocation core. The same conventions as in Figure 9 are used. Note that the magnitude of interactions is not as strong as for the [1 $\bar{1}$ 0] orientation.

that is slightly twisted to conform with the helical structure of the screw dislocation. This can be explained by comparing to our above results for [1 $\bar{1}$ 0] dumbbells.

In the regions where it is most energetically favorable to have a dumbbell from the <1 1 0> family, we also obtain a <1 1 0> structure when starting with a [1 1 1] dumbbell structure. Looking at individual dumbbells from the <1 1 0> regions, we find that dumbbells convert to <1 1 0>$^+$ structures instead of <1 $\bar{1}$ 0>, due to the smaller degree of rotation needed, or the relative closeness of the two structures. In the regions where a <1 1 0> dumbbell was shown to have a positive interaction energy with respect to the dislocation, [1 1 1] dumbbells rotate away from being perfectly aligned with the core, but do not convert to <1 1 0>-type. Dumbbells very near the core appear to stay in [1 1 1] configurations, but this is really an artifact of their being absorbed into the core, creating a crowdion-like structure along the dislocation line.

Interaction energies from atomistics for the [1 1 1] dumbbell calculations can be seen in Figure 13. As described above, all interaction energies are referred to the <1 1 0> structure, so results from all atomistics calculations of interstitials can be compared directly. In the regions where dumbbells rotated to the [1 1 0] shape, interaction energies are negative.

28
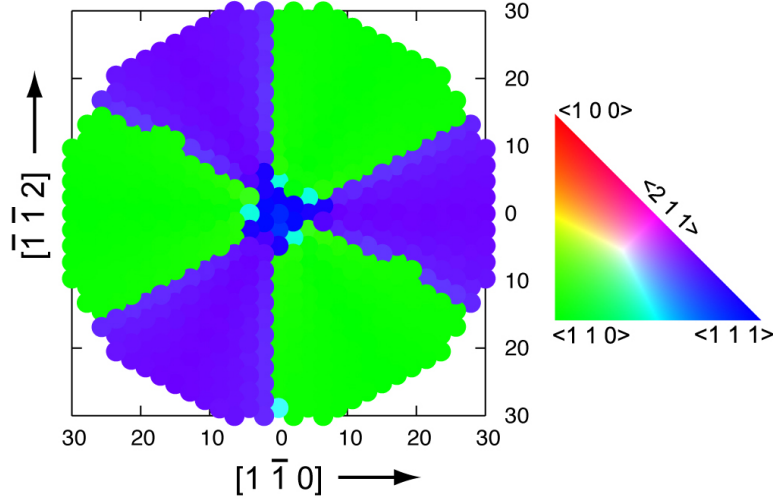
Figure 12: [1 1 1] dumbbells are placed at various angles and positions about the dislocation core and minimized; their final orientations are shown by color. Approximately one half end up as <1 1 0>-type; the other half remain strongly <1 1 1> with some reorientation to align with the helical structure of the screw dislocation.

Where the dumbbells rotated only slightly, interaction energies remain strongly positive, while negative energies result when the dumbbell achieves the more stable configuration. The missing lattice sites near the core indicate where a dumbbell was absorbed in the dislocation, resulting in the low energy core structure.

Results from elasticity theory (Equation 9) are shown in Figure 14. Again, anisotropic theory reveals the non-degenerate core structure while isotropic theory neglects it. In fact, isotropic theory predicts almost no interaction at all. Because of the addition of the $E_{defect}^{<1\ 1\ 1>} = .48$ to the interaction energies, results from theory are referenced identically to those from atomistics, and the results can easily be compared. Where our atomistics show rotation to <1 1 0> structures, the theory indicates interaction energies slightly below 0.48 for the [1 1 1]. Dumbbells in these regions feel an attraction to the core which results in their reorientation to a more energetically favorable configuration. Thus, while anisotropic elasticity does not explicitly predict the spontaneous rotation of <1 1 1> dumbbells, the preference for that rotation is present in the interaction energies of the <1 1 1> dumbbell with the dislocation. Higher interaction energies are seen in the regions where no reorientation is observed atomistically.

Figure 13: The interaction energies between what are originally [1 1 1] dumbbells and a screw dislocation core are shown as a function of of distance and angle from the dislocation core. The same conventions as in Figure 9 are used. In the red regions, dumbbells convert to the more energetically favorable <1 1 0>-type.

(a)

(b)
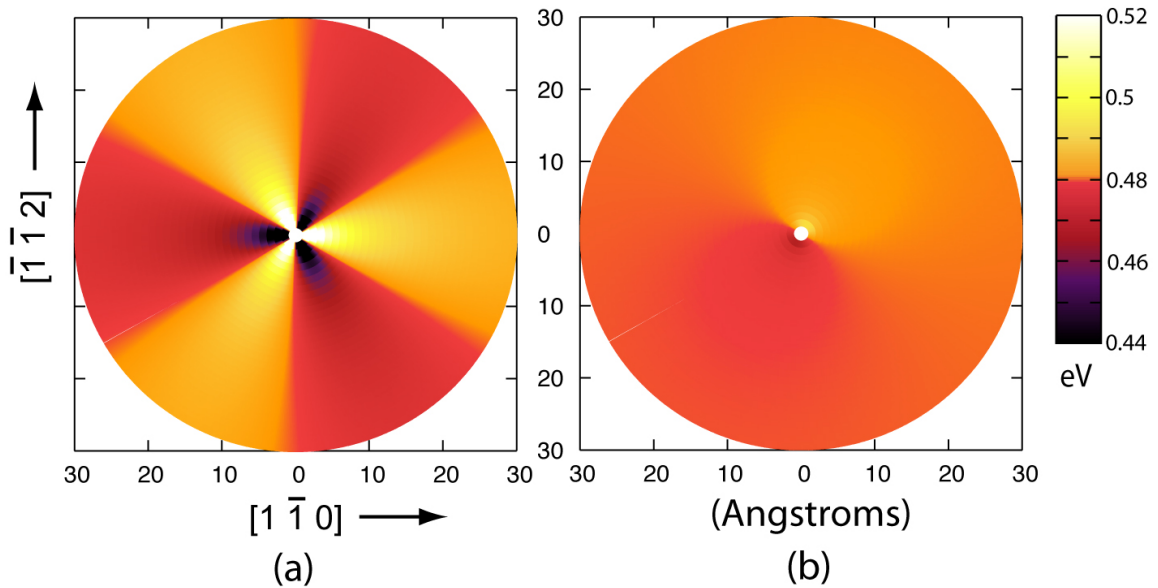
Figure 14: Interaction energies from elasticity theory (including the E_{defect} term of Eq. 9) for a [1 1 1] dumbbell. Results using the anisotropic strain field are shown in (a); isotropic is shown in (b). Note that the energy is scaled differently than in previous plots, but quantitatively may be compared directly.

Although anisotropic elasticity theory provides a glimpse into the energetics near the core, it is unable to predict where dumbbells may reorient and what their final state will be. That is, elasticity theory cannot determine when a given structure is stable, only what its energy is if one assumes that it is stable. Atomistics is needed to obtain this crucial information.

2.4.3 <1 0 0> Dumbbell

The [1 0 0] dumbbell has the highest formation energy of the three primary dumbbells in the bulk and is generally not stable for any significant time. So, perhaps it is not surprising that this dumbbell is also unstable near a dislocation core. A complex landscape of energetics is revealed in Figure 15. As can be seen in Figure 16, this is due to the fact that all of the dumbbells originally introduced in the [1 0 0] orientation transform under minimization. Most become some type of <1 1 0> or <1 $\bar{1}$ 0> structure. Which variant an individual dumbbell transitions to depends on its initial location about the core. Vectors are shown for each lattice site; these run along the resulting dumbbell, and many have partial extent into the page. [1 0 0] dumbbells lying near the [1 0 $\bar{1}$] or [$\bar{1}$ 1 0] directions transition to be one of the indicated types, respectively; these are the lowest energy structures attained. In other areas, dumbbells become variants of <1 1 0>. In the [0 $\bar{1}$ 1] direction, this configuration is not as low energy as a [1 0 $\bar{1}$] shape would be. Presumably, the lowest energy <1 $\bar{1}$ 0> configurations are unattainable under a simple minimization, while a <1 1 0> orientation provides an acceptable local minimum.

Due to symmetry considerations, the patterns of behavior described above will occur for the [0 1 0] and [0 0 1] dumbbell orientations, though rotated by 120°. Just as for the case of the [1 1 1] dumbbell, continuum elasticity would not be able to predict the unstable nature of the [1 0 0] dumbbell.

2.4.4 Vacancy

The results for vacant lattice sites are presented in Figure 17. Perhaps unsurprisingly, negative interaction energies are seen for vacancies in the regions where positive interaction energies are observed for interstitials, and vice versa. That is, where an interstitial is

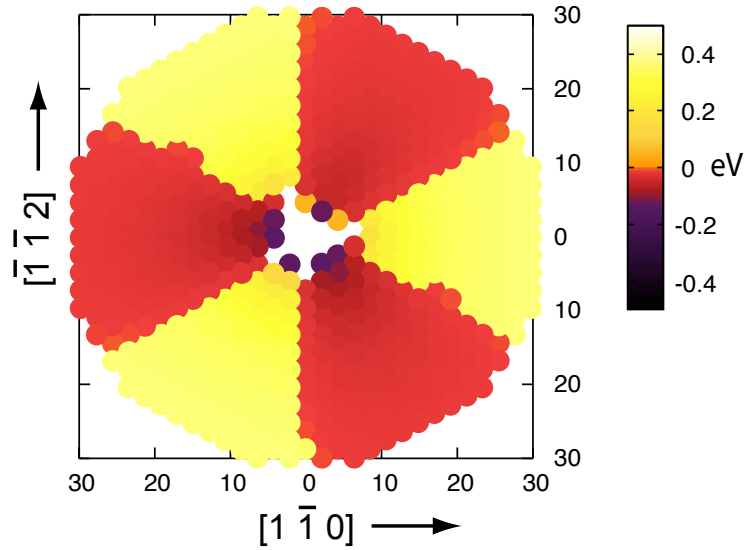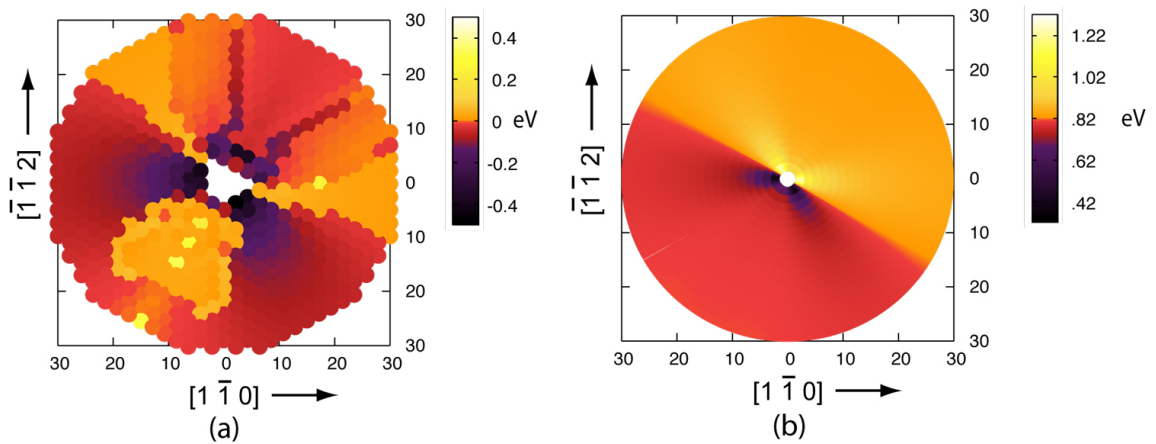**Figure 15:** The interaction energies between [1 0 0] dumbbells and a screw dislocation core are shown as a function of of distance and angle from the dislocation core. The same conventions as in Figure 9 are used. (a) shows the interaction energy calculated by atomistics. It is important to note that the majority of the dumbbells reorient to more energetically favorable configurations during minimization, so these energies do not truly represent the interaction between [1 0 0] dumbbells and the core. (b) shows E calculated by anisotropic continuum theory; in this case the interaction energies are representative of [1 0 0] dumbbells. Note the different scales for the two graphs. Both are referenced for a value of 0 equal to a <1 1 0> dumbbell in the bulk.
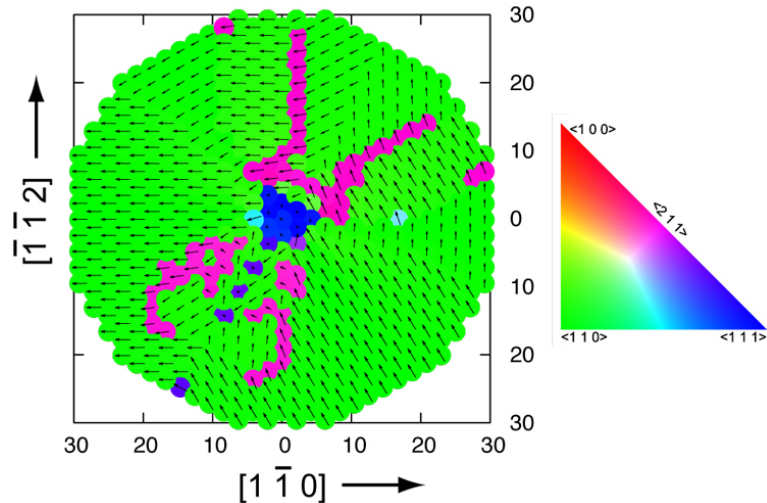
Figure 16: [1 0 0] dumbbells are placed at various angles and positions about the dislocation core and minimized; their final orientations are shown by color. The majority of dumbbells reorient to some variant of a <1 1 0> dumbbell. Vectors on top of each point indicate the direction of the dumbbell (some are partially pointed into the page).
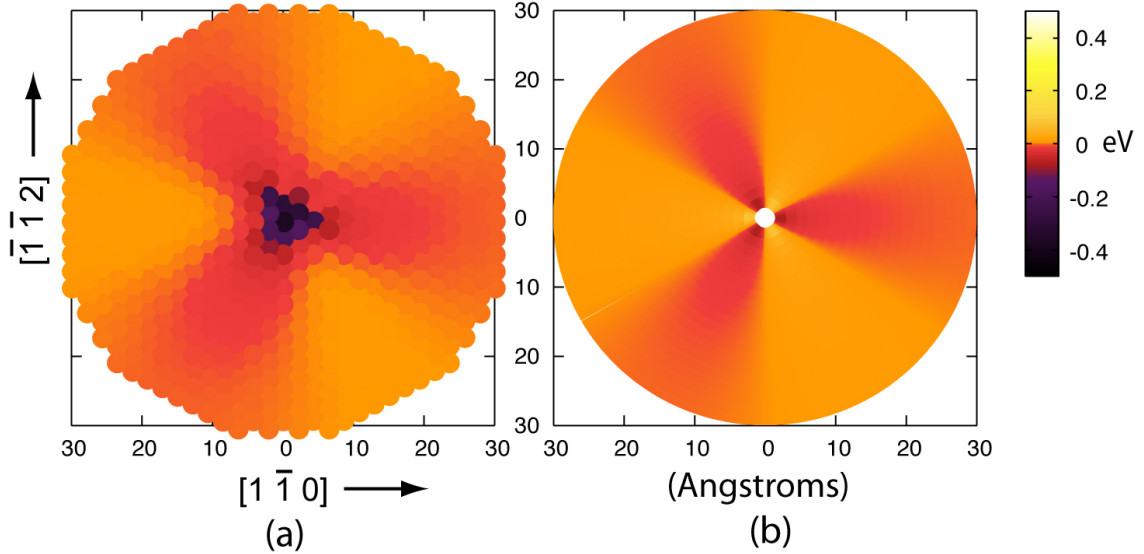
Figure 17: The interaction energies between vacancies and a screw dislocation core are shown as a function of of distance and angle from the dislocation core. The same conventions as in Figure 9 are used. Results from atomistic calculations are shown in (a); anisotropic continuum results are shown in (b). No results are displayed for isotropic elasticity theory; due to the nature of the matrices, this theory predicts no interaction whatsoever.

attracted to the dislocation, the vacancy is repelled, and vice versa. The magnitudes of the interactions for vacancies are significantly less than those for interstitials, however. Positive interaction energies do not exceed 0.003 eV, which indicates that the dislocation core never has a strong repulsive effect on vacancies. Negative interaction energies just outside the core dip to around -0.07 eV; when a vacancy is absorbed by the core the system energy falls by about 0.35 eV. A vacancy has a symmetric dipole tensor which, unlike interstitial dumbbells, results in an isotropic distortion of the lattice around it.

When we compare results from atomistics to those of elasticity theory, agreement is quite good. The sign and magnitude of the interaction energy is similar everywhere except within about 10 Å of the core. Here, atomistics shows a negative interaction energy in all directions, with absorption of the vacancy within about 5 Å of the core. The behavior is qualitatively similar to that observed for the interstitial.

Comparison with isotropic elasticity theory is not shown because the vacancy dipole tensor has only diagonal components and the strain field has only off-diagonal components. As a consequence, no interaction is predicted by Equation 7 at all.

33

2.4.5 Absorption by the Core

Spontaneous absorption of an interstitial defect by the core is observed, regardless of the initial orientation, when the defect is placed within a few angstroms of the core. The radius within which an interstitial will be absorbed is somewhat larger for the less stable defect configurations than for the <1 1 0> types. Absorption of an interstitial results in a crowdion structure along the dislocation line. This crowdion may form along any of several of the columns of atoms nearest the core. These structures are essentially degenerate in energy when compared to the energy of the system before absorption. An example of this is shown in Figure 18. In Figures 12 and 16, the lattice sites which convert to this structure are shown in blue, with <1 1 1> orientation. This absorption by the core generally occurs when the dumbbell is placed within an approximately triangular region about 6 Å from the center of the dislocation; this volume encompasses all the lattice sites in any of 10 [1 1 1] columns parallel to the dislocation. In the case of <1 $\bar{1}$ 0> dumbbells, which are the most stable, absorption occurs only in the 5 columns closest to the core, as shown in Figure 9. This absorbed state is ~2.5 eV below the 0.0 eV reference energy of the interstitial infinitely far from the dislocation; in other words, the system reduces its energy by about 2.5 eV by absorbing an interstitial, or the binding energy of the interstitial to the core is about 2.5 eV.

Similar to the interstitials, a triangular region of low energy configurations exists for the vacancy (see the purple region in Figure 17). Having a vacancy within this region lowers the system energy by about 0.35 eV (the binding energy of a vacancy to the core is about 0.35 eV). However, unlike with absorption of an interstitial, the vacancy keeps its character within the core region. As is shown in Figure 19, the atoms near the vacancy relax around it, but the vacancy essentially remains localized to a lattice site.

2.5 Discussion

Absorption of interstitials in the dislocation core enables kink nucleation and glide, as well as core spreading [33, 117, 118]. These effects are modeled at longer length and time scales with large scale constitutive models, such as in [112], which rely on input from
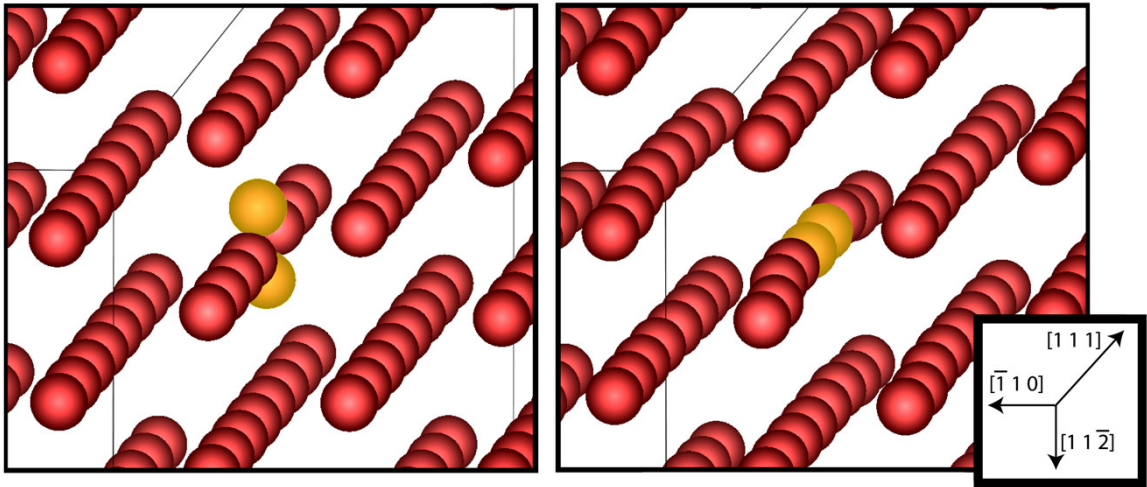
Figure 18: Core structure before (left) and after (right) minimization of a [1 1 0] dumbbell. The dumbbell reorients to become a crowdion along the dislocation line. The two atoms of the dumbbell are highlighted as a visual aid.
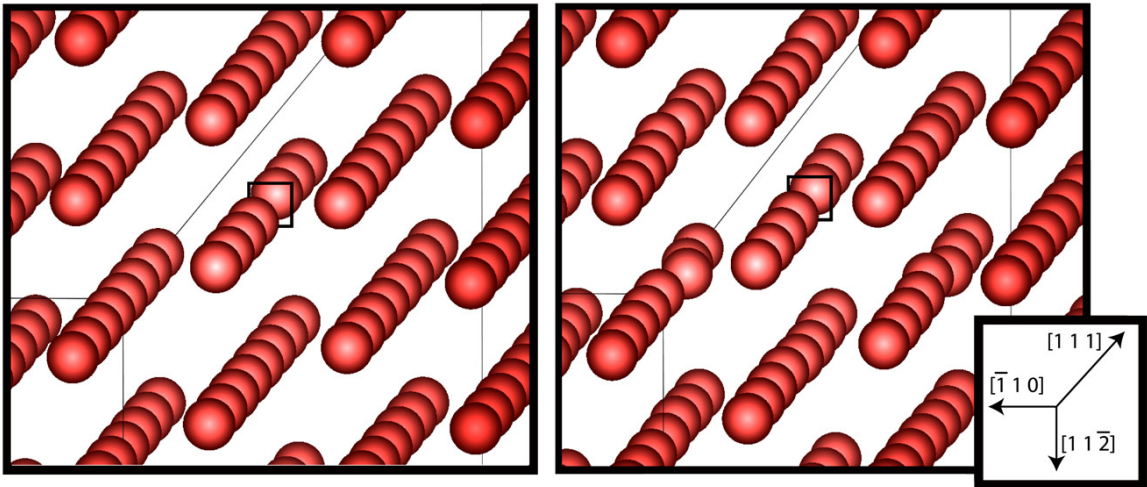
Figure 19: Core structure before (left) and after (right) minimization of a vacancy. The vacancy, marked by an empty box, maintains its character within the core; neighboring atoms relax around it.
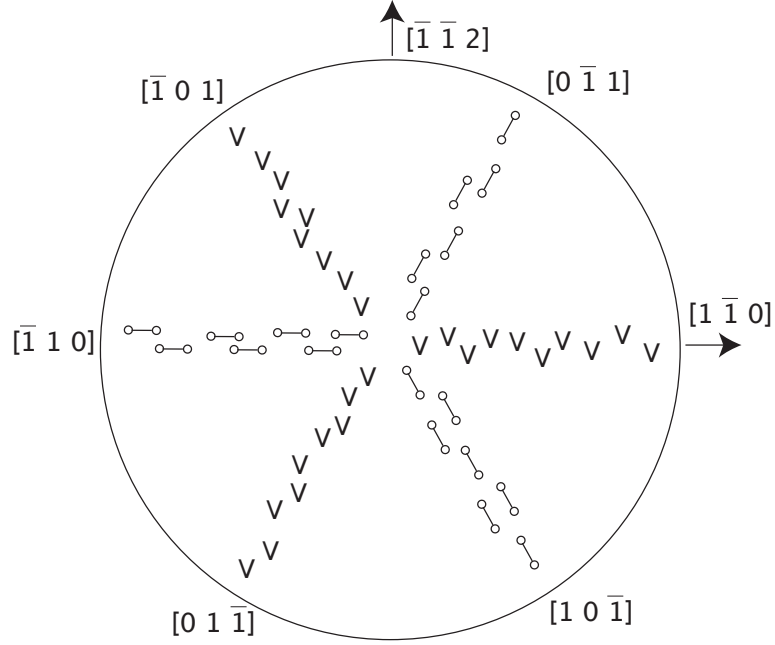
Figure 20: For a right-handed 1/2 [1 1 1] screw dislocation vacancies have the lowest interaction energies along the [1 $\bar{1}$ 0], [$\bar{1}$ 0 1], and [0 1 $\bar{1}$] directions, while interstitials prefer to lie perpendicular to the dislocation line along the [$\bar{1}$ 1 0], [1 0 $\bar{1}$], and [0 $\bar{1}$ 1] directions.

atomistic simulations to govern their dynamics. However, as was previously discussed, many of these codes still rely on isotropic formulations, because of the ease of implementation and generality.

Isotropic continuum theory is shown to be inadequate for describing the interactions between defects and the screw core in Fe based systems, both quantitatively and qualitatively. Anisotropic theory is certainly more promising, with overall good qualitative and improved quantitative agreement with atomistics; however, our results indicate that anisotropic elasticity calculations can not be used solely to describe the interactions between defects and dislocation cores. First, anisotropic calculations alone do not predict which dumbbell structures will be stable near the core. Second, quantitative agreement is not good in this region. These limitations do not preclude the use of anisotropic theory, but indicate that it must be carefully and thoughtfully applied.

In addition to being affected by displacements along the dislocation line, slip may be significantly affected by the atomic displacements perpendicular to the Burgers vector; these may be considered edge components of the displacement[50, 20, 32, 51]. The stresses

on these non-glide components affect the plastic behavior, modifying the critical resolved shear stress needed to move the dislocation. In the isotropic case, there is *no* displacement perpendicular to the dislocation line, only along it. In the anisotropic case, there are edge components of the displacement, however they are not as prominent as they are in the atomic model. This discrepancy is likely to be very important in determining the behavior of the interaction of the dislocation with defects very near the core.

Generically, the regions about the core can be split into those with a preference for vacancies (along the $[1\ \bar{1}\ 0], [\bar{1}\ 0\ 1]$, and $[0\ 1\ \bar{1}]$ directions) and those with a preference for interstitials (along the $[\bar{1}\ 1\ 0], [1\ 0\ \bar{1}]$, and $[0\ \bar{1}\ 1]$ directions), as shown in Figure 20. This segregation may reduce the overall recombination of defects in the vicinity of the dislocation, until absorption within the core itself. The determination of what orientation of interstitial dumbbell is preferred for a given lattice site is a problem for which atomistics provides some insight. Members of the $<1\ \bar{1}\ 0>$ family have the most strongly negative interaction energies, but only in the regions where having an interstitial is preferred over a vacancy. Here, a dumbbell pointed towards the core with no extent along the dislocation line is the lowest energy configuration. In the regions where $<1\ 1\ 0>$ dumbbells show positive interactions energies with the core, members of the $<1\ 1\ 0>^{+}$ family are more likely than those from $<1\ \bar{1}\ 0>$; both have positive interaction energies, but the former is less strongly repelled. $[1\ 1\ 1]$ dumbbells may also survive in these regions, although they are slightly higher in energy. The $[1\ 0\ 0]$ configuration is too unstable to exist near the core; it will typically reorient to a $<1\ 1\ 0>$ structure. Continuum theory does reveal the proper hierarchy of energetics, but does not show conclusively which orientations will be stable near the core, nor what shape an unstable dumbbell will reorient to under the core's influence. Knowing these details is critical for determining, for example, defect absorption rates into the dislocation core.

Near the core, continuum theory is completely unable to describe interactions, due to the $1/r$ terms in the strain fields, consistent with previous work. Additionally, atomistics shows a negative interaction energy close to the core (within approximately 10 Å) for all defects in all direction, indicating the eventual absorption of the defect into the core. The core shows

itself in atomistic simulations as a triangular region about the center of the dislocation with a radius of ~6 Å. Continuum theory often shows positive interaction energies along particular directions, neglecting this important core effect. Far from the core, qualitative agreement is good for the <1 1 0> dumbbells and the vacancies, where stability is not an issue (that is, there are minima in the potential energy landscape near all the initial positions of the defects). However, quantitative agreement is lacking. This issue could be improved with more advanced techniques for calculating the dipole tensor, such as including higher order terms beyond the first order. In any case, while anisotropic elastic theory does predict qualitative behavior far reasonably well, and could be used to form the basis of a higher level model of defect-dislocation interaction, the differences between elasticity and explicit atomistics are great enough that results should always be validated against atomistic calculations.

CHAPTER III

HYDROGEN BUBBLES

3.1 Motivation and Literature Review

Understanding the mechanisms behind phenomena such as embrittlement, hardening, creep, and swelling requires a fundamental understanding of how these gases interact with defects in the microstructure. While it seems clear that hydrogen and helium do play an important role, there are many open questions on how exactly the gases assist in these processes [107, 24, 96].

There is a large body of work on the role of hydrogen with steels. Many have documented the deleterious effects of hydrogen [107, 58, 18], but the processes responsible for the effects remain open for debate. In irradiated environments such as fission and fusion reactors and accelerator-driven systems, hydrogen may be present due to adsorption, implantation, or transmutation [45]. Hydrogen has a fairly low solubility in alpha-iron and a rapid diffusion rate; thus it can be difficult to study experimentally, especially at atomistic scales. Once in the bulk, hydrogen diffuses quickly between tetrahedral interstitial sites until reaching a surface or a trap, such as a vacancy or grain boundary [106]. Computational atomistic studies provide a chance to study the details of this process on a scale not possible with experiment [87, 72]. There have been a large number of ab initio and atomistic scale studies performed on the iron-hydrogen system. These include studies on the diffusion of hydrogen through bulk iron [120, 66, 139], the trapping of hydrogen at monovacancies [62, 115], and the accumulation of hydrogen at crack tips [131] and dislocations [68, 114, 137].

Hydrogen embrittlement (HE) is a particularly important issue with many different theories about the cause behind it. Deformed, strained, and irradiated systems are particularly susceptible. There have been multiple theories proposed on what causes HE in metals [108, 109, 10, 147]. Hydrogen–enhanced localized plasticity (HELP) [10] theory predicts that hydrogen makes dislocations more mobile, leading to increased deformation in specific

areas, and ultimately plastic failure. Hydrogen may also cluster at crack tips, eventually leading to decohesion [108].

However, there is recent evidence that vacancy assisted mechanisms may play the most important role in HE [140, 101, 63]. The excessive numbers of vacancies generated by irradiation may be stabilized internally by hydrogen, allowing for the growth of small individual vacancies into large voids. The resulting increase in plasticity leads to failure of the steel [101, 102]. A thorough understanding of the thermodynamics of vacancy-hydrogen clusters is essential to determining the role that hydrogen bubbles may play in the extremely complex picture of hydrogen embrittlement.

Experimental results from ion beam implantation and detrapping studies provide a basis for comparison and verification of atomistic studies. Ion-beam experiments by Myers et al. [98] investigated defect trapping of deuterium in iron. Using ion-channeling analysis, the locations of hydrogen atoms near defects can be deduced when measurements are taken along at least two axes. Deuterium atoms were implanted in an bcc iron single crystal and the crystal was annealed to allow the D to move to traps. Analysis showed that a D trapped at a monovacancy resides in a positions offset by $\delta = 0.4$ Å from an octahedral interstitial site (O-site) in the direction of the vacancy. The authors reported that their results allow for alternate interpretations involving multiple lattice positions for D, but did not feel that this more complex explanation was necessary. Two detrapping stages were identified at 260 K and 350-450 K when the temperature of the samples was ramped up, with binding energies of 0.48 and 0.81 eV, respectively. The first release was associated with D trapped at monovacancies, while the higher temperature release was speculated to correspond to vacancy clusters or dislocation trapping. Effective medium theory (EMT) was proposed to explain these experimental results [104, 103].

Later work by Myers et al. [97] identified three types of defect traps, with energies of 0.53, 0.71, and 0.78 eV, when iron was implanted with both D and He. The first type was assumed to be due to monovacancies, the second type due to vacancy clusters, and the third type is due to trapping at He bubbles. Further work was performed by Besenbacher et al. [8]. When the fluence was increased compared to the above mentioned experiment, an

additional release stage developed at 220 K. The authors deduced that this stage was due to multiple occupancy of a vacancy by up to six D atoms. When accounting for vacancy mobility, it was found that 1-2 D are trapped by a vacancy with strength of 0.63 eV, while 3-6 D are trapped by 0.43 eV. A review of many of these results, as well as additional results for surface interactions and a transport formalism for hydrogen behavior, are described in a review paper by Myers et al. [99]. Results from effective-medium theory (EMT) [104, 103] reasonably well to these experimental results, with 1-2 D trapping of about 0.8 eV, 3-4 D trapping around 0.52 eV, and 5-6 D trapping around 0.41 eV. These numbers were generated by assuming that all D occupied an offset O-site, with symmetric minimization allowed in the direction of the nearest (1 0 0) planes.

One of the most crucial pieces of information that must be known about hydrogen-vacancy systems if complex studies are to be performed is the basic energetic information. Additional experimental results and most recent density functional theory calculations seek to answer this question by determining how many hydrogen atoms may be bound to a monovacancy. A hydrogen atom can be considered to be exothermically bound to a vacancy its binding energy exceeds the heat of solution. The heat of solution of hydrogen in iron is quoted as slightly different values from different sources, including 0.25 eV/atom [40], 0.29 eV [81] and 0.32 eV/atom [141] from experiment and calculation. Since experiment showed that up to six hydrogen atoms are trapped by 0.43 eV, larger than any of the found heats of solution, it was generally agreed upon in the literature that all six offset O-sites around a monovacancy are exothermic [63, 40], and the H_6V complex will be dominant over the H_2V complex in the bulk.

Tateyama and Ohno [141] performed density functional theory (DFT) calculations that disagreed with this view. In a 54 atom supercell, up to six hydrogen atoms were placed in offset O-sites. The first two hydrogens were bound by $\sim$0.60 eV, in good agreement with the value of 0.63 eV from experiment. For 3-5 hydrogen atoms, trapping energies ranged between about 0.4 and 0.3 eV, also showing agreement with the experimental 0.43 eV. The sixth hydrogen atom showed a slightly negative binding energy, indicating that it would not be trapped. Compared to the hydrogen heat of solution, which the authors calculated

to be 0.32 eV, only 1-3 hydrogen atoms were exothermic, with the third just barely so. The authors concluded that the H_2V state is actually dominant, not the conventionally accepted H_6V state. Based on these results, the authors investigate the shapes of H_2V clusters, finding that anisotropic clusters with linear and tabular shapes will be generated.

While there exist many studies on hydrogen bubbles, a fundamental understanding of themechanisms behind their effects is still largely lacking. Using empirical potentials with molecular dynamics techniques, we are able to model much larger systems than are currently possible with first principles techniques, while retaining the detail of modelling individual atoms. In this chapter, we simulate clusters of hydrogen and vacancies within alpha-iron to determine their energetic properties.

3.2 Methods

Our goal is to simulate hydrogen-vacancy clusters and calculate their minimum energy configurations. Clusters consisting of m hydrogen atoms and n vacancies (H_mV_n) are created in bcc iron. Unless otherwise mentioned, a simulation cell of size $15a_0 \times 15a_0 \times 15a_0$ is employed, where $a_0 = 2.8553$ is the lattice constant of iron. In a perfect cell, there are 6750 Fe atoms. Periodic boundary conditions are used in all dimensions. The LAMMPS Molecular Dynamics Simulator [113] is used for all relaxation steps.

For the interatomic potentials, two variants of an embedded atom method (EAM) potential developed by Ramasubramaniam et al. [119, 121] for iron and hydrogen are used for all calculations. Referred to by the developers as potentials B and B$'$, these potentials both take their Fe-Fe interactions from Ackland et al. [3], while the H-H and Fe-H interactions are fit from density functional theory (DFT) data. Potential B$'$ is fit to bulk and vacancy DFT data, while potential B is additionally fit to surface DFT data. Potential B is recommended over B$'$ by the potentials' authors, however they note that B$'$ performs slightly better under a strain field in a bulk environment. Since our system is essentially a bulk environment lacking surfaces, it was unclear which variant would be more well-suited to the problem of hydrogen-vacancy clusters. We test both potentials and characterize the thermodynamic properties of the resulting cluster configurations by calculating formation energies

and binding energies of vacancies, hydrogen atoms, and self-interstitial atoms (SIAs).

A formation energy is defined as the difference between the total energy of the system of interest and the sum of the energies of the constituent parts when separated. Thus, the formation energy of each $H_m V_n$ bubble is calculated by

$$E_f(H_m V_n) = E_{tot}(H_m V_n) - \left\{ (N-n)E_{coh}^{Fe} + mE_{coh}^{H} \right\} \tag{19}$$

where N is the total number of atoms in the perfect system, the *tot* subscript indicates total system energy and the *coh* subscript indicates cohesive energy. Cohesive energy is calculated for bcc iron at $E_{coh}^{Fe} = -4.013$ eV/atom, and the cohesive energy for hydrogen is taken to be $E_{coh}^{H} = -2.37$ eV/atom [119]. Additionally, formation energies are calculated for <1 1 0> SIAs, giving a value of $E_f^{SIA(110)} = 3.529$ eV, and for hydrogen interstitials occupying the tetrahedral interstitial site, with $E_f^{H} = 0.292$ eV or 0.296 eV for potentials B and B', respectively. E_f^{H} is equivalently termed the heat of solution of hydrogen in iron. In order for the formation energies calculated to be meaningful, it is imperative to use minimum system energies. However, it is non-trivial to find the minimum energy configurations of $(m+n)$-body systems; we use a combination of molecular dynamics and Monte Carlo (MC) algorithms to search for these configurations.

First, the energetics of voids without hydrogen are investigated. A vacancy is introduced into the simulation cell, and the system is minimized using a conjugate gradient algorithm, yielding a single vacancy formation energy E_f^{V} of 1.721 eV. Next, the atom with the highest potential energy is removed from the system, and again the system is minimized. This scheme is iteratively conducted to create voids up to 10 vacancies, and the formation energy of each is calculated. These systems with n vacancies form the initial configurations into which hydrogen atoms are later introduced. In practice, the voids are roughly spherical.

Next, hydrogen atoms are introduced to the systems of n vacancies. For this initial study, each combination of m and n that fit the following conditions is considered: $0 < m < 50$, $1 < n < 10$, and the ratio $(m/n) \leq 10$.

A region of radius 1.3 Å is defined around each of the n vacant lattice sites. m hydrogen atoms are randomly inserted into the volume formed by the union of these regions. The

system is minimized to a local minimum using conjugate gradient in the LAMMPS MD Simulator. Then, the system is quenched to 0 K by scaling down the velocity components of each atom. The total system energy is measured and recorded. At this point, a Metropolis Monte Carlo scheme [85] is used, in combination with minimizations through molecular dynamics, to aid in finding lower energy configurations. Every hydrogen in the system is randomly displaced from its site by a maximum of r_{max} Å in each of the x, y, and z directions. The system, including both the iron and hydrogen atoms, is again minimized at 300 K with the LAMMPS MD Simulator to come to a new local minimum, then quenched to 0 K. If the total system energy is lower than in the previous state ($\Delta E < 0$), the transition is accepted, and the newly found configuration is used as the basis for the next iteration. If $\Delta E > 0$, the transition is accepted with probability $p = \exp(-\Delta E/kT)$, where k is Boltzmann's constant and T is absolute temperature. Accepting some transitions that raise the system energy allows the cluster to avoid getting stuck in local minima. Iterations are repeated until the stopping criterion, discussed below, is met. An iteration consists of three steps: moving the hydrogen atoms within the cluster, minimizing the entire system using MD methods, and comparing the energy to previously seen states and accepting or rejecting the new state with MC criterion. A schematic of this iterative process is shown in Figure 21.

The systems tend to find lower energy states infrequently, but with relatively large decreases in energy, instead of finding slightly lower energy states on nearly every step. Thus, we use a stopping criterion based on number of iterations, instead of stopping when the change in energy is below some set value. Each bubble simulation is continued for a minimum of 1000 steps, and the total number of steps is adaptively increased for each case so that the simulation runs for at least q steps without finding a new lowest energy state.

Additionally, a subset of clusters ($H_m V_1$, $1 \leq n \leq 6$) are replicated in a smaller $3a_0 \times 3a_0 \times 3a_0$ simulation cell, using *only* potential B. Density functional theory (DFT) is also used to study the energetics of this subset of configurations. In these calculations, performed by Benjamin Beeler, the lowest energy configuration for each $H_m V$ system is

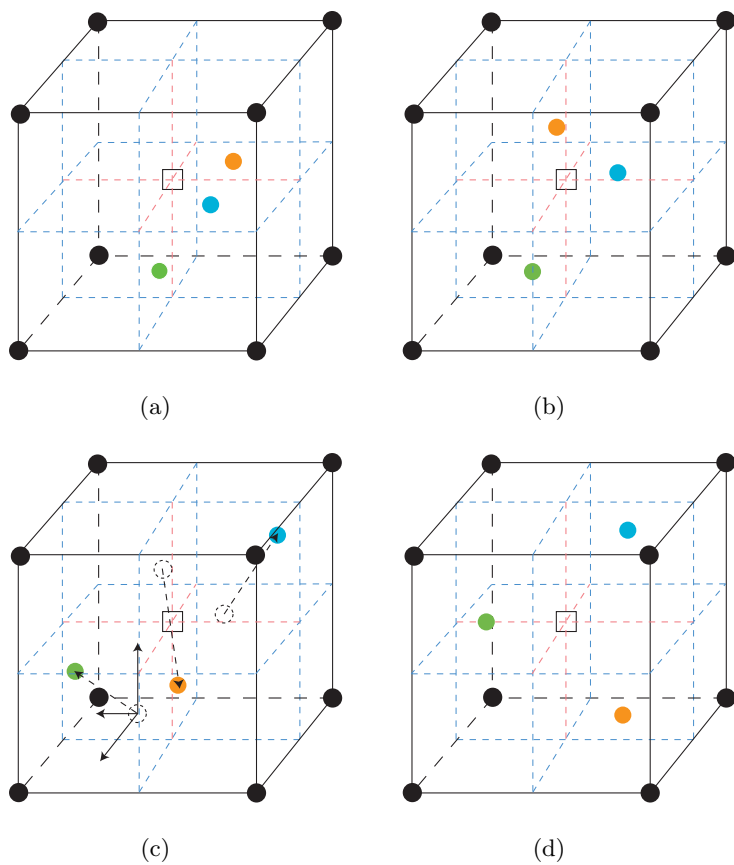**Figure 21:** The Monte Carlo process is depicted schematically for the H_3V_1 cluster. First, atoms are randomly inserted (a), then minimized (b). The atoms are displaced randomly in the x, y, and z directions (c) and minimized multiple times. Finally, the low energy configuration is found (d). Hydrogen atoms are shown colored, the vacancy is shown as a square in the center of a bcc iron cell.

placed into a 54 atom supercell and analyzed with the Vienna *ab initio* Simulation Package (VASP) [71, 67, 11]. The Projector Augmented Wave (PAW) method [65] is utilized within the density functional theory [61, 70] framework. Calculations are performed using the Perdew-Burke-Ernzerhof (PBE) [14] Generalized Gradient Approximation density functional implementation for the description of the exchange-correlation. Methfessel and Paxton's smearing method [84] of the first order is used with a width of 0.2 eV to determine the partial occupancies for each wave function. Relaxations are performed using the conjugate gradient method with a convergence criterion on the forces of 0.02 eV/Å. An iron PAW pseudopotential with the $3d^74s^1$ valence electronic configuration and a core represented by [Ar] along with a hydrogen PAW pseudopotential with a $1s^1$ valence electronic configuration is utilized. A cell was analyzed removing symmetry restrictions with a 4x4x4 gamma-centered k-point mesh, resulting in 36 irreducible k-points in the Brillouin zone. To make the calculations more accurate, the energy cutoff was increased to 500 eV.

3.3   Results

3.3.1   Performance of Interatomic Potentials

It is desirable to find the ground state, or lowest energy, configuration of hydrogen atoms with a void of a given size in order to accurately calculate its energetics. Since the formation and binding energies are on the order of 1-10 eV, configurations with higher energies will cause scatter in the data. Optimizing the iterative scheme to search out very low energy configurations with a reasonable amount of computational resources is needed.

The three parameters that control the speed and accuracy of the scheme are r_{max}, q, and T. r_{max} controls the maximum distance in each of the x, y, and z directions that hydrogen atoms are displaced each iteration, q determines the number of iterations that will be run, and T gives the temperature that is considered when accepting or rejecting transitions.

To find the optimal values for each of these parameters for each potential, a test system with $m = 18$ and $n = 3$ is considered for its relatively small size but high cluster density [54]. The two potentials vary considerably in their performance. For each parameter variant, two trials were run, resulting in a total of 34 trials for each potential. When the same energy

is recovered multiple times, we may be fairly certain that this is the lowest energy state of the system. This is the case for potential B$'$, where 29/34 of the trials found the same lowest energy configuration. However, energies varied tremendously for potential B. The lowest energy that was recovered was seen in only one case, with the average system energy over all trials being 0.25 eV higher than the minimum. This difference is significant in the calculation of bubble formation and binding energies, which are on the order of 1 eV.

Values of r_{max} between 0.4 and 1.2 Å in increments of 0.1 Å were tested. Values between 0.7 and 1.0 were found to be suitable. Smaller values do not allow for a thorough search of the potential energy surface (PES), and the hydrogen atoms fall back into their previous positions under minimization. Larger values may cause hydrogen to be artificially removed from the bubble or may cause too much randomness, cancelling out the benefits of using MC. For both potentials, increasing r_{max} results in increased time per iteration. One value of r_{max} must be used for final calculations over all possible combinations of m and n, since the calculated binding energies for a H_mV_n bubble depend on the formation and system energies of bubbles possessing $m \pm 1$ and $n \pm 1$ atoms. A value of $r_{max} = 1.0$ Å, nearly equal to twice the Bohr radius, was selected such that approximately 1/10 of the proposed transitions that raise the energy will be accepted. This accounts for thermal motion over a wide variety of combinations of m and n.

Changing the value of T used for the Monte Carlo step affects the number of energy raising configurations that will be accepted. For the same reasons as were described for r_{max}, very low or high values are inappropriate. We tested $T = 200$, 250, 300, 350, 400, 450, and 1000 K, and found that values between 300 and 450 gave good results. $T = 300$ was used for the results presented in this paper.

The value of q determines how many iterations will be run before the system settles on a final energy; values of 500, 1000, 1500, and 2000 were tested. Increasing q significantly increases computational time, with each iteration taking approximately 1 minute on one processor. For potential B, trials with values of q greater than 500 were more likely to result in lower final energies. However, in all cases the number of iterations between lowest energy states was less than 1000, so $q = 1000$ was chosen for all runs using potential B. $q = 500$
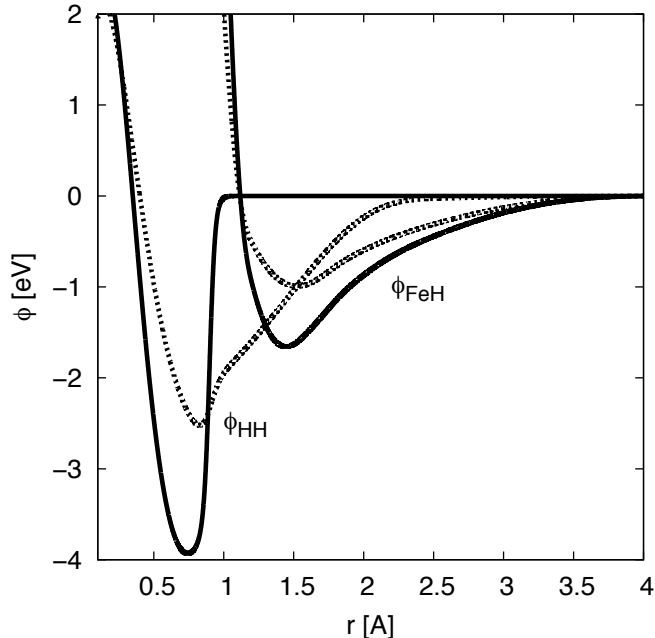
Figure 22: The pair potential part of the EAM potential is shown for Fe-H and H-H interactions. Solid lines indicate potential B, dotted lines indicate potential B′. ϕ_{FeFe} is identical for both potentials.

was found to be sufficient to minimize systems using potential B′.

A smaller battery of tests were also run on the lower ratio $H_{24}V_8$ system to confirm the results. Results were consistent with those described above.

The potential energy surfaces generated by potentials B and B′ are very different and so result in different minimization characteristics. Both potentials are of the EAM type, with contributions to the total energy coming from pair potential and electron embedding functions. The pair potential functions for the H-H and Fe-H interactions for both potentials can be seen in Figure 22. Due to the deep, short-ranged H-H interaction of potential B, the PES is complex, pitted, and difficult to fully explore in a reasonable amount of time. The gradual cutoff of the H-H interaction with potential B′ results in a much smoother PES. Overall, potential B′ is much quicker and easier to minimize with confidence than potential B.
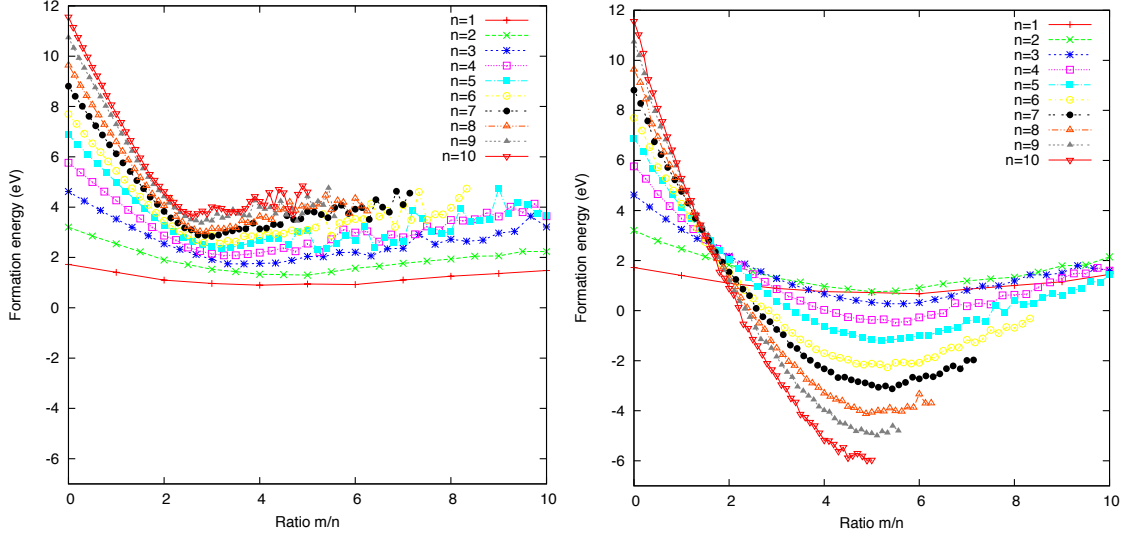
Figure 23: Formation energy curves for clusters of m hydrogen atoms and n vacancies. Results for potential B are on the left and potential B′ on the right. Ratio m/n is shown on the abscissa, formation energy on the ordinate, while curves indicate different values of n.

3.3.2 Energetics

The formation energy, calculated using Equation 19, for each configuration can be seen in Figure 23. Important theoretical differences between the two potential variants become apparent when comparing these two graphs. For potential B, the formation energy of a bubble increases as n increases and is never negative. The minimum formation energy for a particular value of n shifts from occurring at $m/n = 5$ for $n = 1$ to $m/n = 2.6$ for $n = 10$. In contrast, the formation energy of a bubble calculated with B′ decreases as n increases, becoming more strongly negative as the void grows in size. The minimum formation energy for a given n always occurs at $m/n = 5$. The trend seen with potential B′ suggests that it is energetically favorable for hydrogen to be inside a bubble within bulk iron instead of taking molecular form outside of the bulk. However, iron is not observed to absorb large quantities of hydrogen; in fact, the opposite is true - hydrogen has a very low solubility in iron. The trend shown by potential B is more physically believable. It is energetically preferable for hydrogen to be outside of iron than trapped in a void, but the formation energy of the cluster is low enough that a hydrogen-vacancy cluster may form and survive in the right conditions.

The jaggedness seen in the formation energy curves is a product of two effects. First, our method is non-exhaustive in searching for low energy configurations unless an infinite amount of time is allowed for the search, and the global minimum may not be found for every cluster. This is occasionally the case for high n or m/n clusters. Second, when the ratio is too high to support further hydrogen binding, a cluster may eject some hydrogen atoms out of the bubble proper, effectively resulting in a bubble with a lower ratio. This appears as scatter in the data, but is actually an important indicator of how much hydrogen a bubble may support. Potential B suffers compared to potential B' in both these regards, due to the potential shape and characteristics.

The energetics of a cluster of given composition were characterized by the binding energies of a vacancy, a hydrogen atom, and an SIA to that cluster. The following equations were used for the calculations:

$$E_B(V) = E_f(\text{H}_m\text{V}_{n-1}) + E_f^V - E_f(\text{H}_m\text{V}_n) \tag{20}$$

$$E_B(H) = E_f(\text{H}_{m-1}\text{V}_n) + E_f^H - E_f(\text{H}_m\text{V}_n) \tag{21}$$

$$E_B(SIA) = E_f(\text{H}_m\text{V}_{n+1}) + E_f^{SIA} - E_f(\text{H}_m\text{V}_n). \tag{22}$$

These equations are similar to those used by Morishita et al. [92] in their work on the thermal stability of helium-vacancy clusters in iron. Like for their bubbles, we find that the trends in binding energies can be most easily described as functions of the ratio of m to n.

As can be seen in Figure 24, the presence of hydrogen strongly affects the binding of vacancies to voids. Both potentials show that the binding energy of a vacancy to a cluster increases as the hydrogen inventory increases, indicating that hydrogen has a stabilizing effect on a bubble. With potential B, the data become scattered as the ratio approaches 4, while the data for potential B' does not show scatter until a ratio of near 7. This is an indication of the highest ratio that is supported by each potential. Bubbles with ratios higher than 4 and 7 for potentials B and B', respectively, have emitted hydrogen atoms from the cluster core, giving them effectively lower ratios and throwing off the binding energy calculations. For both potentials, the 'even' clusters with $n = 6$, 8, and 10 vacancies have the higher values of $E_B(V)$ than do the 'odd' clusters of $n = 5$, 7, and 9 vacancies. The

50

Figure 24: Binding energy of a vacancy to the cluster for potentials B (left) and B′ (right). Ratio m/n is shown on the abscissa, binding energy on the ordinate, while curves indicate different values of n. As hydrogen inventory increases, so does the binding of vacancies.

odd voids lack the symmetry of the even voids, making them less tightly bound, whether or not hydrogen is present.

The opposite trend is observed in the binding of iron atoms neighboring the cluster (Figure 25). These neighbors may be emitted as self-interstitials into the bulk if not tightly bound, effectively increasing the size of the bubble (i.e. loop punching or Frenkel pair production). Fe atoms are more easily removed from their lattice sites as the density of hydrogen is increased, leading to an effective increase in bubble size. This is another indication of hydrogen's stabilizing effect on vacancy clusters. With potential B, we observe a slow decrease in binding energy from ratio 0 to 2, then a more dramatic increase until scattering begins at around $m/n = 4$. Potential B′ displays a gradual decrease in SIA binding energies until leveling off and beginning to scatter as the ratio approaches 7 and bubbles eject hydrogen atoms to maintain low ratios. Again, we observe some splitting in the curves due to evenness or oddness of the void.

Finally, Figure 26 shows the binding energy of a hydrogen atom to the cluster vs the ratio of hydrogen atoms to vacancies. Like with SIAs, this number decreases as ratio increases. A hydrogen atom can be considered to be unbound from the bubble if its binding energy is less than the heat of solution (0.29 eV). Each curve crosses this line at approximately
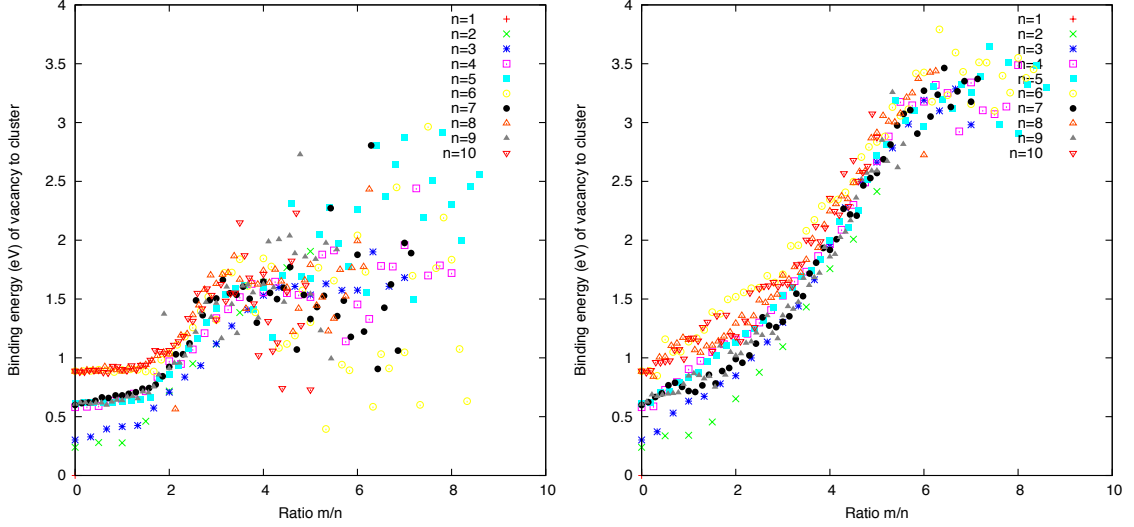
Figure 25: Binding energy of a neighboring iron atom to the cluster for potentials B (left) and B′ (right). Ratio m/n is shown on the abscissa, binding energy on the ordinate, while curves indicate different values of n. As hydrogen inventory increases, binding of neighboring iron decreases.

where we would expect it to from the discussions of the binding energies of vacancies and SIAs - at around $m/n = 4$ for potential B and $m/n = 7$ for potential B′. Even at lower densities, hydrogen atoms are not strongly bound to the cluster and may easily be removed at working temperatures.

Ion implantation and ion-beam analysis studies on hydrogen trapping in iron [97, 8, 99] provide a basis for comparison with our results. Vacancy traps and a large hydrogen inventory are created by bombarding bulk iron with deuterium and helium at low temperature, then the temperature is ramped up while simultaneously measuring hydrogen inventory. The experiments find trap strengths of 0.63 eV and 0.43 eV for 1-2 and 3-6 hydrogen atoms, respectively, about what are assumed to be monovacancies (plus an additional higher strength trap within helium bubbles). This is consistent with our findings for the binding of hydrogen.

Bubble growth may occur by absorption of vacancies or by the emission of neighboring iron atoms into the bulk. In order for the latter phenomenon of loop punching to occur, the emission of iron atoms from around the bubble must compete effectively with emission of a hydrogen atom. However, at any given ratio, hydrogen atoms are significantly less
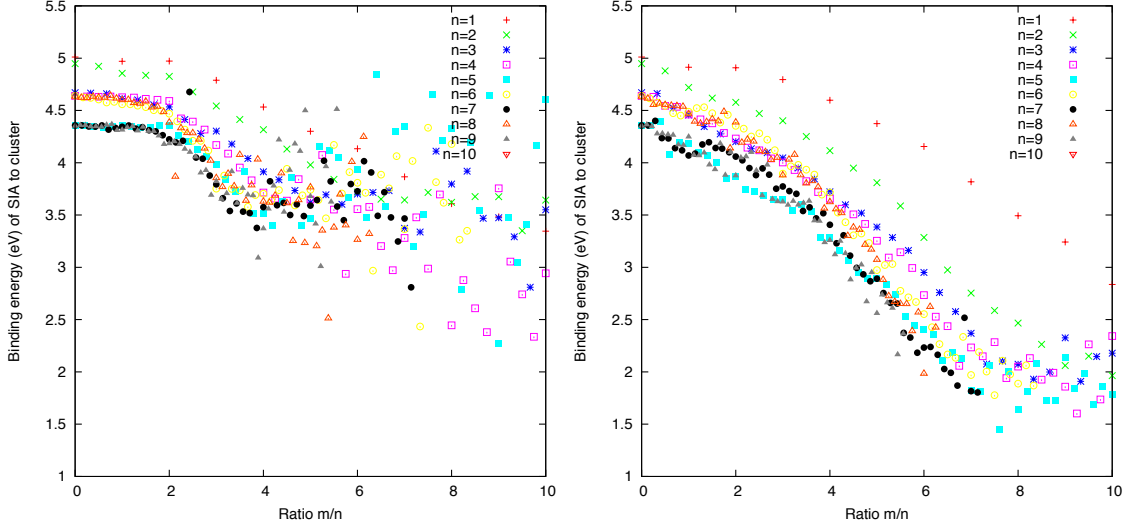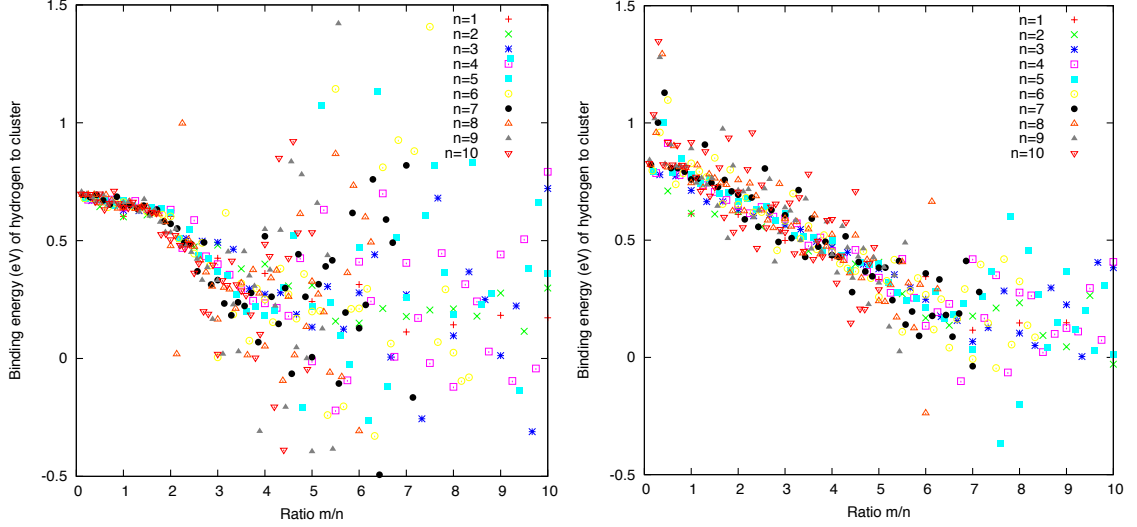
Figure 26: Binding energy of a hydrogen atom to the cluster for potentials B (left) and B′ (right). Ratio m/n is shown on the abscissa, binding energy on the ordinate, while curves indicate different values of n. As hydrogen inventory increases, the binding of hydrogen atoms decreases.

well bound to the cluster than are SIAs, so loop punching would not be expected to occur. Vacancies, which may be present in abundance in an irradiated environment, are a more likely contributor to bubble size.

3.3.3 Multiple Hydrogen Occupancy of Monovacancies

After analysis of the full suite of simulations above, interesting result is discovered for the case of multiple hydrogen atoms surrounding a monovacancy. The trapping of multiple hydrogen atoms at a vacancy in bcc iron is an issue that has been considered by many authors. Experiments [98, 97, 99] have shown that a single hydrogen is trapped by a vacancy in a position slightly offset by $\delta = 0.4$ Å from an octahedral interstitial site (O-site) towards the vacant site. Six of these sites exist in the bcc structure for each vacancy, and it has been assumed that these sites will be the sites of choice when multiple hydrogen atoms are trapped by a vacancy, with sites being filled in the order shown in Figure 27[1]. The number of these sites that are thermodynamically favorable has been much debated, with experiment and effective-medium theory (EMT) [63, 40] favoring H_6V complexes, and

---

[1]The configurations pictured in Figure 27 depict what will be referred to as the mOct configurations (before relaxation), with m denoting the number of hydrogen atoms in the system.
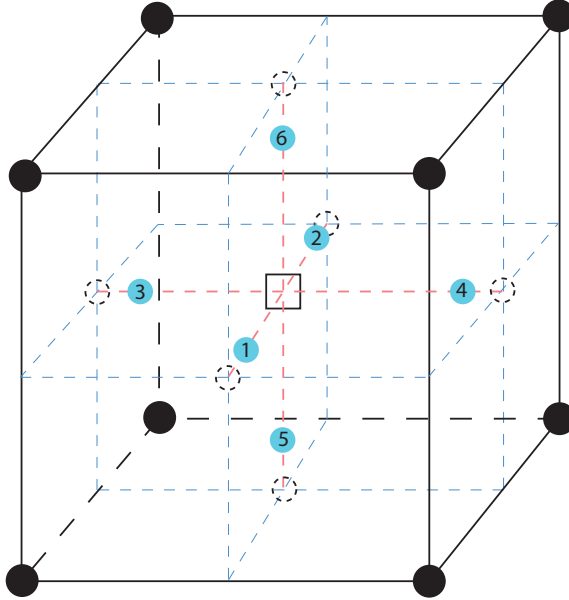
Figure 27: Generally accepted sites for six hydrogen atoms around a monovacancy (the 6Oct configuration) in bcc iron. Iron atoms are shown in black, octahedral sites are shown with dotted circles, vacancy is shown as an empty square. The six hydrogen atoms are blue and offset from octahedral sites by δ; numbers indicate the order in which atoms are added to the system to generate mOct configurations.

recent *ab initio* results showing H_2V complexes to be preferred [141].

However, our research indicates that there are more energetically favorable H_mV configurations than have been studied in the past, and we find new low energy structures for four, five, and six hydrogen atoms about a monovacancy. Although the method described above for locating low energy states of a cluster allows us to reach this conclusion because it makes no initial assumption about the configuration of the hydrogen atoms within a monovacancy, due to the importance of the electrons in calculations involving hydrogen, it cannot be used alone to describe energies accurately. Thus, density functional theory (DFT) calculations are subsequently performed on the low energy configurations obtained by MD/MC methods.

The space of possible configurations for m hydrogen atoms about a monovacancy (H_mV) is first searched using molecular dynamics (MD) and Monte Carlo (MC) methods, as described above. This method allows for a thorough exploration of the potential energy surface

(PES) in a rather short time; however, due to the importance of the electrons in calculations involving hydrogen, it cannot be used alone to describe energies accurately. Thus, density functional theory (DFT) calculations are subsequently performed on the low energy configurations obtained by MD/MC methods.

The six mOct configurations are generated and minimized using the LAMMPS molecular dynamics simulator, using a $3a_0 \times 3a_0 \times 3a_0$ cell with periodic boundary conditions, and Ramasubramaniam et al.'s potential B. As should be expected, we find results equivalent to those originally published by Ramasubramaniam et al. [119]. For one, two, or three hydrogen atoms, the MD/MC method recovers the same configurations that are found when a system starting from the mOct state is minimized. The minimized position for a single hydrogen is offset from the O-site by δ=0.26 Å. When a second hydrogen is added, it occupies the offset O-site opposite from the first hydrogen, as is generally accepted. In this case, δ is lowered to 0.23 Å. When three hydrogen atoms are placed in the positions shown in Figure 27, two of the atoms relax off of the lines between the O-site and the vacancy while continuing to lie on a (1 0 0) plane, forming the configuration shown in Figure 28.

However, the MD/MC method finds new low energy configurations when considering complexes with four, five, or six hydrogen atoms. When the 4Oct configuration is created, all four hydrogen atoms lie on one plane. This is the most symmetric, and perhaps the most intuitive, configuration. After a single 0K minimization, all four hydrogen atoms will remain near plane, close to their initial positions. Two opposing atoms shift to positions slightly above the plane; the other two move slightly below it. However, when the MD/MC method is applied to the H_4V system, the hydrogen atoms are found to form a tetrahedron. This is still closely related to the offset O-sites model; if one of the in-plane hydrogen atoms is moved to either vacant offset O-site, and the system is relaxed, our configuration is recovered. The resulting structure is seen in Figure 29.

With 5 hydrogen atoms, the two configurations are similar. However, the one found with our MD/MC method is a slightly tilted version of the 5Oct configuration, as can be seen in Figure 30. The third, fourth, and fifth hydrogen atoms are shifted away from their offset O-sites towards tetrahedral site (T-sites). The two configurations are nearly equivalent in
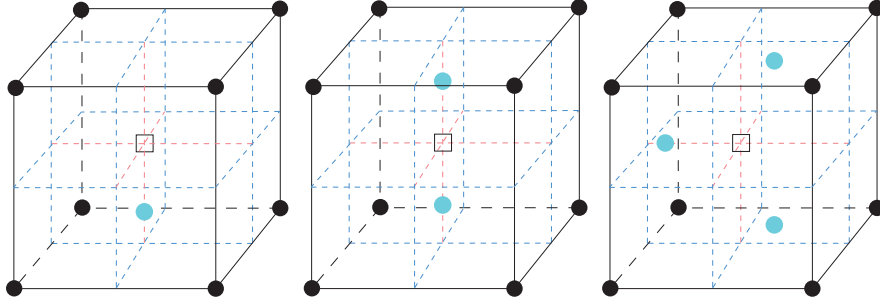
Figure 28: The positions of one, two, and three hydrogen atoms around a monovacancy, found by the MD/MC method. These are the same positions that are found when the corresponding mOct configurations are relaxed. As in Figure 27, iron atoms are shown as black circles, hydrogen atoms are blue, and the vacancy is depicted with an empty square.

Figure 29: The positions of four hydrogen atoms around a monovacancy. 4Oct positions are shown on the left; the lower energy positions from MD/MC are shown on the right. The conventions described in Figure 28 are followed.

energy, but ours is slightly lower.

Minimizing a 6Oct configuration will result in no structural change, other than a slightly varying δ. The MD/MC method gives a different answer. Two opposing H atoms are offset from octahedral positions by only $\delta = 0.052$ Å. The other four atoms lie in a (1 0 0) plane, slightly offset from tetrahedral positions by $\beta \sim 0.12$ Å and equidistant from each other. This is shown in Figure 31, the 2Oct4Tet configuration.

It is important to remember that our minimization and positioning algorithms make no initial guesses about the ideal positions for the hydrogen atoms; instead, hydrogen atoms are randomly inserted into the space around the vacancies and allowed to find the lowest energy positions through Monte Carlo methods. To quantify these results, we compared

Figure 30: The positions of five hydrogen atoms around a monovacancy. 5Oct positions are shown on the left; the lower energy positions from MD/MC are shown on the right. The conventions described in Figure 28 are followed.

Figure 31: The positions of six hydrogen atoms around a monovacancy. 6Oct positions are shown on the left; the lower energy 2Oct4Tet configuration is shown on the right. The conventions described in Figure 28 are followed.

Table 3: Energies (eV) found using molecular dynamics. Note that total energies E_T and formation energies E_f (Equation 19) are lower when $m \geq 4$ for the MD/MC states than for the corresponding mOct configurations.

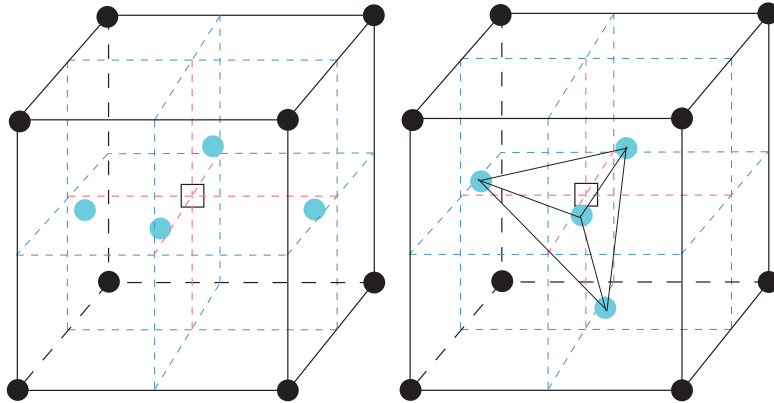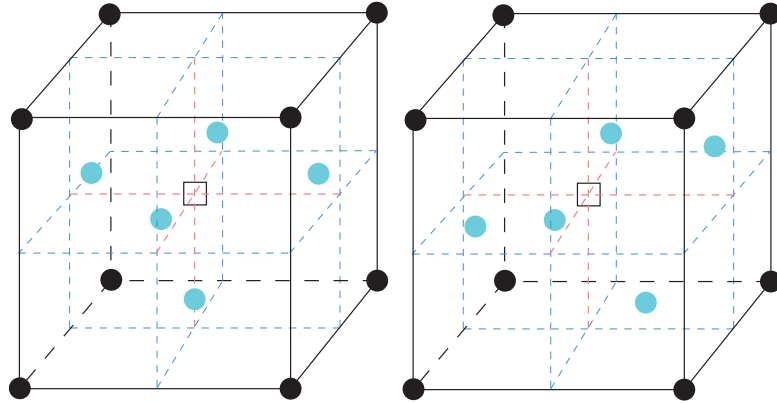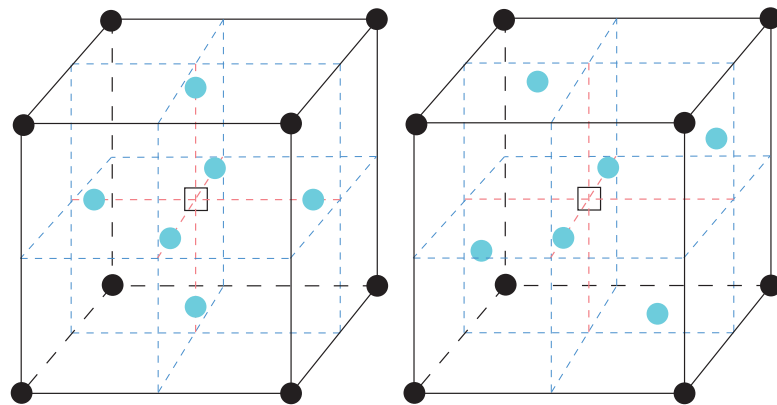| m	mOct Positions			MD/MC Positions		
	E_T	E_f	E_B(H)	E_T	E_f	E_B(H)
1	-213.641	1.417	0.611	-213.641	1.417	0.611
2	-216.323	1.105	0.611	-216.323	1.105	0.611
3	-218.827	0.971	0.432	-218.827	0.971	0.432
4	-221.197	0.971	0.299	-221.255	0.913	0.357
5	-223.511	1.023	0.242	-223.543	0.995	0.217
6	-225.666	1.242	0.084	-225.891	1.018	0.277

the total system, formation, and hydrogen binding energies from our simulations and those from calculations assuming offset O-sites and experiment.

The formation energy of a $H_m V$ complex is calculated as in Equation 19 We calculate the binding energy of the mth hydrogen to the $H_{m-1}V$ cluster with

$$E_B(\text{H}) = [E_T(\text{H}_1\text{V}_0) - E_T(\text{H}_0\text{V}_0)] - [E_T(\text{H}_m\text{V}) - E_T(\text{H}_{m-1}\text{V})]. \qquad (23)$$

Here, $E_T(\text{H}_1\text{V}_0)$ is the energy of a system with a tetrahedral hydrogen interstitial, and $E_T(\text{H}_0\text{V}_0)$ is the total system energy of a perfect block of iron. This formula is mathematically equivalent to Equation 21, however we use this form in order to directly compare with results in the literature without worrying about numerical roundoff errors. Results for E_T, E_f, and $E_B(\text{H})$ for both mOct and MD/MC configurations can be found in Table 3. Energies are equivalent for m =1, 2, 3 since the configurations are identical. Total system energies are lower for our configurations than for mOct configurations when $m \geq 4$; formation energies are also lower.

To confirm our results, we performed *ab initio* calculations as well. We took both the configurations found by MD/MC and the mOct configurations and analyzed their energetics with DFT. We find that our calculations on the mOct states are consistent with what has previously been published [141]. Again, we find that our MD/MC configurations have slightly lower system energies than the mOct configurations in the literature. We compare our results to those available in the literature; namely, Tateyama and Ohno's DFT calculations on mOct configurations [141]. Hydrogen binding energy results can be seen in Table

Table 4: Hydrogen binding energies $E_B(H)$ in eV from previously published DFT calculations, the DFT calculations done for this work, EMT, and experiment.

m	DFT - mOct [141]	DFT - MD/MC	EMT [103]	Experiment [8]
1	0.559	0.584	0.83	0.63
2	0.612	0.607	0.79	0.63
3	0.399	0.384	0.54	0.43
4	0.276	0.343	0.51	0.43
5	0.335	0.297	0.41	0.43
6	-0.019	0.002	0.42	0.43

4.

The mth hydrogen can be considered to be exothermically bound to a monovacancy if its binding energy is greater than the heat of solution of H_2 in iron. The heat of solution of hydrogen in iron from experiment is 0.29 eV/atom [81]. DFT calculations find the heat of solution to be 0.32 eV/atom. Using this value, Tateyama shows that up to three hydrogen atoms are exothermically bound, while the fourth has a binding energy less than the heat of solution. An addition of the fifth hydrogen atom again results in a slight bonding.

In contrast, we show that each additional hydrogen is less well bound than the one before it, instead of predicting a jump in binding energy when adding a hydrogen atom to the H_4V cluster. Binding energies are exothermic for up to four hydrogen sites, when arranged in a tetrahedron shape instead of a plane. For both the 6Oct configuration and 2Oct4Tet, the sixth atom has a binding energy close to zero.

Earlier experimental results from ion beam implantation and hydrogen detrapping studies, demonstrated that there are two release stages of hydrogen from single vacancies, at 0.63 and 0.43 eV [97, 8]. The former is postulated by these practitioners to be related to 1 or 2 H atoms being trapped at a monovacancy, while the latter corresponds to the presence of 3-6 H atoms. Effective medium theory (EMT) was proposed to explain these experimental results, which suggests that all six sites are exothermic for hydrogen occupancy [104, 103].

The binding energies from EMT, however, are significantly higher than the experimental results. Our values, on the other hand, agree rather well with experiment. For one or two hydrogen atoms, we find hydrogen binding energies of 0.584 and 0.607 eV, which match quite well to the second stage of release seen in experiment at 0.63 eV. Our values of 0.384
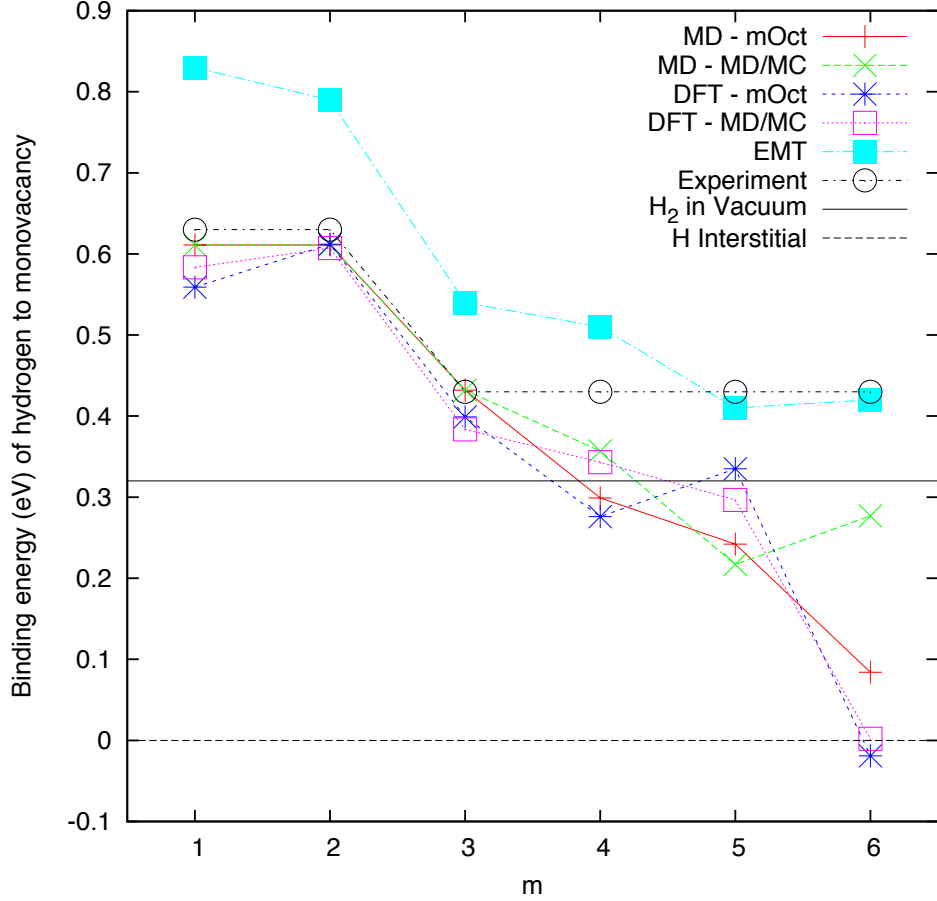
Figure 32: The binding energy of the mth hydrogen atom to a $H_{m-1}V$ cluster. The data points marked with "MD" show data for $E_B(\text{H})$ from Table 3, while those marked "DFT", "EMT", and "Experiment" show the data from Table 4. The energies of a hydrogen atom at an interstitial site and in an H_2 molecule in vacuum (the heat of solution, as calculated by DFT) are pictured as horizontal lines.

and 0.343 eV for the binding of the third and fourth hydrogen atoms are close to the experimentally observed release stage at 0.43 eV. Unlike the EMT results, we do not see binding of the fifth and sixth hydrogen atoms.

3.4 Discussion

The question of whether or not hydrogen gas in bubbles can be adequately modelled with an embedded-atom method potential is a valid one. Hydrogen, as the lightest of elements, has important quantum mechanical properties that are not directly simulated in this study. There will surely be some nuances of interaction that cannot be simulated perfectly without accounting for individual electrons. However, the size limitations of *ab initio* methods make

studying this problem prohibitively computationally expensive at this point in time. The present authors believe that the interatomic potentials we are using adequately reproduce the important interactions that will take place within a hydrogen bubble. The nature of H-H interactions within metals have been studied by various authors. Effective medium theory [105] predicts that hydrogen within a monovacancy will not occupy the center, because of the below optimum value of electron density. Hybridization with the iron occurs, leaving room for multiple hydrogen atoms to occupy the vacancy; however, they will repel each other. This was recently confirmed in *ab initio* calculations [141, 140] which show Fe $3d$-H $1s$ hybridization, in which electron transfer occurs from an iron atom to a hydrogen. Similarly, an H_2 molecule inserted into a vacancy will dissociate, suggesting that hydrogen molecules will not survive in small voids; this effect grows stronger with additional hydrogen occupancy. The interatomic potentials we have used in this study replicate this behavior, having been fit to additional density functional theory calculations. If hydrogen sometimes does exist in a molecular state inside a void, it will dissociate when approaching the iron on the surface. Thus, we can assume that we will capture the most important energetics of a cluster as long as the interactions between hydrogen and iron are properly described.

Although no studies on the specific energetics of hydrogen-vacancy clusters in bcc iron exist in the literature, there are some on helium bubbles [92, 91, 77, 53]. These studies show good agreement with experimental results, which gives us additional confidence that our similar system can be modelled well with these methods. The helium bubbles in iron show the same general trends in binding energy as the hydrogen bubbles we have modelled, with helium tending to stabilize voids. However, the binding of helium to clusters is significantly stronger than the binding of hydrogen; it is comparable to the binding of SIAs. Morishita et al. [91] find that bubbles can support ratios of up to 6 helium atoms per vacancy, at which point SIA-vacancy pairs are created on the edges of bubbles.

Clusters simulated with potential B′ are much more easily minimized to the lowest energy state than those created with potential B. This is due to the more complex nature of the PES generated by potential B. Although the time per iteration is shorter with potential B than potential B′, the increased value of q that is needed cancels this benefit. However,

the interactions described by potential B seem to be more physically relevant than those of B′, based on the formation energy curves seen in Figure 23. In the original paper describing these potentials [119, 121], only data and fitting for potential B is given, so potential B′ needs to be characterized. Our calculations provide data on both potential B and B′'s performance with strongly interacting H clusters which is lacking in the original parameterization.

Binding energy trends are generally consistent between both potential variants. Vacancies become more tightly bound to clusters as the ratio m/n is increased, while both SIAs and hydrogen atoms become more loosely bound. Results from potential B indicate that clusters can support a maximum ratio of ∼4; potential B′ allows for ratios up to ∼7. However, the formation energy curves generated by the two potentials differ, with potential B providing a trend that more closely matches the observed physics. Thus, the former should be taken as a limiting factor for hydrogen ratio in bcc iron.

Based on these basic energetics, bubble growth by vacancy absorption would be a more likely mechanism than loop punching or similar modes. Hydrogen seems to be loosely bound to clusters even at low densities, and the question remains whether it will be bound long enough for stabilizing effects to be realized at temperatures seen in reactor structural materials. However, hydrogen's effect on the binding of self-interstitials may be relevant to the HELP theory of hydrogen embrittlement as well. If interstitials are less well-bound in the presence of hydrogen, dislocation mobility may be increased. Our results for hydrogen binding agree well with experimental ion-beam studies of hydrogen trapping energies, as discussed in the previous section. However, our simulations allow for more precision in calculating energies and allow us to exactly determine the void sizes and bubble ratios involved in creating the traps.

Finally, we have discovered new low energy configurations for four, five, and six hydrogen atoms surrounding a monovacancy in bcc iron and confirmed these results with *ab initio* calculations. All previous calculations and theories assumed that up to 6 hydrogen atoms surrounding a monovacancy would reside in offset O-sites. However, we made no initial assumptions about the positions of the hydrogen atoms, allowing for an unbiased search for the lowest energy configurations.

The question of how many hydrogen atoms can exothermically exist about a monovacancy has been addressed by calculating binding energies of the mth hydrogen to a H_mV cluster. Our simulations agree with previous results [141] that show that the H_6V complex is not the dominant complex in bcc iron, in contrast with earlier experimental and effective medium theory results. However, unlike those previous results, our DFT results show that up to four hydrogen atoms may be exothermically bound to a monovacancy. As more hydrogen atoms are added to a vacancy, each is less well bound than the ones before. This trend is different than when mOct configurations are assumed; in this case, the fourth hydrogen atom is not bound, while the fifth is slightly bound when referenced to the heat of solution. Our low energy configurations provide new insight into the role of vacancy-hydrogen complexes in materials degradation.

The energetics of H_mV_n clusters in bcc iron have been investigated using a combination of molecular dynamics and Monte Carlo techniques, with two different interatomic potentials. The use of empirical potentials allows for larger scale simulations than are currently possible with *ab initio* methods. However, the simulations can still model individual atoms, which gives much more detail than experiment can provide. This detail is essential for the fundamental understanding of how interactions between defects can affect macroscopic properties. Significant differences in the potentials can be seen, but overall trends in binding energies are consistent between both. Hydrogen is seen to have a stabilizing effects on voids, which supports the idea that increased vacancy concentration and clustering may be responsible for hydrogen embrittlement. Although hydrogen is relatively weakly bound to voids, its presence may play a significant role in determining macroscopic properties.

CHAPTER IV

HYDROGEN – HELIUM BUBBLES

4.1 Motivation and Literature Review

Hydrogen and helium are known to have detrimental effects on structural materials, which can be aided by irradiation. This is expected to be a significant problem for future generations of nuclear reactors. This is especially true of fusion reactors [12, 123], in which isotopes of hydrogen provide fuel for the fusion reaction, and helium is created as a transmutation byproduct. There are many theories on what mechanisms are responsible for the deleterious effects of H and He on structural materials [10, 63, 64, 18, 24, 35, 73, 101, 107, 116], ranging from concentration at crack tips to movement along grain boundaries. Whatever the underlying cause, it is well known that either element can contribute to embrittlement and swelling of irradiated materials, with undesirable consequences [102].

In an irradiated system, an above-average concentration of vacancies may assist these processes. Hydrogen and helium diffusing through the material can become trapped at small clusters of vacancies, providing internal stabilization [72]. This results in a decreased likelihood of recombination of self-interstitials with these vacancies, and increased plasticity of the material as a whole. There is a long history of computational study of both hydrogen and helium [145], and in particular, there have been several atomistic scale studies of the energetics of bubbles containing either pure hydrogen [62, 55, 141, 140] or pure helium [92, 38, 77, 53, 133, 43] in α-iron. These studies confirm the idea that the gas stabilizes vacancy clusters, as can be seen in Figures 24 and 25. Vacancies are more tightly bound to the clusters as the inventory of gas increases, while the iron atoms that neighbor the cluster are less tightly bound to their lattice sites and are more likely to be emitted into the bulk as self-interstitials.

While either hydrogen or helium alone may be detrimental, there is evidence to suggest that when both elements are present, synergistic effects occur. It has been shown that

when steel alloys are irradiated with both hydrogen and helium ion beams simultaneously (along with an iron ion beam to induce damage), the swelling of the material and the size of cavities increased significantly compared to samples irradiated with only one of the two elements [152, 138]. Synergistic effects have also been observed in similar studies on other bcc transition metals, such as vanadium [124]. In all these cases, an increased dislocation loop density was also observed under simultaneous irradiation.

Additionally, although the solubility of hydrogen in iron is expected to be quite low by Sievert's law, it has been shown that when helium is also present within the crystal, hydrogen trapping is significantly enhanced even for periods of years after irradiation [142, 45, 44]. It has been theorized that this is due to increased trapping of hydrogen at helium bubbles. This trapping has been observed in metals [7, 97], and attributed to the hydrogen being attracted to the stress field of the pressurized helium bubble [1]. However, there have been no atomistic studies focusing on bubbles containing both hydrogen and helium in iron.

In this work, we present an atomistic study of vacancy clusters containing both pure hydrogen and hydrogen plus helium in bcc iron. We first introduce an interatomic potential suitable for describing the interactions between hydrogen and helium. This potential is used to perform a detailed analysis of the configurations and energetics of a variety of bubbles. We find that the synergistic effects on bubble properties can be explained not through a direct interaction between hydrogen and helium, but through the phenomenon of loop punching. We show that the presence of hydrogen makes loop punching a more energetically favorable event for a bubble with the required amount of helium. In turn, the growth of the bubble results in a larger free surface onto which hydrogen may be bound.

4.2 Methods

We simulate clusters of m hydrogen, j helium, and n vacancies ($H_m He_j V_n$) in bcc iron. In order to extract the energetic properties of these clusters, it is desirable to find the lowest energy configuration of the gas atoms with the voids. We achieve this through iterations of conjugate gradient relaxation and Monte Carlo criteria, using the methods described in Section 3.2 and simply also including j helium atoms in the initial random distribution of

gas atoms.

A suite of interatomic potentials is required to describe all of the interactions between hydrogen, helium, and iron. For the Fe-Fe and Fe-H interactions, we use potential B from Ramasubramaniam et al. [119, 121], which takes the Fe-Fe interactions from the potential of Ackland et al. [3, 83]. For the Fe-He interations, we use the repulsive pair potential of Juslin and Nordlund [69], and for the He-He interactions, Beck's potential is used [6]. For the H-He interactions, we use our own interatomic potential, described in Section 1.2.1.5.

4.3 Results

The idea that bubbles may build up sufficient internal pressure to cause neighboring matrix atoms to be ejected from their lattice sites was proposed many years ago [49], and described in further detail later [35, 146]. This athermal process, known as loop punching, allows for bubble growth even when vacancy absorption is unlikely, perhaps at low temperatures when vacancies are nearly immobile. When neighboring atoms are ejected from their lattice site, Frenkel pairs are created; the vacancy becomes a part of the cluster, while the interstitial may move through the lattice. It is known that helium can build up to high enough pressures within a bubble to cause this occurrence; hydrogen on the other hand, will become unbound from a bubble long before it can induce loop punching. Additionally, experimental studies show an increase in interstitial loops and bubble-loop complexes after irradiation with helium [21].

The process by which bubbles are created progresses in two stages: nucleation and growth. Helium interstitials may cluster together, acting as self-traps [156], or they may become trapped at vacancies. Studies on bubble nucleation show that an initial vacancy is not required for nucleation [90]; instead, the binding between several helium atoms is strong enough to punch out the first interstitial. Additional helium atoms then become trapped at the embryonic bubble, eventually resulting in increased pressure and growth [29].

Although the name "loop punching" is suggestive of the thought that an entire interstitial dislocation loop with a radius equal to that of the bubble would be emitted at once
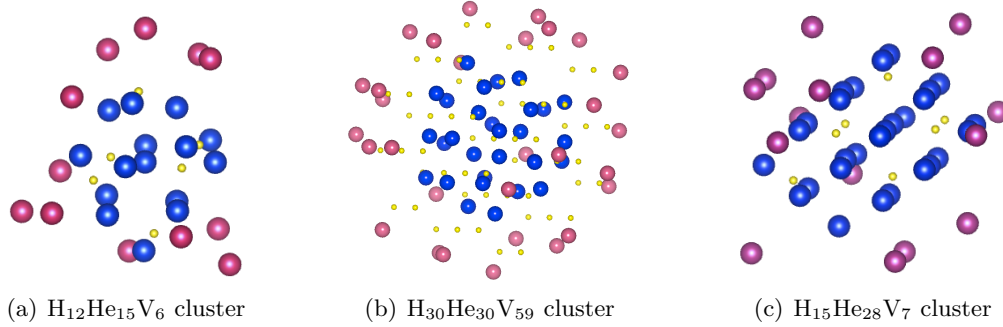
(a) $H_{12}He_{15}V_6$ cluster   (b) $H_{30}He_{30}V_{59}$ cluster   (c) $H_{15}He_{28}V_7$ cluster

Figure 33: The low energy configurations of hydrogen-helium-vacancy clusters are shown. Vacant lattice sites are pictured as small yellow circles, hydrogen atoms are pink, and helium atoms are blue. Surrounding iron atoms are not pictured. The helium atoms form the core of the bubble, with the hydrogen atoms making up the shell. In general, the helium was not well-ordered, but occasionally highly ordered states such as in 33(c) were seen.

[35, 17], some recent simulations show that the loop may be created through a series of emissions of single interstitials over time [42]. These individual interstitials are initially bound to the cluster. Whether full loops or single interstitials are emitted may be a function of the bubble size.

4.3.1   Bubble Structure

In all the simulations performed, the lowest energy configuration of the gas atoms within the bubble took approximately the same form, regardless of the bubble size. The core of the bubble was comprised of helium, surrounded by a shell of hydrogen atoms.

This structure does not seem to result from any particular interaction between hydrogen and helium. If either element is removed, the other maintains essentially the same structure. That is, in a bubble containing only hydrogen, the hydrogen will attach to the free surface, leaving the core empty. Once the surface of the bubble is effectively covered, the remaining hydrogen is emitted into the bulk. In a pure helium bubble, the gas maintains a distance from the iron atoms comprising the surface of the bubble, as found in the simulations of Stewart et al. [133]. Examples of these structures are shown in Figure 33. Additionally, although the helium in a cluster was not generally well ordered, occasionally highly-ordered states were observed as in Figure 33(c).

For the majority of this work, we consider bubbles made up of six vacancies. Since
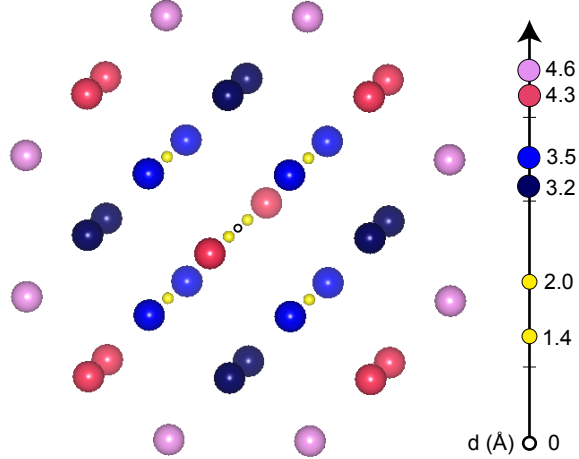
Figure 34: The structure of the *unrelaxed* configuration of a cluster of 6 vacancies. The vacant lattice sites are shown in yellow, and the first four shells of neighboring iron atoms are also shown, sorted by color. The geometric center of the bubble is shown as a small white circle, and the distance d (Angstroms) at which members of each group reside from the center is shown on the right. We use the dark blue atoms, which reside at a distance or ~ 3.2 Å from the geometric center, to define the inner and outer radii of the cluster as described in the text.

our bubble are rather small and may not be considered fully spherical, defining a radius is not straightforward. However, the iron atoms that surround the six vacancies form shells, as can be seen in Figure 34. Before gas atoms are added to the bubble, eight iron atoms reside closest to, and at the same distance from, the geometric center of the bubble in a symmetric configuration. As we add gas atoms to the bubble, the symmetry is broken. Thus, we refer to the inner and outer radii as the distances between the geometrical center of the bubble and the iron atoms of this first shell that are closest to and farthest from that point, respectively.

Figures 35 and 36 show profiles of where different elements are located within the clusters. Both the inner and outer radii are shown, as well as a profile of where the hydrogen is located. As can be seen from the red curves in Figure 35, hydrogen has little ability to enlarge the radius of a bubble. As hydrogen inventory is increased, only a very slight increase in the radius is observed. At $m = 20$, a sharp decrease in inner radius is seen, while the outer radius stays roughly constant. The hydrogen profile explains this behavior. When $m < 19$, all of the hydrogen well is within the inner radius. At $m > 19$, at least one
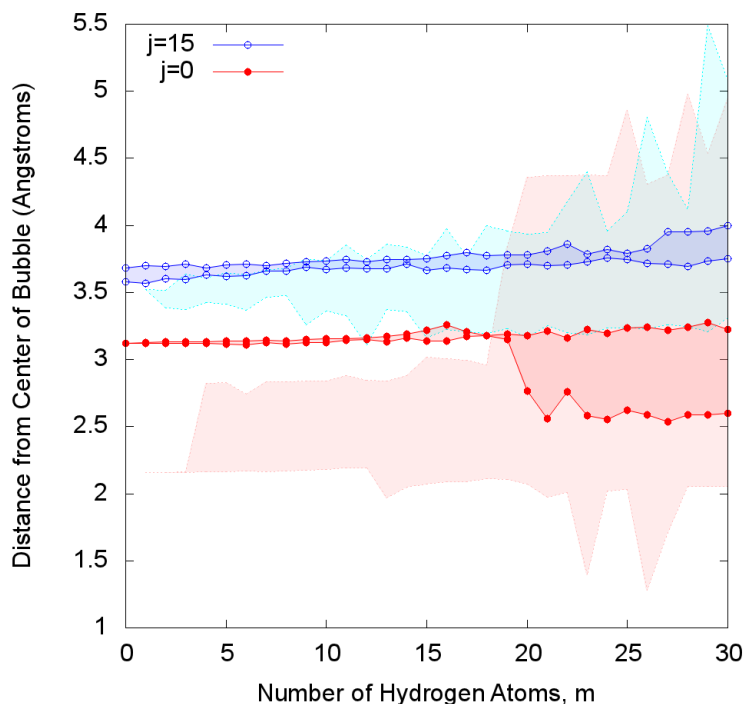
Figure 35: The radii in Angstroms of a $H_mHe_jV_6$ cluster as m is increased; j is constant with a value of 0 (red, filled points) or 15 (blue/cyan, hollow points). The two lines for each curve show inner and outer radii, as described in the text. Lightly colored shaded areas show the geometric profile of the hydrogen atoms within the clusters and follow the curves that are similarly colored. Helium causes an increase in radius of the bubble, while hydrogen alone does not. The addition of helium to the bubble changes the hydrogen's positioning, but allows more hydrogen to remain close to the interior.

hydrogen atom is residing outside the outer radius. This hydrogen atom sits behind an iron atom and pushes it towards the center of the bubble. In contrast (as seen in the blue curves of Figure 35), when 15 helium atoms are also located within the cluster, internal pressure causes an overall increase in radius. The bubble is fairly symmetric with inner and outer radii having nearly the same value, and the radius does not increase further as hydrogen is added. However, the hydrogen profile is affected - hydrogen tends to reside closer to the iron atoms than when helium is absent, but remains largely within the inner radius. More hydrogen remains close to the bubble surface when helium is present than when it is absent. As will be discussed below, this is because the hydrogen has a greater binding energy with helium present than without it, when $j \geq 19$.
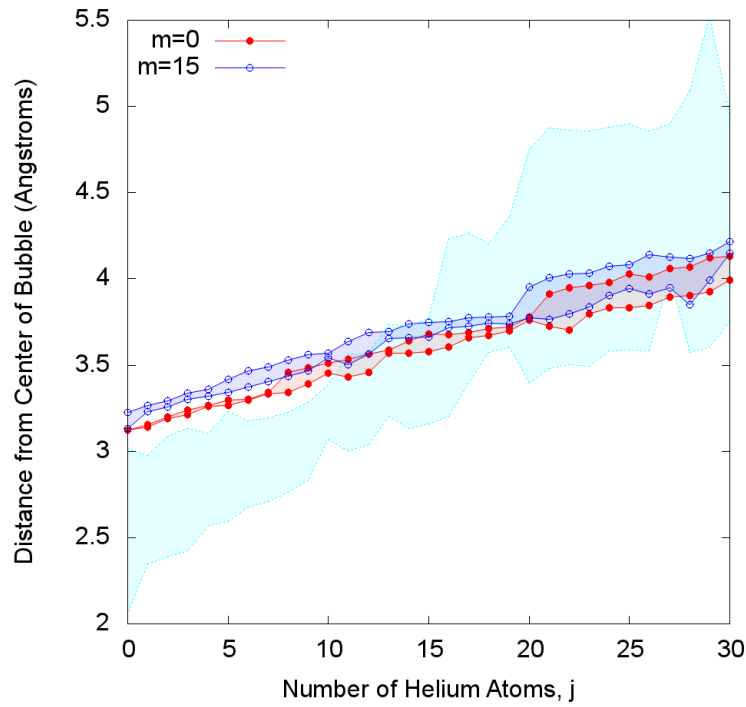
Figure 36: The radii in Angstroms of a $H_mHe_jV_6$ cluster as j is increased; m is constant with a value of 0 (red, filled points) or 15 (blue, hollow points). The two lines for each curve show inner and outer radii, as described in the text. The light cyan area shows the geometric profile of hydrogen atoms within the latter cluster. The radius of the bubble is an increasing function of the helium inventory. As the helium inventory is increased, some of the hydrogen is pushed outside the first neighbor shell of iron.

Figure 36 shows similar profiles, but for bubbles with increasing j and constant m. Unlike for hydrogen, increasing helium results in an increasing radius. Having 15 hydrogen atoms in the bubble seems to further increase the radius, but only very slightly. As helium is increased, the hydrogen in the cluster moves from being primarily inside the inner radius to primarily outside the outer radius. We see that when the cluster gains 21 helium atoms, it becomes slightly less symmetric; additionally, the hydrogen moves a bit farther into the bulk, but it still attracted to the cluster.

4.3.2 Interaction between H and He

The direct interactions between hydrogen and helium can be characterized through their binding energies to $H_m He_j V_6$ clusters, as seen in Figure 37. For these simulations clusters with $0 \leq m \leq 30$ and $0 \leq j \leq 30$ were considered. It should be noted that the Monte Carlo process described in Section 3.2 is essential to obtaining the following results. Since binding energies are on the order of 1 eV, small deviations from the global minima can result in large errors.

The formation energy for a particular cluster can be calculated by taking the difference between a cluster's energy and the sum of the energies of the constituent parts:

$$E_f(H_m He_j V_n) = E_{tot}(H_m He_j V_n) - \left\{ (N-n)E_{coh}^{Fe} + mE_{coh}^{H} + jE_{coh}^{He} \right\}. \tag{24}$$

Here, the "*tot*" subscript refers to total energy, while the "*coh*" subscript refers to cohesive energy. There are N iron atoms in the system lacking defects or impurities. We use the values $E_{coh}^{Fe} = -4.013$ eV/atom, $E_{coh}^{H} = -2.37$ eV/atom, and $E_{coh}^{He} = -.00714$ eV/atom. In general, adding a hydrogen atom to the cluster lowers the total system energy, while adding a helium atom raises it.

The formation energies can be used to calculate the binding of defects and atoms to the clusters. The binding energy of the mth hydrogen atom to a $H_m He_j V_n$ cluster is given by

$$E_B(H) = E_f(H_{m-1} He_j V_n) + E_f^{H} - E_f(H_m He_j V_n), \tag{25}$$

while the binding energy of the jth helium atom is given by

$$E_B(He) = E_f(H_m He_{j-1} V_n) + E_f^{He} - E_f(H_m He_j V_n). \tag{26}$$

The formation energy of a tetrahedral hydrogen interstitial E_f^H is 0.29 eV, while the formation energy of a tetrahedral helium interstitial E_f^{He} is much larger at 4.39 eV.

Helium appears to have a significant effect on the binding of hydrogen to clusters, as can be see in Figure 37(a). For low concentrations of hydrogen (less than about 18 atoms in the void), adding helium to the bubble decreases the hydrogen's binding energy. This is in contrast to the idea that helium directly causes hydrogen to be more tightly bound to bubbles, as has been previously suggested [97]. However, at high concentrations of hydrogen, we see the opposite effect. While hydrogen is essentially unbound from a bubble containing *only* hydrogen, the addition of enough helium allows the hydrogen to remain more strongly bound. This can be attributed to the fact that a large amount of helium atoms will cause an increase in radius of the bubble, resulting in a larger free surface for a given amount of hydrogen to spread out in, as was discussed in the previous section. However, we can generally say that for a bubble with a given radius and a given number of hydrogen atoms, the addition of further gas atoms of either species results in a decreased hydrogen binding to the cluster.

On the other hand, the binding of helium to the clusters is only weakly affected by the presence of hydrogen, as shown in Figure 37(b). For a given amount of helium, introducing hydrogen to the bubble barely affects the helium. Its binding is a much stronger function of the concentration of helium atoms in the bubble - as the concentration increases, helium is less well-bound.

It should be noted that the binding of helium is always much stronger than the binding of hydrogen in these simulations. While the most tightly bound hydrogen atoms are bound by less than 1 eV, the most weakly bound helium atoms are bound by more than 1.5 eV. In summary, the binding energy of hydrogen to the cluster is more strongly affected by helium's presence than vice versa.
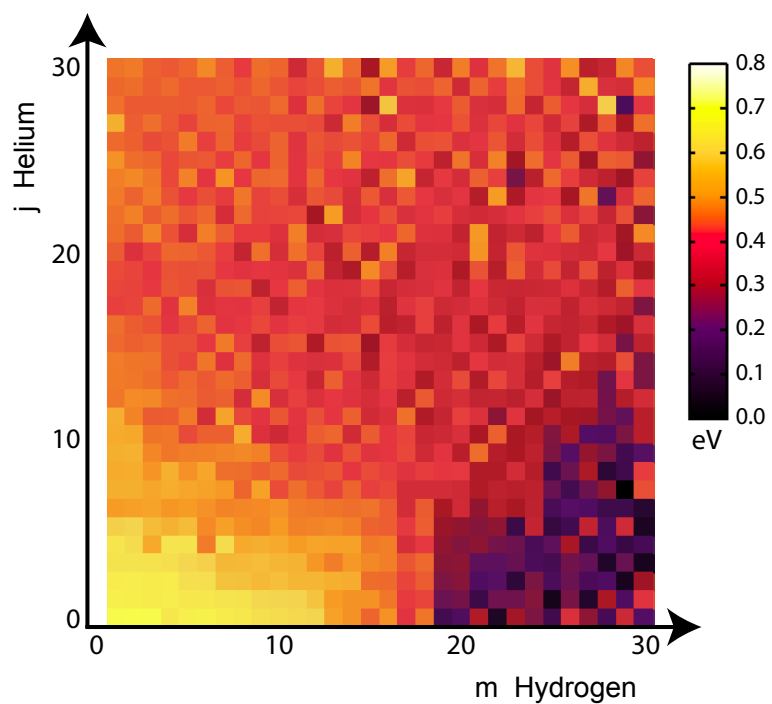
(a) Hydrogen binding energies
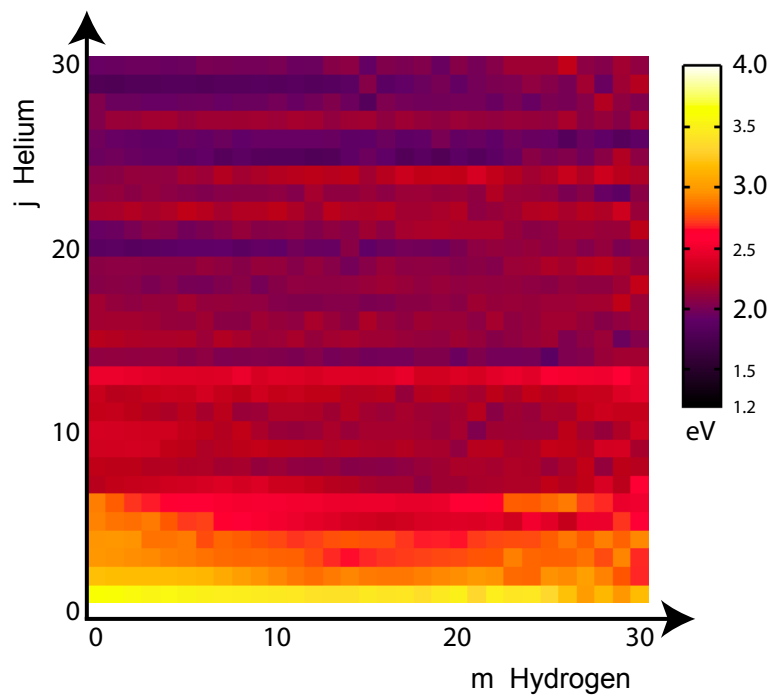
(b) Helium binding energies

Figure 37: The binding energies of hydrogen and helium to $H_mHe_jV_6$ clusters. Binding energies are depicted by the respective color bars; data are in eV.

4.3.3 Binding of Vacancies and Interstitials

We can also characterize the clusters through the binding of point defects. The binding energies of vacancies and self-interstitial iron atoms are given by

$$E_B(\mathrm{V}) = E_f(\mathrm{H}_m\mathrm{He}_j\mathrm{V}_{n-1}) + E_f^V - E_f(\mathrm{H}_m\mathrm{He}_j\mathrm{V}_n). \tag{27}$$

$$E_B(\mathrm{SIA}) = E_f(\mathrm{H}_m\mathrm{He}_j\mathrm{V}_{n+1}) + E_f^{SIA} - E_f(\mathrm{H}_m\mathrm{He}_j\mathrm{V}_n), \tag{28}$$

where $E_f^V = 1.721$ eV and $E_f^{SIA} = 3.529$ eV.

As can been seen in Figure 38, the binding energy of a self-interstitial to a cluster of j helium atoms and 6 vacancies decreases at a faster rate than does the binding of helium itself, as the helium inventory is increased. This trend has previously been observed in several studies [92, 126, 77]. Eventually, at a ratio of about three helium atoms per vacancy, self-interstitials are less well bound than are helium atoms. Once there are several helium atoms in the cluster, vacancies are more tightly bound than either helium or self-interstitials.

Introducing hydrogen to the clusters affects these binding energies. The binding of self-interstitials is consistently lower when 15 hydrogen atoms are included in the clusters than when they are absent, across the entire range of helium inventories. The binding of helium itself is also slightly affected, primarily at low concentrations of helium. Thus the SIA binding energy curve intersects with the helium atom binding energy curve at a lower ratio than when hydrogen is not present, close to $j/n = 2$. Additionally, including hydrogen increases the binding of vacancies to clusters.

4.3.4 Loop Punching

A necessary criterion for loop punching to occur is that the binding of the species inside the bubble to the bubble be stronger than the binding of neighboring matrix atoms to the bubble. For hydrogen in bubbles, binding is rather weak compared to the binding of self-interstitials; hydrogen will always be emitted from the bubble before pressures can build up high enough to generate loop punching. However, for helium, loop punching is a recognized phenomenon; a cluster of helium atoms in the bulk may even punch out an initial vacancy.
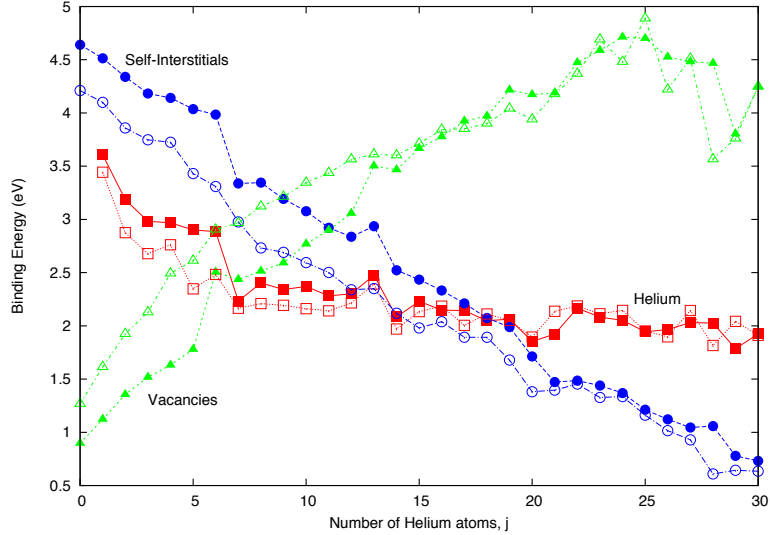
Figure 38: Binding energies (eV) of helium atoms (red squares), SIAs (blue circles), and vacancies (green triangles) to $H_mHe_jV_6$ clusters. Filled data points represent pure helium bubbles ($m = 0$); hollow data points are from bubbles with $m = 15$. As the helium inventory is increased, both the binding of self-interstitials and helium atoms decreases, while the binding of vacancies increases. Hydrogen exacerbates these effects, especially for low helium concentrations.

As shown in Figure 38, in this study of clusters with $n = 6$, this condition occurs for the pure helium bubbles at a ratio of approximately $j/n = 3$.

However, this criterion in and of itself is not sufficient to guarantee loop punching; it must also be energetically favorable for a Frenkel pair to be created. The minimum energy configurations of $H_mHe_jV_n$ and $H_mHe_jV_{n+1}$ bubbles are generated with the method discussed in Section 3.2 . To simulate loop punching, an iron atom is introduced to the latter configuration at a particular lattice site, and the new configuration is minimized. These lattice sites are chosen both near the $(n+1)^{th}$ vacancy and at large distances to determine how an interstitial created at the surface of the bubble would be bound. At each lattice site where a dumbbell was placed, the six possible orientations of a <1 1 0> dumbbell are individually tested; the orientation which results in the lowest energy structure is taken as our data point. The <1 1 0> family of dumbbells is the most stable in bulk bcc iron, but no restriction is made to guarantee that a <1 1 0> configuration is maintained under minimization. However, each minimized state is tested to guarantee that a recombination event has not occurred and the cluster still contains $(n+1)$ vacancies.
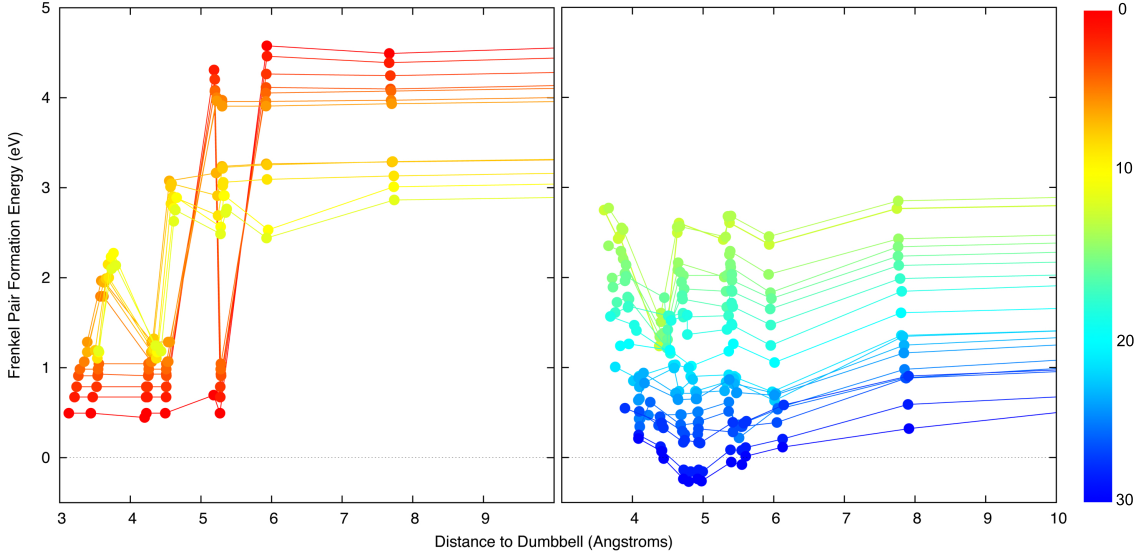
Figure 39: Curves for Frenkel pair formation energy for pure helium bubbles. The x-axis shows the distance of the interstitial from the center of the bubble; y-axis shows the energy of the system containing the Frenkel pair referenced to the system without it. The curves are broken into two plots for ease of understanding. The red curve shows data for $j = 0$; as the curves progress to blue ($j = 30$), the helium concentration increases.

The difference in the energy ΔE of the ($H_m He_j V_{n+1}$+SIA) configuration and the energy of the $H_m He_j V_n$ configuration is due to the change in "defect status" of the atoms in and around the bubble. This include mainly the Frenkel pair formation energy, but also may be affected by the hydrogen atoms on the edge of the cluster:

$$\Delta E = E_{tot}(H_m He_j V_{n+1} + SIA) - E_{tot}(H_m He_j V_n). \tag{29}$$

If the value of ΔE is below zero, it is more energetically favorable for a Frenkel pair to exist than not; therefore, it is more favorable for loop punching to occur. This procedure allows us to examine the energetics of loop punching without the computational expense of performing dynamics and simply waiting to observe the phenomenon.

In Figure 39, several curves for Frenkel pair formation energies in pure helium bubbles ($m = 0$) are shown. The distance shown on the x-axis is the distance from the center of the void to the dumbbell; the vacancy component of the Frenkel pair is stationary. For the $n = 6$ case, loop punching become energetically favorable when $j \geq 29$; that is, when the ratio of helium to vacancies is ~ 4.8. There is a small barrier for this event to occur.

We perform these same calculations on bubbles containing both $m = 15$, with varying amounts of helium, where $n = 6$. Representative curves for $j = 28, 29$ may be seen in Figure 40. As with the pure helium bubbles, as the interstitial dumbbell of the Frenkel pair is moved farther away from the surface of the bubble, the energy of a given system initially drops, but quickly rises again. This indicates that an emitted self-interstitial will be bound to the cluster at a distance of 1-2 Å from the surface. As the interstitial is moved into the bulk, each curve levels off to some asymptotic value.

Thus we can conclude that loop punching becomes energetically favorable in pure helium bubbles when $j = 29$. However, when 15 hydrogen atoms are also included in the cluster, loop punching is favorable with only 27 helium atoms. This is shown in Figure 41, where the minimum value of the ΔE curve is given for each cluster. In almost all cases, when the concentration of helium is high, the presence of 15 hydrogen atoms in the clusters makes loop punching more favorable than it would otherwise be. This may be explained through the binding of hydrogen atoms. When the concentration of helium is high, some hydrogen is forced outside of the inner radius and may be considered to be occupying an interstitial position in the bulk, as shown in Figure 36. For hydrogen, occupying an interstitial position is less energetically favorable than being within a vacancy. Thus, the system is able to lower its energy by creating a Frenkel pair, removing the hydrogen interstitial by reabsorption into the cluster, and increasing the free surface of the bubble.

4.4 Discussion

In our simulations of $H_m He_j V_n$ clusters, we see that the low energy configuration is a core of helium surrounded by a shell of hydrogen. At high concentrations of helium, the presence of hydrogen makes loop punching more energetically favorable than it would otherwise be. The mechanisms behind the synergistic effects of hydrogen and helium are complicated and not obvious, and there are many variables that may affect the outcome of these calculations, not limited to bubble size, interatomic potentials, and temperature effects. However, our work provides a basis for further study.
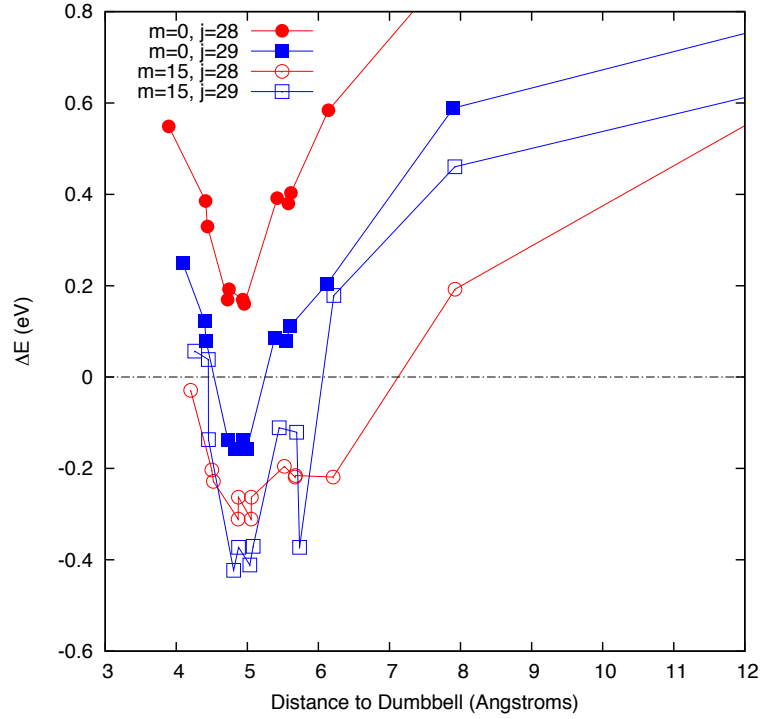
Figure 40: Curves showing the difference in energy between clusters $(H_m He_j V_6)$ with and without a Frenkel pair. The x-axis shows the distance of the interstitial from the center of the bubble; y-axis shows the energy of the system containing the Frenkel pair referenced to the system without it. The red curves with cirucular data points show data for $j = 28$; the blue curves with square points show data for $j = 29$. Filled data points represent pure helium bubbles; empty data points represent bubbles with 15 hydrogen atoms. It is more energetically favorable for a Frenkel pair to exist when the bubbles contain hydrogen. The SIA is bound to the bubble a short distance from the surface.
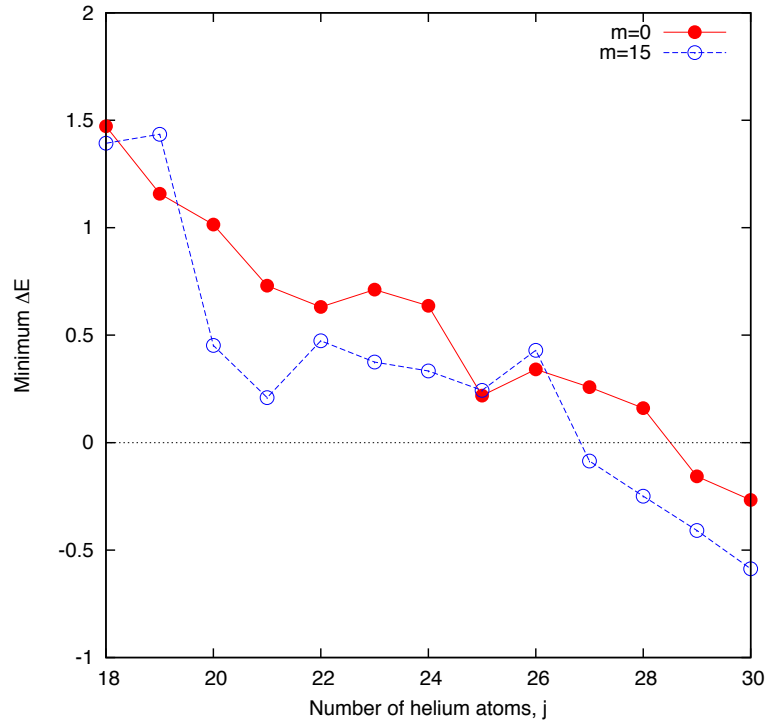
Figure 41: For each $H_mHe_jV_6$ cluster that is tested for energetic the favorability of loop punching, a curve is generated as the interstitial of a Frenkel pair is moved away from the cluster (as shown in Figure 40; this graph shows the minima of those curves. Without hydrogen, loop punching is energetically favorable when $j \geq 29$. Including hydrogen reduces the amount of helium needed to $j = 27$. In almost all cases, loop punching is more energetically favorable when hydrogen is included in a cluster.

It can be argued that the interatomic potentials used in this work do not accurately represent the true interactions, however, we do not feel that any deficiencies in the potentials would substantially change the nature of our conclusions. First, while the H-H interaction potential does provide an attractive well, H_2 molecules are not represented entirely realistically by the EAM formalism. It may be argued that hydrogen could be retained in the center of bubbles lacking helium, contrary to our simulations. While this is entirely plausible for large enough bubbles, we capture the most relevant interactions for the analysis of synergistic and radiation effects. It has been shown with *ab initio* methods [140] that an H_2 molecule placed in a vacancy will dissociate and hybridize with iron; this is seen in the covering of the free surfaces of the bubbles with hydrogen [62]. Indeed, if hydrogen were to be contained in molecular form within the bubbles, the pressures inside the bubbles should only increase, strengthening our conclusions.

Second, the interaction potential between hydrogen and helium may change in the presence of iron. However, there is no obvious physical mechanism that would result in a significantly stronger bonding of hydrogen to helium due to the proximity of iron; hydrogen's predilection to hybridize with iron would still presumably be the dominant interaction. Thus, we believe that the character of our main conclusions would not change even if an interatomic potential incorporating all the nuances of the interactions between iron, hydrogen, and helium were used.

However, the area of interatomic potential creation and validation is a very active one, in particular for the iron-helium system [41, 125]. There are studies which show a dependence on interatomic potentials for clustering behavior [134], so it would be beneficial to explore how our results are affected by the use of different interatomic potentials.

CHAPTER V

CONCLUSIONS

Understanding the interactions between defects in structural materials in a fundamental way is necessary to develop predictive models for irradiated systems. Atomistic simulation is an extremely valuable tool in this pursuit, which allows for the exploration of interactions at a scale and level of detail that is not possible using experiment alone. In this work, we present computational studies of the interactions between point defects and screw line dislocations and the energetics of hydrogen-helium-vacancy clusters in body-centered cubic iron.

In our investigation of dislocation-point defect interactions, we analyze the interaction energy and stability of a variety of interstitial dumbbell configurations and vacancies at a level of detail that has not been investigated before. Comparing our atomistic results to continuum elasticity theory, we provide a guide to where theory is valid and may be safely used in larger scale models, and where more detail that can only be provided by atomistics is required. We observe that a screw dislocation core will spontaneously absorb defects of all types within a few Angstroms, resulting in characteristic core structures.

Next, in our simulations of small gas bubbles in the bulk, we provide a method for searching for minimum energy configurations of hydrogen and helium within vacancy clusters. This method is shown to be of value in our study of multiple hydrogen atoms trapped at monovacancies, in which we find new low energy configurations that have not been studied in the past, and we verify these structures with the help of *ab initio* methods.

We show that hydrogen has a stabilizing effect on vacancy clusters, causing vacancies to be more tightly bound to clusters, while neighboring iron atoms are less tightly bound. These studies of the detailed energetics of clusters are conducted on bubbles that are larger than have been studied in the past, while still retaining the detail of individual interatomic interactions.

Finally, we present the first atomistic computational studies of hydrogen-helium-vacancy

clusters in bcc iron. To accomplish this, we introduce a new interatomic potential for hydrogen and helium. We show that the low energy configuration of a cluster is a core of helium surrounded by a shell of hydrogen. The binding energy of hydrogen, helium, and point defects to the clusters are determined, and we show that the binding of hydrogen is strongly affected by the presence of helium. Finally, we show that the synergistic effects of hydrogen and helium may be explained through the loop punching phenomenon. In this process, the presence of hydrogen makes it more energetically favorable for bubbles to grow through creation of Frenkel pairs at a smaller helium concentration than when hydrogen is absent. The hydrogen atoms are able to be retained more readily by helium bubbles with large free surfaces.

Although we did not perform simulations directly involving both dislocations and hydrogen, further studies linking these phenomena would be beneficial. In the HELP theory of hydrogen embrittlement [10], hydrogen causes dislocations to be mobile, resulting in increased plasticity. We show that the presence of hydrogen does cause self-interstitials to become less well bound to their lattice sites; we also show that the absorption of interstitials leads to rearrangement of the core of a dislocation, resulting in motion of the dislocation. Thus, the methods described in this work could easily be extended to further study these effects.

The interactions of defects within a microstructure are extremely complex and no one atomistic study can fully explain macroscopic behavior. However, our work provides a unique insight into fundamental behavior, as well as providing valuable data that may be used to parameterize further work.

REFERENCES

[1] ABRAMOV, E. and ELIEZER, D., "Trapping of hydrogen in helium-implanted metals," *Journal of Materials Science Letters*, vol. 7, no. 2, pp. 108–110, 1988.

[2] ACKLAND, G., BACON, D., CALDER, A., and HARRY, T., "Computer simulation of point defect properties in dilute Fe-Cu alloy using a many-body interatomic potential," *Philosophical Magazine A*, vol. 75, pp. 713–732, Jan 1997.

[3] ACKLAND, G., MENDELEV, M., SROLOVITZ, D., HAN, S., and BARASHEV, A., "Development of an interatomic potential for phosphorus impurities in alpha-iron," *Journal of Physics: Condensed Matter*, vol. 16, pp. 2629–2642, 2004.

[4] AZEVEDO, C., "A review on neutron-irradiation-induced hardening of metallic components," *Engineering Failure Analysis*, vol. 18, pp. 1921–42, 2011.

[5] BACON, D., OSETSKY, Y., and RONG, Z., "Computer simulation of reactions between an edge dislocation and glissile self-interstitial clusters in iron," *Philosophical Magazine*, vol. 86, pp. 3921–3936, Jan 2006.

[6] BECK, D., "A new interatomic potential function for helium," *Molecular Physics*, vol. 14, no. 4, pp. 311–315, 1968.

[7] BESENBACHER, F., BØTTIGER, J., and MYERS, S., "Deuterium trapping in helium–implanted nickel," *Journal of Applied Physics*, vol. 53, no. 5, pp. 3547–3551, 1982.

[8] BESENBACHER, F., MYERS, S., NORDLANDER, P., and NØRSKOV, J., "Multiple hydrogen occupancy of vacancies in Fe," *Journal of Applied Physics*, vol. 61, p. 1788, 1987.

[9] BHATTACHARYA, A. and ANDERSON, J., "Exact quantum Monte Carlo calculation of the H-He interaction potential," *Physical Review A*, vol. 49, no. 4, pp. 2441–2445, 1994.

[10] BIRNBAUM, H. and SOFRONIS, P., "Hydrogen-enhanced localized plasticity–a mechanism for hydrogen-related fracture," *Materials Science and Engineering: A*, vol. 176, no. 1-2, pp. 191–202, 1994.

[11] BLÖCHL, P., "Projector augmented-wave method," *Physical Review B*, vol. 50, pp. 17953–17979, Jan 1994.

[12] BLOOM, E., ZINKLE, S., and WIFFEN, F., "Materials to deliver the promise of fusion power – progress and challenges," *Journal of Nuclear Materials*, vol. 329, pp. 12–19, 2004.

[13] BULATOV, V. and CAI, W., *Computer simulations of dislocations.* Oxford University Press, 2006.

[14] Burke, K. and Ernzerhof, M., "Generalized gradient approximation made simple," *Physical Review Letters*, vol. 77, pp. 3865–3868, Jan 1996.

[15] Cai, W., Arsenlis, A., Weinberger, C., and Bulatov, V., "A non-singular continuum theory of dislocations," *Journal of the Mechanics and Physics of Solids*, vol. 54, pp. 561–587, Jan 2006.

[16] Capolungo, L., Beyerlein, I. J., and Wang, Z. Q., "The role of elastic anisotropy on plasticity in hcp metals: a three-dimensional dislocation dynamics study," *Modelling and Simulation in Materials Science and Engineering*, vol. 18, no. 085002, 2010.

[17] Caro, A., Hetherly, J., Stukowski, A., Caro, M., Martinez, E., Srivilliputhur, S., Zepeda-Ruiz, L., and Nastasi, M., "Properties of helium bubbles in Fe and FeCr alloys," *Journal of Nuclear Materials*, vol. 418, pp. 261–268, 2011.

[18] Castellote, M., Fullea, J., de Viedma, P., Andrade, C., Alonso, C., Llorente, I., Turrillas, X., Campo, J., Schweitzer, J., and Spillane, T., "Hydrogen embrittlement of high-strength steel submitted to slow strain rate testing studied by nuclear resonance reaction analysis and neutron diffraction," *Nuclear Instruments and Methods in Physics Research Section B: Beam Interactions with Materials and Atoms*, vol. 259, no. 2, pp. 975–983, 2007.

[19] Chang, J., Cai, W., Bulatov, V., and Yip, S., "Molecular dynamics simulations of motion of edge and screw dislocations in a metal," *Computational Materials Science*, vol. 23, pp. 111–115, Jan 2002.

[20] Chaussidon, J., Fivel, M., and Rodney, D., "The glide of screw dislocations in bcc Fe: atomistic static and dynamic simulations," *Acta Materialia*, vol. 54, no. 13, pp. 3407–3416, 2006.

[21] Chen, J., Hoffelner, W., Ullmaier, H., and Jung, P., "Dislocation loops and bubbles in oxide dispersion strengthened ferritic steel after helium implantation under stress," *Acta Materialia*, vol. 56, pp. 250–258, 2008.

[22] Chiesa, S., Gilbert, M., Dudarev, S., Derlet, P., and Swygenhoven, H. V., "The non-degenerate core structure of a 1/2<111> screw dislocation in bcc transition metals modelled using Finnis–Sinclair potentials: The necessary and sufficient conditions," *Philosophical Magazine*, vol. 89, no. 34, pp. 3235–3243, 2009.

[23] Clouet, E., Garruchet, S., Nguyen, H., Perez, M., and Becquart, C., "Dislocation interaction with C in α-Fe: A comparison between atomic simulations and elasticity theory," *Acta Materialia*, vol. 56, no. 14, pp. 3450–3460, 2008.

[24] Condon, J. and Schober, T., "Hydrogen bubbles in metals," *Journal of Nuclear Materials*, vol. 207, pp. 1–24, 1993.

[25] Daw, M. and Baskes, M., "Semiempirical, quantum-mechanical calculation of hydrogren embrittlement in metals," *Physical Review Letters*, vol. 50, pp. 1285–1288, Jan 1983.

[26] Daw, M. and Baskes, M., "Embedded-atom method: Derivation and application to impurities, surfaces, and other defects in metals," *Physical Review B*, vol. 29, pp. 6443–6453, Jan 1984.

[27] DAW, M., FOILES, S., and BASKES, M., "The embedded-atom method - a review of theory and applications," *Materials Science Reports*, vol. 9, pp. 251–310, Jan 1993.

[28] DEDERICHS, P. and SCHROEDER, K., "Anisotropic diffusion in stress fields," *Physical Review B*, vol. 17, no. 6, p. 2524, 1978.

[29] DEO, C., OKUNIEWSKI, M., SRIVILLIPUTHUR, S., MALOY, S., BASKES, M., JAMES, M., and STUBBINS, J., "Helium bubble nucleation in bcc iron studied by kinetic Monte Carlo simulations," *Journal of Nuclear Materials*, vol. 361, no. 2-3, pp. 141–148, 2007.

[30] DOMAIN, C. and MONNET, G., "Simulation of screw dislocation motion in iron by molecular dynamics simulations," *Physical Review Letters*, vol. 95, p. 215506, Nov 2005.

[31] DUDAREV, S. and DERLET, P., "A 'magnetic' interatomic potential for molecular dynamics simulations," *Journal of Physics: Condensed Matter*, vol. 17, pp. 7097–7118, Oct 2005.

[32] DUESBERY, M. and VITEK, V., "Plastic anisotropy in bcc transition metals," *Acta Materialia*, vol. 46, no. 5, pp. 1481–1492, 1998.

[33] DUESBERY, M., VITEK, V., and BOWEN, D., "Effect of shear-stress on screw dislocation core structure in body-centered cubic lattices," *Proceedings of the Royal Society of London A*, vol. 332, pp. 85–111, Jan 1973.

[34] ESHELBY, J., READ, W., and SHOCKLEY, W., "Anisotropic elasticity with applications to dislocation theory," *Acta Metallurgica*, vol. 1, no. 3, pp. 251–259, 1953.

[35] EVANS, J., "The role of implanted gas and lateral stress in blister formation mechanisms," *Journal of Nuclear Materials*, vol. 76 & 77, pp. 228–234, Jan 1978.

[36] FINNIS, M. and SINCLAIR, J., "A simple empirical n-body potential for transition metals," *Philosophical Magazine A*, vol. 50, no. 1, pp. 45–55, 1984.

[37] FREDERIKSEN, S. and JACOBSEN, K., "Density functional theory studies of screw dislocation core structures in bcc metals," *Philosophical Magazine*, vol. 83, pp. 365–375, Jan 2003.

[38] FU, C.-C. and WILLAIME, F., "Ab initio study of helium in alpha-Fe: Dissolution, migration, and clustering with vacancies," *Physical Review B*, vol. 72, no. 6, p. 064117, 2005.

[39] FUJITA, S., OKITA, T., KURAMOTO, E., and SEKIMURA, N., "A study of the interaction between irradiation induced-defect and a line dislocation in bcc-iron," *Journal of Nuclear Materials*, vol. 386-388, pp. 93–96, Feb 2009.

[40] FUKAI, Y., *The Metal-Hydrogen System.* Springer, 2005.

[41] GAO, N., SAMARAS, M., and SWYGENHOVEN, H. V., "A new Fe–He pair potential," *Journal of Nuclear Materials*, vol. 400, pp. 240–244, 2010.

[42] GAO, N., SWYGENHOVEN, H. V., VICTORIA, M., and CHEN, J., "Formation of dislocation loops during He clustering in bcc Fe," *Journal of Physics: Condensed Matter*, vol. 23, p. 442201, 2011.

[43] GAO, N., VICTORIA, M., CHEN, J., and SWYGENHOVEN, H. V., "Helium-vacancy cluster in a single bcc iron crystal lattice," *Journal of Physics: Condensed Matter*, vol. 23, p. 245403, 2011.

[44] GARNER, F. A., OLIVER, B., GREENWOOD, L., JAMES, M., FERGUSON, P., MALOY, S., and SOMMER, W., "Determination of helium and hydrogen yield from measurements on pure metals and alloys irradiated by mixed high energy proton and spallation neutron spectra in lansce," *Journal of Nuclear Materials*, vol. 296, no. 1-3, pp. 66–82, 2001.

[45] GARNER, F. A., SIMONEN, E., OLIVER, B., GREENWOOD, L., GROSSBECK, M., WOLFER, W., and SCOTT, P., "Retention of hydrogen in fcc metals irradiated at temperatures leading to high densities of bubbles or voids," *Journal of Nuclear Materials*, vol. 356, no. 1-3, pp. 122–135, 2006.

[46] GHONIEM, N., TONG, S., HUANG, J., SINGH, B., and WEN, M., "Mechanisms of dislocation-defect interactions in irradiated metals investigated by computer simulations," *Journal of Nuclear Materials*, vol. 307, pp. 843–851, 2002.

[47] GILLAN, M., "The elastic dipole tensor for point defects in ionic crystals," *Journal of Physics C: Solid State Physics*, vol. 17, no. 9, pp. 1473–1488, 1984.

[48] GORDON, P., NEERAJ, T., LI, Y., and LI, J., "Screw dislocation mobility in bcc metals: the role of the compact core on double-kink nucleation," *Modelling and Simulation in Materials Science and Engineering*, vol. 18, p. 085008, 2010.

[49] GREENWOOD, G., FOREMAN, A., and RIMMER, D., "The role of vacancies and dislocations in the nucleation and growth of gas bubbles in irradiated fissile material," *Journal of Nuclear Materials*, vol. 4, pp. 305–324, 1959.

[50] GRÖGER, R., RACHERLA, V., BASSANI, J., and VITEK, V., "Multiscale modeling of plastic deformation of molybdenum and tungsten: II. yield criterion for single crystals based on atomistic studies of glide of 1/2<1 1 1> screw dislocations," *Acta Materialia*, vol. 56, no. 19, pp. 5412–5425, 2008.

[51] GRÖGER, R. and VITEK, V., "Directional versus central-force bonding in studies of the structure and glide of 1/2<1 1 1> screw dislocations in bcc transition metals," *Philosophical Magazine*, vol. 89, no. 34-36, pp. 3163–3178, 2009.

[52] GROH, S. and ZBIB, H., "Advances in discrete dislocations dynamics and multiscale modeling," *Journal of Engineering Materials and Technology*, vol. 131, p. 041209, 2009.

[53] HAGHIGHAT, S., LUCAS, G., and SCHAUBLIN, R., "State of a pressurized helium bubble in iron," *Europhysics Letters*, vol. 85, p. 60008, 2009.

[54] HAYWARD, E. and DEO, C., "Finding minimum energy states of hydrogen-vacancy clusters in iron," *Transactions of the American Nuclear Society*, vol. 104, pp. 63–64, Apr 2011.

[55] HAYWARD, E. and DEO, C., "Energetics of small hydrogen–vacancy clusters in bcc iron," *Journal of Physics: Condensed Matter*, vol. 23, p. 425402, Oct 2011.

[56] HEAD, A., "The [111] dislocation in a cubic crystal," *physica status solidi (b)*, vol. 6, no. 2, pp. 461–465, 1964.

[57] HEINISCH, H., GAO, F., and KURTZ, R., "Atomic-scale modeling of interactions of helium, vacancies and helium–vacancy clusters with screw dislocations in alpha-iron," *Philosophical Magazine*, vol. 90, no. 7, pp. 885–895, 2010.

[58] HIRTH, J., "Effects of hydrogen on the properties of iron and steel," *Metallurgical and Materials Transactions A*, vol. 11, no. 6, pp. 861–890, 1980.

[59] HIRTH, J. and GEHLEN, P., "Dislocation displacement fields in anisotropic media," *Journal of Applied Physics*, vol. 40, no. 5, pp. 2177–2181, 1969.

[60] HIRTH, J. and LOTHE, J., *Theory of Dislocations*. McGraw-Hill, Inc., 1982.

[61] HOHENBERG, P. and KOHN, W., "Inhomogeneous electron gas," *Physical Review*, vol. 136, pp. B864–B871, Jan 1964.

[62] IRIGOYEN, B., FERULLO, R., CASTELLANI, N., and JUAN, A., "The interaction of hydrogen with an Fe vacancy: a molecular orbital simulation," *Journal of Physics D: Applied Physics*, vol. 29, pp. 1306–1309, 1996.

[63] IWAMOTO, M. and FUKAI, Y., "Superabundant vacancy formation in iron under high hydrogen pressures: Thermal desorption spectroscopy," *Materials Transactions-JIM*, vol. 40, no. 7, pp. 606–611, 1999.

[64] IYER, R. and PICKERING, H., "Mechanism and kinetics of electrochemical hydrogen entry and degradation of metallic systems," *Annual Review of Materials Science*, vol. 20, no. 1, pp. 299–338, 1990.

[65] JEPSEN, O. and ANDERSEN, O., "Improved tetrahedron method for brillouin-zone integrations," *Physical Review B*, vol. 49, pp. 16223–16233, Jan 1994.

[66] JIANG, D. and CARTER, E. A., "Diffusion of interstitial hydrogen into and through bcc Fe from first principles," *Physical Review B*, vol. 70, no. 6, p. 64102, 2004.

[67] JOUBERT, D., "From ultrasoft pseudopotentials to the projector augmented-wave method," *Physical Review B*, vol. 59, pp. 1758–1775, Jan 1999.

[68] JUAN, A., IRIGOYEN, B., and GESARI, S., "Electronic structure and bonding of hydrogen in a screw dislocated bcc Fe," *Applied Surface Science*, vol. 172, pp. 8–17, Jan 2001.

[69] JUSLIN, N. and NORDLUND, K., "Pair potential for Fe-He," *Journal of Nuclear Materials*, vol. 382, no. 2-3, pp. 143–146, 2008.

[70] KOHN, W. and SHAM, L., "Self-consistent equations including exchange and correlation effects," *Physical Review*, vol. 140, pp. A1133–A1138, Jan 1965.

[71] KRESSE, G., "Efficient iterative schemes for *ab initio* total-energy calculations using a plane-wave basis set," *Physical Review B*, vol. 54, pp. 11169–11186, Jan 1996.

[72] Krom, A. and Bakker, A., "Hydrogen trapping models in steel," *Metallurgical and Materials Transactions B*, vol. 31, no. 6, pp. 1475–1482, 2000.

[73] Kurtz, R., Heinisch, H., and Gao, F., "Modeling of He-defect interactions in ferritic alloys for fusion," *Journal of Nuclear Materials*, vol. 382, no. 2-3, pp. 134–142, 2008.

[74] Lennard-Jones, J., "Cohesion," *Proceedings of the Physical Society*, vol. 43, p. 461, 1931.

[75] Liu, X. and Biner, S., "Molecular dynamics simulations of the interactions between screw dislocations and self-interstitial clusters in body-centered cubic Fe," *Scripta Materialia*, vol. 59, no. 1, pp. 51–54, 2008.

[76] Liu, Z. L., Liu, X. M., Zhuang, Z., and You, X. C., "A multi-scale computational model of crystal plasticity at submicron-to-nanometer scales," *International Journal of Plasticity*, vol. 25, pp. 1436–1455, Aug 2009.

[77] Lucas, G. and Schäublin, R., "Stability of helium bubbles in alpha-iron: A molecular dynamics study," *Journal of Nuclear Materials*, vol. 386, pp. 360–362, 2009.

[78] Masuda, K., Sugano, K., and Sato, A., "Interaction energy between a self-interstitial and a (1/2)<111> screw dislocation in b. c. c. transition metals," *Journal of the Physical Society of Japan*, vol. 48, no. 4, pp. 1233–1236, 1980.

[79] Masuda-Jindo, K., "On the interaction between a screw dislocation and point defects in bcc transition metals," *physica status solidi (b)*, vol. 129, no. 2, pp. 595–599, 1985.

[80] McDowell, D., "Viscoplasticity of heterogeneous metallic materials," *Materials Science and Engineering: R: Reports*, vol. 62, no. 3, pp. 67–123, 2008.

[81] McLellan, R. and Harkins, C., "Hydrogen interactions with metals," *Mater Sci Eng*, vol. 18, pp. 5–35, 1975.

[82] Meissner, N., Savino, E., Willis, J., and Bullough, R., "The dislocation loop in an anisotropic medium and its interaction with an interstitial atom," *physica status solidi (b)*, vol. 63, no. 1, 1974.

[83] Mendelev, M., Han, S., Srolovitz, D., Ackland, G., Sun, D., and Asta, M., "Development of new interatomic potentials appropriate for crystalline and liquid iron," *Philosophical Magazine*, vol. 83, no. 35, pp. 3977–3994, 2003.

[84] Methfessel, M., "High-precision sampling for brillouin-zone integration in metals," *Physical Review B*, vol. 40, pp. 3616–3621, Jan 1989.

[85] Metropolis, N., Rosenbluth, A., Rosenbluth, M., Teller, A., and Teller, E., "Equation of state calculations by fast computing machines," *The Journal of Chemical Physics*, vol. 21, no. 6, p. 1087, 1953.

[86] Miller, W., *Treatise on Crystallography*. Cambridge, 1839.

[87] Monasterio, P., Lau, T., Yip, S., and Vliet, K. V., "Hydrogen-vacancy interactions in Fe-C alloys," *Physical Review Letters*, vol. 103, no. 8, p. 85501, 2009.

[88] MONTI, A., SARCE, A., SMETNIANSKY-DEGRANDE, N., SAVINO, E., and TOMÉ, C., "Point defects and sink strength in h.c.p. metals," *Philosophical Magazine A*, vol. 63, pp. 925–936, Jan 1991.

[89] MORIARTY, J., VITEK, V., BULATOV, V., and YIP, S., "Atomistic simulations of dislocations and defects," *Journal of Computer-Aided Materials Design*, vol. 9, pp. 99–132, Jan 2002.

[90] MORISHITA, K., "Nucleation path of helium bubbles in metals during irradiation," *Philosophical Magazine*, vol. 87, no. 7, pp. 1139–1158, 2007.

[91] MORISHITA, K., SUGANO, R., and WIRTH, B. D., "MD and KMC modeling of the growth and shrinkage mechanisms of helium-vacancy clusters in Fe," *Journal of Nuclear Materials*, vol. 323, no. 2-3, pp. 243–250, 2003.

[92] MORISHITA, K., SUGANO, R., WIRTH, B. D., and DE LA RUBIA, T. D., "Thermal stability of helium–vacancy clusters in iron," *Nuclear Instruments and Methods in Physics Research, B*, vol. 202, pp. 76–81, 2003.

[93] MROVEC, M., NGUYEN-MANH, D., ELSÄSSER, C., and GUMBSCH, P., "Magnetic bond-order potential for iron," *Physical Review Letters*, vol. 106, no. 24, p. 246402, 2011.

[94] MUGHRABI, H., "On the current understanding of strain gradient plasticity," *Materials Science and Engineering: A*, vol. 387, pp. 209–213, 2004.

[95] MULLER, M., ERHART, P., and ALBE, K., "Analytic bond-order potential for bcc and fcc iron-comparison with established embedded-atom method potentials," *Journal of Physics: Condensed Matter*, vol. 19, no. 32, p. 326220, 2007.

[96] MYERS, S., BASKES, M., BIRNBAUM, H., CORBETT, J., DELEO, G., ESTREICHER, S., HALLER, E., JENA, P., JOHNSON, N., and KIRCHHEIM, R., "Hydrogen interactions with defects in crystalline solids," *Reviews of Modern Physics*, vol. 64, no. 2, pp. 559–617, 1992.

[97] MYERS, S., FOLLSTAEDT, D., BESENBACHER, F., and BØTTIGER, J., "Trapping and surface permeation of deuterium in He–implanted Fe," *Journal of Applied Physics*, vol. 53, no. 12, pp. 8734–8744, 1982.

[98] MYERS, S., PICRAUX, S., and STOLTZ, R., "Defect trapping of ion–implanted deuterium in Fe," *Journal of Applied Physics*, vol. 50, p. 5710, 1979.

[99] MYERS, S., RICHARDS, P., WAMPLER, W., and BESENBACHER, F., "Ion-beam studies of hydrogen-metal interactions," *Journal of Nuclear Materials*, vol. 165, no. 1, pp. 9–64, 1989.

[100] NABARRO, F., "Theory of crystal dislocations," *Oxford University Press*, 1967.

[101] NAGUMO, M., "Function of hydrogen in embrittlement of high-strength steels," *ISIJ International*, vol. 41, pp. 590–598, Jan 2001.

[102] NAGUMO, M., NAKAMURA, M., and TAKAI, K., "Hydrogen thermal desorption relevant to delayed-fracture susceptibility of high-strength steels," *Metallurgical and Materials Transactions A*, vol. 32, no. 2, pp. 339–347, 2001.

[103] Nordlander, P., Nørskov, J., Besenbacher, F., and Myers, S., "Multiple deuterium occupancy of vacancies in Pd and related metals," *Physical Review B*, vol. 40, no. 3, pp. 1990–1992, 1989.

[104] Nørskov, J., "Covalent effects in the effective-medium theory of chemical binding: Hydrogen heats of solution in the 3d metals," *Physical Review B*, vol. 26, no. 6, pp. 2875–2885, 1982.

[105] Nørskov, J. and Besenbacher, F., "Theory of hydrogen interaction with metals," *Journal of the Less Common Metals*, vol. 130, pp. 475–490, 1987.

[106] Oriani, R., "The diffusion and trapping of hydrogen in steel," *Acta Metallurgica*, vol. 18, no. 1, pp. 147–157, 1970.

[107] Oriani, R., "Hydrogen embrittlement of steels," *Annual Review of Materials Science*, vol. 8, no. 1, pp. 327–357, 1978.

[108] Oriani, R. and Josephic, P., "Equilibrium aspects of hydrogen-induced cracking of steels," *Acta Metallurgica*, vol. 22, no. 9, pp. 1065–1074, 1974.

[109] Oriani, R. and Josephic, P., "Equilibrium and kinetic studies of the hydrogen-assisted cracking of steel," *Acta Metallurgica*, vol. 25, no. 9, pp. 979–988, 1977.

[110] Osetsky, Y., Bacon, D., Serra, A., Singh, B., and Golubov, S., "Stability and mobility of defect clusters and dislocation loops in metals," *Journal of Nuclear Materials*, vol. 276, no. 1, pp. 65–77, 2000.

[111] Osetsky, Y., Serra, A., and Priego, V., "Interactions between mobile dislocation loops in Cu and α-fe," *Journal of Nuclear Materials*, vol. 276, no. 1, pp. 202–212, 2000.

[112] Patra, A. and McDowell, D., "Crystal plasticity-based constitutive modelling of irradiated bcc structures," *Philosophical Magazine*, pp. 1–27, Jan 2011.

[113] Plimpton, S., "Fast parallel algorithms for short-range molecular dynamics," *Journal of Computational Physics*, vol. 117, no. 1, pp. 1–19, 1995.

[114] Pronsato, M., Brizuela, G., and Juan, A., "The electronic structure and location of H pairs in bcc Fe edge dislocation," *Applied Surface Science*, vol. 173, pp. 368–379, Jan 2001.

[115] Pronsato, M., Pistonesi, C., and Juan, A., "Density functional study of H–Fe vacancy interaction in bcc iron," *Journal of Physics: Condensed Matter*, vol. 16, p. 6907, 2004.

[116] Puska, M. and Nieminen, R., "Theory of hydrogen and helium impurities in metals," *Physical Review B*, vol. 29, no. 10, pp. 5382–5397, 1984.

[117] Qin, Q. and Bassani, J., "Non-associated plastic flow in single crystals," *Journal of the Mechanics and Physics of Solids*, vol. 40, no. 4, pp. 835–862, 1992.

[118] Racherla, V. and Bassani, J., "Strain burst phenomena in the necking of a sheet that deforms by non-associated plastic flow," *Modelling and Simulation in Materials Science and Engineering*, vol. 15, p. S297, 2007.

[119] RAMASUBRAMANIAM, A., ITAKURA, M., and CARTER, E. A., "Interatomic potentials for hydrogen in alpha–iron based on density functional theory," *Physical Review B*, vol. 79, no. 17, p. 174101, 2009.

[120] RAMASUBRAMANIAM, A., ITAKURA, M., ORTIZ, M., and CARTER, E. A., "Effect of atomic scale plasticity on hydrogen diffusion in iron: Quantum mechanically informed and on-the-fly kinetic monte carlo simulations," *Journal of Materials Research*, vol. 23, pp. 2757–2773, Jan 2008.

[121] RAMASUBRAMANIAM, A., ITAKURA, M., and CARTER, E. A., "Erratum: Interatomic potentials for hydrogen in alpha–iron based on density functional theory [Phys. Rev. B 79, 174101 (2009)]," *Physical Review B*, vol. 81, p. 099902, Mar 2010.

[122] RHEE, M., STOLKEN, J., BULATOV, V., DE LA RUBIA, T., ZBIB, H., and HIRTH, J., "Dislocation stress fields for dynamic codes using anisotropic elasticity: methodology and analysis," *Materials Science and Engineering: A*, vol. 309, pp. 288–293, 2001.

[123] SCHAUBLIN, R. and BALUC, N., "Radiation damage in ferritic/martensitic steels for fusion reactors: a simulation," *Nuclear Fusion*, vol. 47, pp. 1690–1695, 2007.

[124] SEKIMURA, N., IWAI, T., ARAI, Y., YONAMINE, S., NAITO, A., MIWA, Y., and HAMADA, S., "Synergistic effects of hydrogen and helium on microstructural evolution in vanadium alloys by triple ion beam irradiation," *Journal of Nuclear Materials*, vol. 283, pp. 224–228, 2000.

[125] SELETSKAIA, T., OSETSKY, Y., STOLLER, R., and STOCKS, G., "Development of a Fe-He interatomic potential based on electronic structure calculations," *Journal of Nuclear Materials*, vol. 367, pp. 355–360, 2007.

[126] SELETSKAIA, T., OSETSKY, Y., STOLLER, R., and STOCKS, G., "Calculation of helium defect clustering properties in iron using a multi-scale approach," *Journal of Nuclear Materials*, vol. 351, no. 1-3, pp. 109–118, 2006.

[127] SHASTRY, V. and DE LA RUBIA, T. D., "The interaction between point defects and edge dislocation in bcc iron," *Journal of Engineering Materials and Technology*, vol. 121, p. 126, 1999.

[128] SIVAK, A., CHERNOV, V., DUBASOVA, N., and ROMANOV, V., "Anisotropy migration of self-point defects in dislocation stress fields in bcc Fe and fcc Cu," *Journal of Nuclear Materials*, vol. 367, pp. 316–321, Jan 2007.

[129] SIVAK, A., ROMANOV, V., and CHERNOV, V., "Diffusion of self-point defects in body-centered cubic iron crystal containing dislocations," *Crystallography Reports*, vol. 55, pp. 97–108, Jan 2010.

[130] SMETNIANSKY-DEGRANDE, N., SAVINO, E., and C.N.TOME, "Stress induced anisotropic diffusion of intrinsic point defects towards dislocations in h.c.p. crystals," *physica status solidi (b)*, vol. 144, p. 271, 1987.

[131] SONG, J. and CURTIN, W. A., "A nanoscale mechanism of hydrogen embrittlement in metals," *Acta Materialia*, vol. 59, pp. 1557–1569, Feb 2011.

[132] Sørensen, M. and Voter, A., "Temperature-accelerated dynamics for simulation of infrequent events," *The Journal of Chemical Physics*, vol. 112, p. 9599, 2000.

[133] Stewart, D. and Osetsky, Y., "Atomistic studies of formation and diffusion of helium clusters and bubbles in bcc iron," *Journal of Nuclear Materials*, Jan 2010.

[134] Stewart, D., Osetsky, Y., Stoller, R., Golubov, S., Seletskaia, T., and Kamenski, P., "Atomistic studies of helium defect properties in bcc iron: comparison of He–Fe potentials," *Philosophical Magazine*, vol. 90, no. 7-8, pp. 935–944, 2010.

[135] Stoller, R., Golubov, S., Kamenski, P., Seletskaia, T., and Osetsky, Y., "Implementation of a Fe-He 3-body interatomic potential," *Oak Ridge National Lab Report (unpublished)*.

[136] Stroh, A. N., "Dislocations and cracks in anisotropic elasticity," *Philosophical Magazine*, vol. 3, no. 625, 1958.

[137] Taketomi, S., Matsumoto, R., and Miyazaki, N., "Atomistic study of hydrogen distribution and diffusion around a {1 1 2}< 1 1 1> edge dislocation in alpha iron," *Acta Materialia*, vol. 56, no. 15, pp. 3761–3769, 2008.

[138] Tanaka, T., Oka, K., Ohnuki, S., Yamashita, S., Suda, T., Watanabe, S., and Wakai, E., "Synergistic effect of helium and hydrogen for defect evolution under multi-ion irradiation of Fe-Cr ferritic alloys," *Journal of Nuclear Materials*, vol. 329, pp. 294–298, 2004.

[139] Tanguy, D. and Mareschal, M., "Superabundant vacancies in a metal-hydrogen system: Monte carlo simulations," *Physical Review B*, vol. 72, no. 17, p. 174116, 2005.

[140] Tateyama, Y. and Ohno, T., "Atomic-scale effects of hydrogen in iron toward hydrogen embrittlement: Ab-initio study," *ISIJ international*, vol. 43, no. 4, pp. 573–578, 2003.

[141] Tateyama, Y. and Ohno, T., "Stability and clusterization of hydrogen-vacancy complexes in alpha-fe: An ab initio study," *Physical Review B*, vol. 67, p. 174105, May 2003.

[142] Tolstolutskaya, G., Ruzhytskiy, V., Kopanets, I., Karpov, S., Bryk, V., Voyevodin, V., and Garner, F. A., "Displacement and helium-induced enhancement of hydrogen and deuterium retention in ion-irradiated 18Cr10NiTi stainless steel," *Journal of Nuclear Materials*, vol. 356, no. 1-3, pp. 136–147, 2006.

[143] Tomé, C., Cecatto, H., and Savino, E., "Point-defect diffusion in a strained crystal," *Physical Review B*, vol. 25, no. 12, pp. 7428–7440, 1982.

[144] Tomé, C. and Savino, E., "Interaction between point defects and straight dislocations in hexagonal crystals," *Materials Science and Engineering*, vol. 24, pp. 109–122, Jan 1976.

[145] Trinkaus, H. and Singh, B., "Helium accumulation in metals during irradiation–where do we stand?," *Journal of Nuclear Materials*, vol. 323, pp. 229–242, 2003.

[146] TRINKAUS, H. and WOLFER, W., "Conditions for dislocation loop punching by helium bubbles," *Journal of Nuclear Materials*, vol. 122 & 123, pp. 552–557, Jan 1984.

[147] TROIANO, A. R., "The role of hydrogen and other interstitials in the mechanical behavior of metals," *Trans. ASM*, vol. 52, p. 54, 1960.

[148] VENTELON, L. and WILLAIME, F., "Core structure and Peierls potential of screw dislocations in α-Fe from first principles: cluster versus dipole approaches," *Journal of Computer-Aided Materials Design*, vol. 14, pp. 85–94, 2007.

[149] VENTELON, L. and WILLAIME, F., "Generalized stacking-faults and screw-dislocation core-structure in bcc iron: A comparison between ab initio calculations and empirical potentials," *Philosophical Magazine*, vol. 90, pp. 1063–1074, Mar 2010.

[150] VITEK, V., "Computer simulation of the screw dislocation motion in b.c.c. metals under the effect of the external shear and uniaxial stresses," *Proceedings of the Royal Society of London A*, vol. 352, pp. 109–124, Jan 1976.

[151] VITEK, V., "Structure of dislocation cores in metallic materials and its impact on their plastic behavior," *Progress in Materials Science*, vol. 36, pp. 1–27, Jan 1992.

[152] WAKAI, E., SAWAI, T., FURUYA, K., NAITO, A., ARUGA, T., KIKUCHI, K., YAMASHITA, S., OHNUKI, S., YAMAMOTO, S., and NARAMOTO, H., "Effect of triple ion beams in ferritic/martensitic steel on swelling behavior," *Journal of Nuclear Materials*, vol. 307, pp. 278–282, 2002.

[153] WALLIN, M., CURTIN, W. A., RISTINMAA, M., and NEEDLEMAN, A., "Multi-scale plasticity modeling: Coupled discrete dislocation and continuum crystal plasticity," *Journal of the Mechanics and Physics of Solids*, vol. 56, no. 11, pp. 3167–3180, 2008.

[154] WEN, M., TAKAHASHI, A., and GHONIEM, N. M., "Kinetics of self-interstitial cluster aggregation near dislocations and their influence on hardening," *Journal of Nuclear Materials*, vol. 392, pp. 386–395, Aug 2009.

[155] WILSON, W. *in: Conference on Fundamental Aspects of Radiation Damage in Metals*, vol. USERDA-CONF-751006-P2, p. 1025, 1975.

[156] WILSON, W., BISSON, C., and BASKES, M., "Self-trapping of helium in metals," *Physical Review B*, vol. 24, no. 10, pp. 5616–5624, 1981.

[157] WOODWARD, C. and RAO, S., "Ab-initio simulation of isolated screw dislocations in bcc Mo and Ta," *Philosophical Magazine A*, vol. 81, no. 5, pp. 1305–1316, 2001.

[158] ZBIB, H. and AIFANTIS, E., "Size effects and length scales in gradient plasticity and dislocation dynamics," *Scripta Materialia*, vol. 48, no. 2, pp. 155–160, 2003.